CHALCOGENIDE-ON-LITHIUM NIOBATE RESONATOR WAVEGUIDES AND THEIR NONLINEAR APPLICATIONS

A Dissertation

by

YIFENG ZHOU

Submitted to the Office of Graduate and Professional Studies of
Texas A&M University
in partial fulfillment of the requirements for the degree of

DOCTOR OF PHILOSOPHY

Chair of Committee,	Christi K. Madsen
Committee Members,	Ohannes Eknoyan
	Jim Ji
	Alexey Belyanin
Head of Department,	Chanan Singh

December 2014

Major Subject: Electrical Engineering

ABSTRACT

Chalcegenide glass material, such as amorphous As_2S_3, is an ideal candidate material to be integrated onto a much lower refractive index substrate and used as an all-optical active device. The As_2S_3 glass is with wide infrared transparence from near IR to mid IR and refractive index as high as 2.45 at 1.55 μm. As_2S_3 glass also shows a good potential as a Kerr medium for ultra-fast all-optical tuning capability because of its high nonlinearity coefficient at infrared wavelength range.

In terms of the all-optical nonlinear application, resonant cavity devices are favored for their easily tunable ability as a small change of refractive index in the material would lead to a shift for their resonance. Therefore, it is motivating to combine the As_2S_3-on-$LiNbO_3$ optical waveguide platform and the resonant cavity structure together for the integrated all-optical circuits.

A vertically integrated As_2S_3 ring resonator side-coupled to a low-index Ti:diffused $LiNbO_3$ straight waveguide was designed and fabricated. At 1.55-μm wavelength, a low 1.2 dB/cm propagation loss and an over 30-dB extinction ratio were demonstrated on the fabricated As_2S_3-on-$LiNbO_3$ ring resonator waveguide with 400-μm bend radius, which corresponded to an intrinsic Q value as high as $3.5x10^5$. At the same time, an integrated As_2S_3-on-$LiNbO_3$ optical cavity waveguide based on sidewall grating couplers was designed, fabricated and optically tested. Using the sidewall grating couplers with a coupling strength as high as 14 mm^{-1}, the cavity resonant response with a

FSR of 0.5 nm over a 5 nm bandwidth at 1.55 μm was demonstrated with a cavity propagation loss at 2.5 dB/cm.

The waveguide nonlinear efficiency γ of the As_2S_3-on-$LiNbO_3$ ring waveguide was calculated at 3.85 radian/m·W and a pump-signal measurement platform was setup to observe the nonlinear tuning phenomenon of the ring resonator waveguide. Also, the nonlinear tunability of our hybrid As_2S_3-on-$LiNbO_3$ grating cavity waveguide is numerically analyzed. The optical energy at the resonant wavelength inside the grating cavity waveguide is 7 times as high as the input energy, which would significantly reduce the pump power for the nonlinear tuning applications.

DEDICATION

To my family

ACKNOWLEDGEMENTS

I would like to thank my committee chair and advisor, Dr. Christi K. Madsen. Her guidance and support on my research work through the past five years help me finish this dissertation. I am especially thankful for her patience and encouragement when I faced trouble and difficulties in the research works. I am also grateful to my committee members, Dr. Ohannes Eknoyan, Dr. Jim Ji and Dr. Alexey Belyanin, for their guidance, time and support efforts through this course of the research thesis.

I would also like to express my gratitude to the ISSE staff, Larry Rehn, Robert Atkins, Jim Gardner and Dennie R. Spears for their supports in my research works. I appreciate a lot from the discussion and help from my friends and group members. They are Qi Chen, Xin Xia, Mehmet Solmaz, William Snider, Xin Wang, Jae Hyun Kim, Ran Huang, Yuxiao Liu, Dwayne Macik and Chen Zhang.

Finally, I would like to thank my mother, Yun Le and my aunt, Qun Le for their love and encouragement for the past five years.

TABLE OF CONTENTS

CHAPTER

LIST OF FIGURES

FIGURE Page

FIGURE Page

FIGURE Page

FIGURE Page

FIGURE Page

LIST OF TABLES

TABLE Page

CHAPTER I

INTRODUCTION

1.1 Background and motivation

Near infrared (IR) light refers to the electromagnetic radiation at the wavelength range from 769 nm to 2.5 μm. Fiber optical telecommunication chooses the wavelength at 1.55 μm inside the near IR range because at this wavelength, the attenuation of silicon dioxide (SiO_2), the material which the current commercial optical fibers are made from, shows the smallest loss. A single mode optical fiber working at 1.55 μm available at the market now has an up-to-date propagation loss as low as 0.17 dB/km [1]. Now the optical fibers are widely used as the medium for the telecommunication and computer networking. Thanks to their extremely low propagation loss and flexibility for bundled cables, the optical fibers are especially advantageous for the long distance communication. The recorded highest data transmission speed of optical fibers is 400 Gbit/s.

However, compared to the high speed of the data transmission, the whole computer networking data processing speed is only about several gigabits per second. The core process units of the computer networking are based on the silicon semiconductor electrical circuits and the slow electron response speed of the semiconductor material limits the upper bound processing speed of the whole networking system. And electro-optical conversion devices are employed connecting the

optical data and electrical processing units: the LED detectors convert the optical signals to the electrical signals and lasers convert the electrical signals to the optical signals. An all-optical network is a system that completely working in the optical domain and consists of two parts: the all-optical computing part and the optical fiber part. They are connected by the optical switches. To realize the all-optical computing functions, the optical circuits should have several key components including the modulators, the reconfigurable filters and lasers. All of these components are driven by the optical signals without any electrical signals involved and are desired to be integrated on a single chip.

Optical waveguides are the ideal platform to realize the active optical circuit components and can be integrated onto the single chip. The optical modulator, reconfigurable filter, frequency converter and laser are realized with optical waveguides on various material platforms, such as Si-on-insulator (SOI) [2], III-IV material-on-insulator [3], chalcogenide-on-insulator [4], Si_3N_4-on-SiO_2 [5] and as well as chalcogenide-on-$LiNbO_3$ [6]. The all-optical active waveguides should meet at least two requirements: a big refractive index contrast between the waveguide and substrate materials to confine the optical mode in the core with respected to the cladding; a large nonlinear coefficient of the waveguide material for the all-optical signal processing purposes.

A large refractive index contrast between the waveguide layer and the substrate would ensure the optical mode well confined inside a small area which would allow a small bend radii optical mode propagation loss and minimize the waveguide device

footprint for the integration. All-optical reconfigurable waveguides mean the waveguide device parameters (i.e. optical mode index) can be varied with an optical power injection into the waveguide material. An example of an all-optical active device is a ring-structure logic gate (Fig. 1.1). The passive optical spectral response of a ring resonator is the blue color curve and at its resonant wavelength λ_1, the light is trapped inside the resonator without any optical power at the output which stands for the '0' bit. If the ring waveguide refractive index is tuned by an incident optical pump power and the resonant wavelength is shifted to λ_2 shown in the red curve, the output power at wavelength λ_1 stands for the '1' bit.

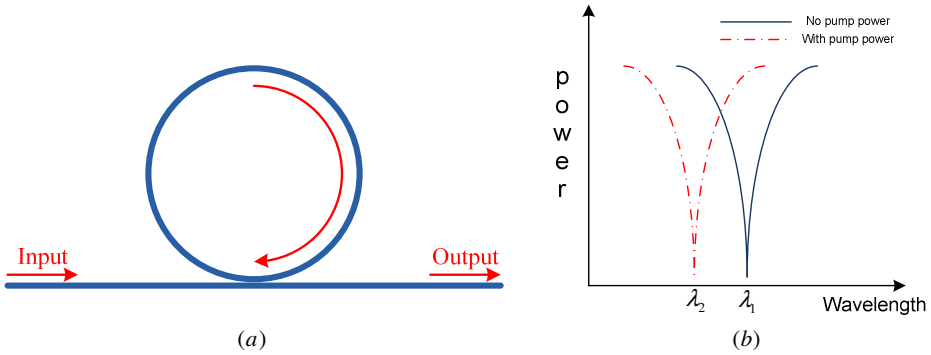

Fig. 1.1 (a) A schematic figure of an optical ring resonator waveguide (b) The ring resonator spectral response with and without an incident optical pump power

1.2 Integrated chalcogenide-on-$LiNbO_3$ optical waveguide

Chalcegenide glass material, such as amorphous As_2S_3, is an ideal candidate material to be integrated onto a much lower refractive index substrate and used as an all-optical active device. The As_2S_3 glass is with wide infrared transparence and refractive

index as high as 2.45 at 1.55 μm, which can be utilized to make low loss tight bend radii optical waveguide devices at the operation wavelength range from near IR to mid IR. The comparison of index contrast and waveguide dimension between As_2S_3 and other materials can be found in Table 1.1. As_2S_3 glass also shows a good potential as a Kerr medium for ultra-fast all-optical tuning capability because of its high nonlinearity coefficient at infrared wavelength range. The nonlinearity comparison between As_2S_3 and other materials is shown in Table 1.2.

Material	Silicon-on-Insulator (SOI)	ChG glass	Ti:$LiNbO_3$	III-V materials
Index contrast	~60%	~20%	<0.03%	~70%
Dimension size	<1 μm	~3 μm	~7-12 μm	~2-3 μm

Table 1.1 Comparison of index contrast and waveguide dimension between As_2S_3 and other materials

On the other side, $LiNbO_3$ is a very good substrate for As_2S_3 waveguide. The benefits by using the $LiNbO_3$ as the substrate mainly show in three aspects. Firstly, its much lower refractive index compared to As_2S_3 material enables a strong mode confinement for a high integration density. Secondly, it is very easy to make a high quality, low loss channel waveguide by diffuse titanium strip into the $LiNbO_3$ substrate. The mode size of the diffused channel waveguide is well close to the mode size of a single mode fiber, which helps to minimize the fiber-to-chip coupling loss, as low as 0.5

dB per facet. And thirdly, the excellent birefringence property of $LiNbO_3$ substrate enables its high efficiency in parametric frequency conversions, which explores the good potential in the nonlinear applications by the hybrid As_2S_3-on-$LiNbO_3$ material platform.

Material	Kerr coefficient (n_2)	Lowest propagation loss at 1.55 μm	Lowest propagation loss at mid IR (4.8 μm)	Two photon absorption at 1.55 μm
ChG glass	3.8×10^{-18} m^2/W	0.2 dB/cm	0.33 dB/cm	None
Silicon	4×10^{-18} m^2/W	0.3 dB/cm	Non-transparent	0.8 cm/GW
Silica (SiO_2)	~100 times smaller than ChG glass	---	---	---

Table 1.2 Comparison of nonlinearity between As_2S_3, Si and SiO_2

1.3 Resonant cavity optical waveguide

Resonator based reconfigurable optical devices with feedback paths are attracting interest in recent years as compact on-chip active optic device components with various functions, such as modulators [7], tunable optical filters and multiplexers [8]. The resonant cavity optical waveguide can be realized by various structures, such as ring resonator, micro disk, micro sphere and grating Fabry-Perot cavity resonator. A resonant cavity optical waveguide consists of a feedback path and a coupler structure that only a partial of the incident light would be coupled into the cavity and the remained part would

be transmitted to the output port. At a certain wavelength, if the phase of the light propagating inside the cavity is the integral times of 2π, the light would be totally trapped inside the cavity. And this wavelength would be the resonant wavelength of an optical cavity waveguide. For the integrated planar resonant cavity optical waveguide, the commonly used structures are the ring resonator and the grating coupler cavity (Fig. 1.2).

A ring resonator waveguide is consisted of a straight bus waveguide, a ring bend waveguide and a directional coupler that connecting the bus and feedback path ring waveguide (Fig. 1.2 (a)). The incident light is input through the bus waveguide and partially coupled into the feedback ring waveguide. The coupled light inside the cavity propagates along a round-trip path and partially coupled back to the bus waveguide. The grating coupler cavity waveguide is consisted of two identical grating couplers with a straight long uniform waveguide in the middle as the feedback path (Fig. 1.2 (b)).

The grating coupler cavity waveguide is consisted of two identical grating couplers with a straight long uniform waveguide in the middle as the feedback path (Fig. 1.2 (b)). Compared to the ring resonator, the grating cavity waveguide uses a straight uniform waveguide as the feedback path cavity instead of a bend waveguide and this makes the structure with no concerns about the waveguide bend loss. Meanwhile, the ring resonator employs a directional coupler as the coupling region but the grating cavity just uses two identical grating reflector couplers. While the directional coupler requires a more precise control on the lithography process and the coupling performance is not

stable, the grating couplers have the advantages of strong coupling strength, compact device size and simpler lithography process.

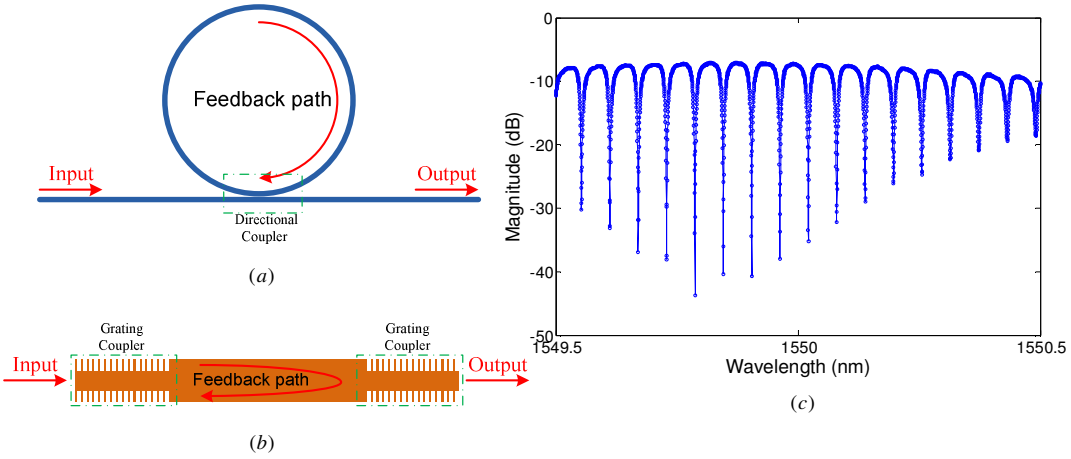

Fig. 1.2 (a) Ring resonator waveguide (b) Grating coupler cavity waveguide (c) An example of a spectral response of a resonant cavity waveguide

In terms of the all-optical nonlinear application, resonant cavity devices are favored for their easily tunable ability as a small change of refractive index in the material would lead to a shift for their resonance. Therefore, it is motivating to combine the As_2S_3-on-$LiNbO_3$ optical waveguide platform and the resonant cavity structure together for the integrated all-optical circuits.

1.4 Previous works

Parametric frequency conversion through four-wave mixing (FWM) was demonstrated by using a silicon micro-ring resonator [9]. Four-wave mixing is a

traditional nonlinear optical process in all-optical applications. Under a phase-matching condition, with the input of a signal light at wavelength λ_1 and an optical pump light at a different wavelength λ_2, an idler light is generated at a new wavelength λ_3 in which $\lambda_3=2(\lambda_2-\lambda_1)$. A 50-μm radius ring resonator was fabricated on silicon-on-insulator (SOI) material platform. With the help of the resonant-cavity enhancement, a 15-dB enhancement of FWM process was observed by using a pump power at 5 mW and a signal power at 100 μW. However, the nonlinear conversion efficiency inside the silicon ring resonator was limited by the absorption of light due to the free carriers generated inside the silicon material. On the contrary, the chalcogenide (ChG) glass is not limited by the free carrier absorption like silicon.

The first experimental resonant-cavity enhancement nonlinear process inside As_2S_3 material was reported by Hu [10]. A 30-μm radius micro-disk As_2S_3 waveguide was built on silica substrate. A photo-induced refractive index increase of 0.06 at 1550 nm was measured inside the As_2S_3 micro-disk cavity waveguide with an optical pump power of 18.6 dBm at the input.

The hybrid As_2S_3-on-$LiNbO_3$ vertically integrated ring resonator waveguide device was firstly demonstrated in 2009 [11]. The round-trip loss of the ring resonator with a circumference of 4.827 mm was 2.08 dB, which corresponds for a relatively high propagation loss of 4.3 dB/cm, which is not good for all-optical operations. Meanwhile, the coupling strength between Ti:$LiNbO_3$ bus and As_2S_3 ring waveguides was only 10%, as well as a small extinction ratio of only 5 dB, which is not favorable for a resonance-notch filter device. Finally, the ring response was only able to be measured at 1522 nm,

which is far away to the ideal telecom-band wavelength centered at 1555 nm. Therefore this hybrid As_2S_3-on-$LiNbO_3$ ring resonator waveguide needs to be improved in these aspects: a). propagation loss; b). coupling strength between bus waveguide and ring resonator; c). ring resonator response at telecommunication wavelength (1550 nm). d). extinction ratio of the ring response.

1.5 Organization of the dissertation

After the introduction in Chapter I, in Chapter II the fundamental theory of the electro-magnetic field, optical waveguide, coupled mode equation and nonlinear all-optical phenomena of wave propagation inside the waveguide, including self-phase modulation, cross-phase modulation and parametric processes, were introduced.
In Chapter III, the design process and simulation of the As_2S_3-on-$LiNbO_3$ resonant cavity waveguide were discussed. The design flows included the race-track ring resonator waveguide and the sidewall grating coupler cavity waveguide. The all-optical nonlinear applications based on the As_2S_3-on-$LiNbO_3$ resonant cavity devices were proposed and simulated.

In Chapter IV, the fabrication processes of the As_2S_3-on-$LiNbO_3$ resonant cavity waveguides were given in details. The optimization and processing development of the fabrication were covered. The fabrication processes include the thin film deposition, photo-lithography, E-beam writing lithography and etching.

In Chapter V, it was focused on the optical measurements and characterizations of the fabricated As_2S_3-on-$LiNbO_3$ resonant cavity devices. The performance of the measurement results would be fitted and compared to the design and simulations.

In Chapter VI, the conclusion of this dissertation thesis was given.

CHAPTER II

WAVEGUIDES AND NONLINEAR OPTICS THEORY

2.1 Background theoretical knowledge on optical waveguides

The optical waveguide covered in this dissertation is the thin-film waveguide which is formed when thin films are deposited on top of the substrate layer and the thin film index is higher than that of the substrate material. Generally, a cladding layer is also added on top of the thin film waveguide layer (Fig. 2.1).

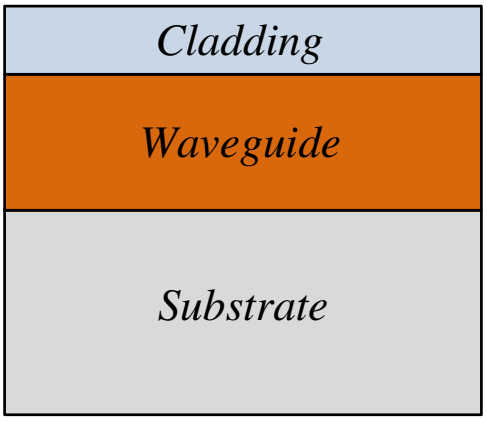

Fig. 2.1 Cross-section view of the thin film waveguide structure

The refractive index of the substrate, waveguide and cladding layers are denoted as n_s, n_f and n_c. The light can be guided inside the waveguide only if $n_f > n_s > n_c$ and the waveguide thin film thickness is above the critical thickness [12].

Wave equations were derived to solve the guided modes propagating inside the waveguide layer. Maxwell's equations in an isotropic and lossless material medium are written as:

$$\nabla \times \vec{E} = -\mu_0 \frac{\partial \vec{H}}{\partial t} \tag{2.1}$$

$$\nabla \times \vec{H} = \varepsilon_0 n^2 \frac{\partial \vec{E}}{\partial t} \tag{2.2}$$

where ε_0 and μ_0 are the dielectric permittivity and magnetic permeability of free space and n is the refractive index. If the optical wave propagates along the z direction and the propagation constant is β, the electromagnetic fields are written as

$$\vec{E} = E(x, y) \cdot \exp j(\omega t - \beta z) \tag{2.3}$$

$$\vec{H} = H(x, y) \cdot \exp j(\omega t - \beta z) \tag{2.4}$$

The two equations yield two different mode with the mutually orthogonal polarization states in which one is TE mode and the other is TM mode. The optical wave equations for TE mode are written as

$$\frac{\partial^2 E_y}{\partial x^2} + (k_0^2 n^2 - \beta^2) E_y = 0 \tag{2.5}$$

$$\begin{cases} H_y = -\dfrac{\beta}{\omega \mu_0} E_y \\ H_z = -\dfrac{1}{j\omega \mu_0} \dfrac{\partial E_y}{\partial x} \end{cases} \tag{2.6}$$

and for TM mode are written as

$$\frac{\partial^2 H_y}{\partial x^2} + (k_0^2 n^2 - \beta^2) H_y = 0 \tag{2.7}$$

$$\begin{cases} E_x = \dfrac{\beta}{\omega \varepsilon_0 n^2} H_y \\ E_z = \dfrac{1}{j\omega \varepsilon_0 n^2} \dfrac{\partial H_y}{\partial x} \end{cases} \tag{2.8}$$

The boundary conditions at the interfaces $x = -T$ and $x = 0$ along with the field solutions would lead to eigenvalue equations. The eigenvalue equations determine the propagation characteristics of the guided TE and TM modes inside the waveguide layer.

2.2 Step-index 2-D waveguides

A step-index 2-D optical waveguide has the refractive index profile in Fig. 2.2.

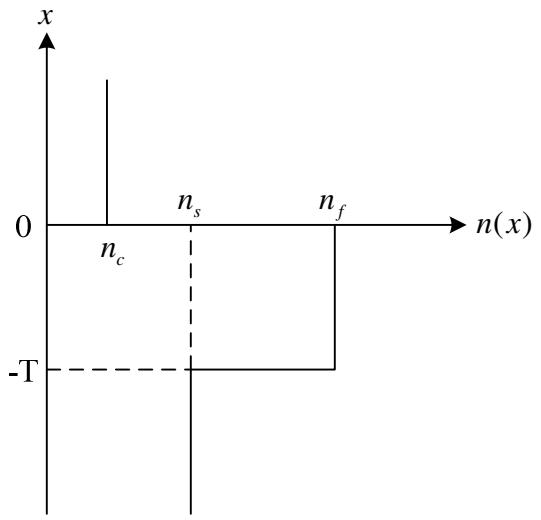

Fig. 2.2 Step-index type 2-D optical waveguide refractive index profile

The TE mode optical field solution from the TE mode wave equation can be express as:

$$\begin{cases} E_y = E_c \exp(-\gamma_c x), x > 0 & \text{(in the cover)} \\ E_y = E_f \cos(k_x x + \phi_c), -T < x < 0 & \text{(in the guiding layer)} \\ E_y = E_s \exp\{\gamma_s (x+T)\}, x < -T & \text{(in the substrate)} \end{cases} \tag{2.9}$$

where the x-direction propagation constants are expressed in terms of the index N, as given in the followings: $\gamma_c = k_0\sqrt{N^2 - n_c^{\,2}}$, $k_x = k_0\sqrt{n_f^{\,2} - N^2}$ and $\gamma_s = k_0\sqrt{N^2 - n_s^{\,2}}$.

The tangential field components Ey and Hz should follow the boundary condition and must be continuous at the interface x=0 yields

$$\begin{cases} E_c = E_f \cos\phi_c \\ \tan\phi_c = \gamma_c / k_x \end{cases} \tag{2.10}$$

and at x=-T yields

$$\begin{cases} E_s = E_f \cos(k_x T - \phi_c) \\ \tan(k_x T - \phi_c) = \gamma_s / k_x \end{cases} \tag{2.11}$$

If the arbitrary coefficients in the preceding relations are eliminated, the eigenvalue equation results in

$$k_x T = (m+1)\pi - \tan^{-1}(\frac{k_x}{\gamma_s}) - \tan^{-1}(\frac{k_x}{\gamma_c}) \tag{2.12}$$

where m is the mode number value in 0, 1, 2…….

If the indices of the waveguide material and the guide layer thickness T are given, from the equation, k_x can be obtained. The effective index of N can be calculated by substituting k_x into equation for the guided mode. Here, N must be a discrete number

in the range of $n_s<N<n_f$ as the mode number is a positive integer. The fundamental mode is the guided mode with the mode number of 0 and has the largest effective index. For the higher order modes, N is close to n_s.

For the TM mode analysis, the method is the same as for the TE mode. The eigenvalue equation for the TM guided mode is written as:

$$k_x T = (m+1)\pi - \tan^{-1}(\frac{n_s}{n_f})^2(\frac{k_x}{\gamma_s}) - \tan^{-1}(\frac{n_c}{n_f})^2(\frac{k_x}{\gamma_c}) \tag{2.13}$$

Hy and Ez are continuous at the waveguide interface and a square of the index ratio is additionally included in the eigenvalue equation.

2.3 Graded-index 2-D waveguides

Low-loss channel waveguide can be got by diffuse the titanium metal or ion exchange into the birefringence crystal substrate lithium niobate ($LiNbO_3$). The wave equation for such a graded-index 2-D waveguide is generally given by

$$\frac{\partial^2 E_y}{\partial x^2} + (k_0^2 n^2(x) - \beta^2)E_y = 0 \tag{2.14}$$

There is a widely used approximation methods to solve the wave proceeding equation numerically which is called ray-approximation method.

The index distribution of the diffused waveguide can be written in the form as:

$$n(x) = n_s + \Delta n \cdot f(x/d) \tag{2.15}$$

where ns is the substrate index. The index profile of the graded-index waveguide is shown in Fig 2.3.

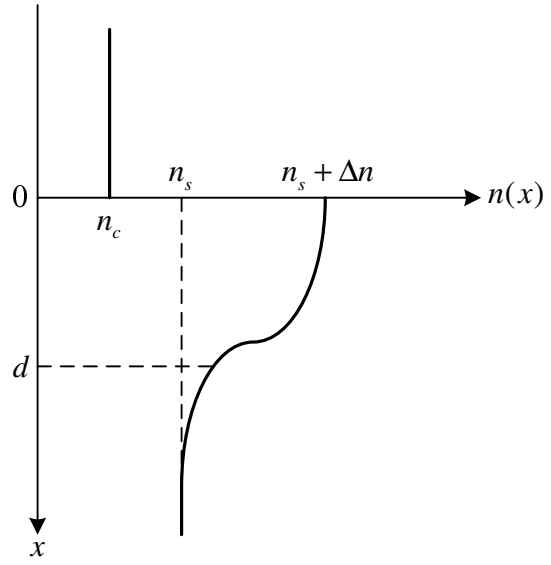

Fig. 2.3 Graded-index type 2-D optical waveguide refractive index profile

The index reaches the maximum value of $(n_s + \Delta n)$ at the surface x=0. The diffusion depth is denoted by d in which the value of $f(x/d)$ equals $1/e$. The ray arc wave in the diffused waveguide is approximated by a combination of the piecewise linear paths with an infinitesimal propagation distance Δz. The angle θ_i, as of the graded-index distribution, changes gradually between the wave normal and the z direction according to the equation [Fig. 2.4]

$$\theta_i = \cos^{-1}(N / n(x_i)) \tag{2.16}$$

where N is the effective index of the guided mode. The depth of the i th segment is given by

$$\Delta x_i = \Delta z \tan \theta_i \tag{2.17}$$

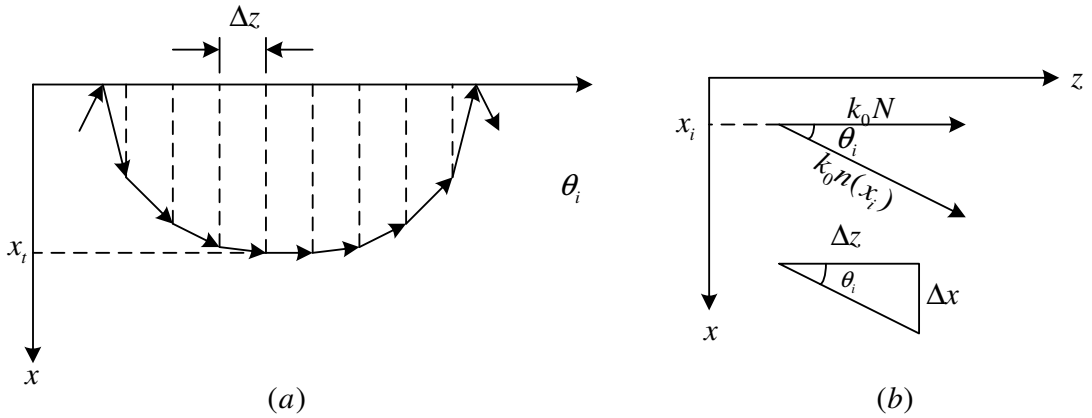

Fig. 2.4 (a) Trajectory of the optical ray (b) Wave-vector diagram in i th segment

x_t is regarded as the effective waveguide thickness of the diffused waveguide. The incremental transverse phase shift across Δx_i is:

$$\phi_i = k_0 n(x_i)\sin\theta_i \cdot \Delta x_i = k_0\sqrt{n^2(x_i) - N^2}\cdot \Delta x_i \tag{2.18}$$

The wave also undergoes the phase shift due to the total internal reflection at the guide surface. The reflection of the plane wave at the interface between two different dielectric materials is characterized by Fresnel equations and yields as:

$$\begin{cases} 2\phi_0 = \pi & \text{at } x = 0 \\ 2\phi_t = \pi/2 & \text{at } x = x_t \end{cases} \tag{2.19}$$

The existence of the guided modes needs that the total transverse phase shift for one round trip across the waveguide must be an integral multiple of 2π . And this results in the eigenvalue equation:

$$\sum_i \phi_i - 2\phi_0 - 2\phi_t = 2m\pi \tag{2.20}$$

where the mode number m=0, 1, 2…… Using equation (2.20), the first term on the left-hand side of the proceeding equation is expressed as:

$$\sum_i \phi_i = 2k_0 \int_0^{x_t} \sqrt{n^2(x) - N^2}\, dx \tag{2.21}$$

Considering $\Delta n \ll n_s$, equation (2.15) is approximated and can be written as:

$$n^2(x) \approx n_s^2 + (n_f^2 - n_s^2) f(x/d) \tag{2.22}$$

where $n_f = (n_s + \Delta n)$ is the maximum index of the waveguide. If d corresponds to the thickness T of the step-index 2-D waveguide, the normalized diffusion depth can be defined by

$$V_d = k_0 d \sqrt{n_f^2 - n_s^2} \tag{2.23}$$

A normalized frequency b can be defined as $b = (N^2 - n_s^2)/(n_f^2 - n_s^2)$, the eigenvalue equation (2.20) can be re-written in the normalized expression:

$$2V_d \int_0^{\zeta_t} \sqrt{f(\zeta) - b}\, d\zeta = (2m + \frac{3}{2})\pi \tag{2.24}$$

where $\zeta = x/d, \zeta_t = x_t/d$ and $b = f(\zeta_t)$. For the Ti-diffused LiNbO3 waveguide, the index distribution function is $f(\zeta) = \exp(-\zeta^2)$. The proceeding normalized eigenvalue equation can be solved numerically then to get the number of guided modes supported, as well as their electrical field distribution.

2.4 Coupled mode theory in the waveguides

The optical mode propagating along the uniform waveguide was discussed. However, in a lot of cases, the modes propagate with coupling. In our As_2S_3-on-$LiNbO_3$ waveguide, the optical mode would first propagate inside the diffused $LiNbO_3$ channel waveguide and then coupled to the higher refractive index As_2S_3 planar waveguide. Therefore, in this section, the basic concept and background of the coupled mode theory inside the waveguide would be discussed.

Guided modes exist in a lossless waveguide which is uniform along the propagation direction. These are normal modes defined by the waveguide structure and its boundary conditions. An orthogonal relationship holds among the modes. Thus, each mode propagates without mutual coupling and carries the power independently. This situation holds in the unperturbed waveguide [Fig 2.5 (a)].

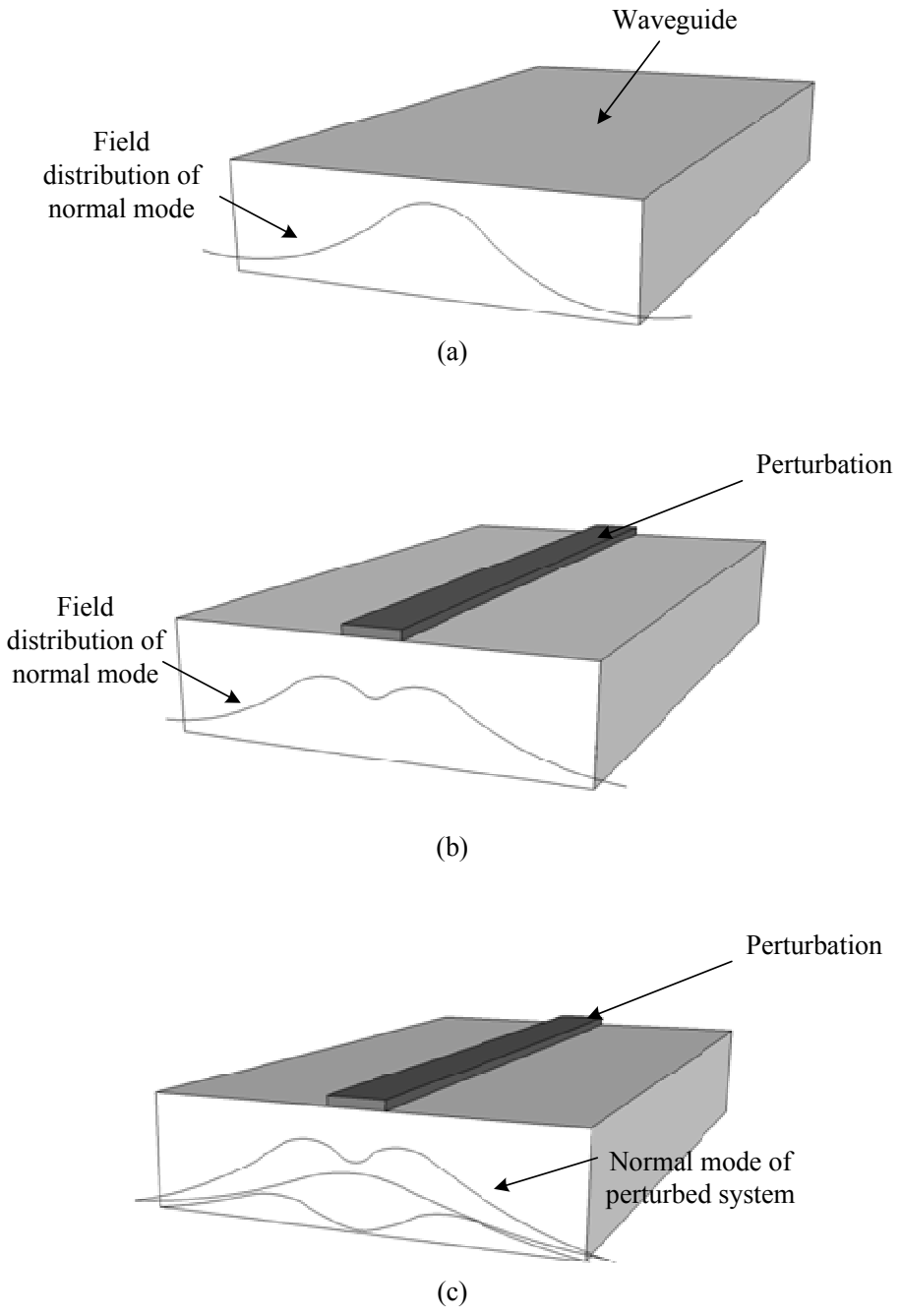

Fig. 2.5 (a) Unperturbed system and its normal mode (b) Perturbed system and its normal mode (c) Two normal modes of unperturbed system and a normal mode of perturbed system

In the perturbed waveguide, normal modes of unperturbed guides are not independent, and are coupled mutually. For analyzing optical wave propagation in a perturbed waveguide system, the method of coupled mode theory is used. The method is to express the perturbed wave behavior by summation of normal modes in the unperturbed waveguide system. This method only gives approximate solutions but is straightforward and simple. The solution approximation is very good and thus the coupled mode theory is a method that can be used to describe the wave behavior in a perturbed waveguide system by means of the known normal modes of the unperturbed system.

Considering there are two waveguide I and II as shown in Fig. 2.6 (a). When they are separate enough from each other, two normal modes, a and b, propagate independently on each waveguide with field ψ_a and ψ_b, and with propagation constants β_a and β_b ($\beta_b > \beta_a$). When the waveguides are uniformly coupled (perturbed) by reducing the separation, the original normal modes ψ_a and ψ_b no longer exist, and two new normal modes ψ_e and ψ_o propagate along a coupled waveguide system consisting of waveguide I and II (Fig. 2.6 (b)).

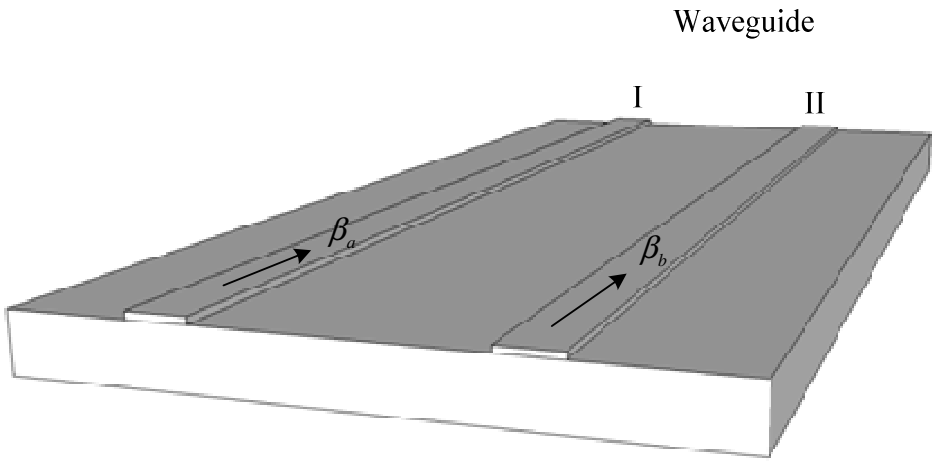

(a)

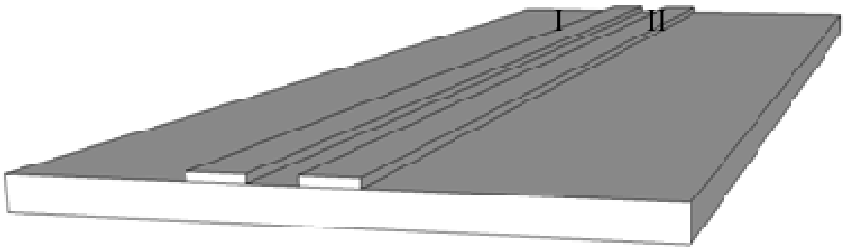

(b)

Fig. 2.6 (a) Normal modes in two uncoupled waveguides (b) Two normal modes in a coupled waveguide system

ψ_e and ψ_o correspond to a symmetric mode and an asymmetric mode respectively. Propagation constants of these modes are β_e, larger than β_b, and β_o, smaller than β_a. ψ_e and ψ_o can be excited independently by an appropriate method. Depending on the excitation condition, the two modes are excited at the same time and

yield a beat. Wave power transfers back and forth periodically between waveguide I and II. The coupling effect appears stronger if β_a and β_b are close to each other.

Optical wave ψ_a and ψ_b propagating along the coupled waveguides I and II are expressed as:

$$\begin{cases} \psi_a(x,y,z,t) = A(z)e^{-j\beta_a z} f_a(x,y)e^{j\omega t} \\ \psi_b(x,y,z,t) = B(z)e^{-j\beta_b z} f_b(x,y)e^{j\omega t} \end{cases} \tag{2.25}$$

where f_a and f_b are field distribution functions that are normalized by power flow over a cross section. If coupling between I and II is reduced to zero, ψ_a and ψ_b are reduced to two independent original normal modes. $A(z)$ and $B(z)$ are reduced to constants. Here, coupling is assumed and therefore, $A(z)$ and $B(z)$ are no longer independent. The coupled mode equations only include functions of z as follows:

$$\begin{cases} \pm\dfrac{dA(z)}{dz} = -j\kappa_{ab}B(z)e^{-j(\beta_b-\beta_a)z} \\ \pm\dfrac{dB(z)}{dz} = -j\kappa_{ba}A(z)e^{+j(\beta_b-\beta_a)z} \end{cases} \tag{2.26}$$

where κ_{ab} and κ_{ba} are coupling coefficients between two modes. The term $e^{\pm j(\beta_b-\beta_a)z}$ corresponds to the phase-constant mismatching of the modes. When $\kappa_{ab} = \kappa_{ba} = 0$, in the equation Eq., they are reduced to $A(z) = A_0$ and $B(z) = B_0$. ψ_a and ψ_b are reduced to the two original waves. The coupling coefficient is a measure for spatial overlapping of normal modes over dielectric constant increments $\Delta\varepsilon$ in waveguide II and is calculated by the following integral:

$$\kappa_{ab} = c \iint_{II} f_a^* \Delta\varepsilon f_b dxdy \tag{2.27}$$

where the integration range is the cross section of waveguide II, and c is a constant related to the normalization of ψ_a and ψ_b. The relation between κ_{ab} and κ_{ba} is $\kappa_{ab} = \kappa_{ba}^*$.

Behavior of coupled waves can be determined by obtaining propagation constants of the waveguide system from the coupled mode equation. Here, the case of unidirectional propagation would be discussed, as shown in Fig. 2.7.

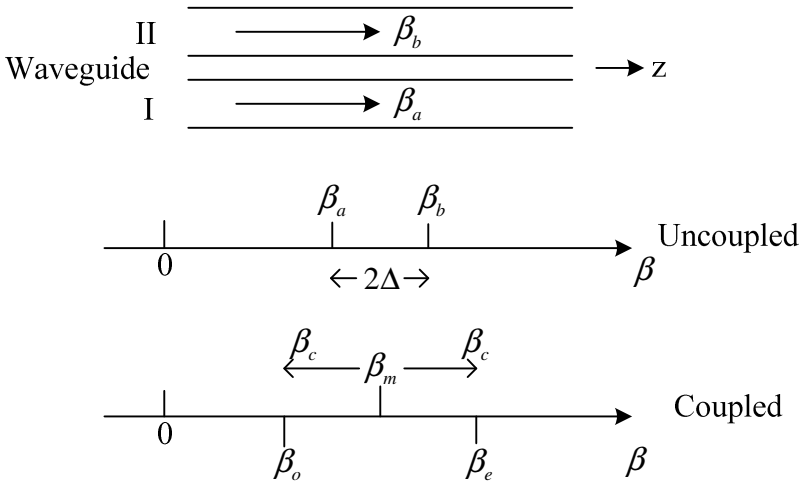

Fig. 2.7 Propagation constants in the case of co-directional coupling

Under the unidirectional case ($\beta_a > 0$, $\beta_b > 0$), the coupled mode equation is reduced to

$$\begin{cases} \dfrac{dA(z)}{dz} = -j\kappa B(z) e^{-j(\beta_b - \beta_a)z} \\ \dfrac{dB(z)}{dz} = -j\kappa A(z) e^{+j(\beta_b - \beta_a)z} \end{cases} \tag{2.28}$$

where $\kappa_{ab} = \kappa_{ba}^{*} = \kappa$. By introducing a new quantity $2\Delta \equiv \beta_b - \beta_a$ for convenience, the equation (2.28) becomes

$$\begin{cases} A(z) = Ae^{-\gamma z}e^{-j\Delta z} \\ B(z) = Be^{-\gamma z}e^{+j\Delta z} \end{cases} \tag{2.29}$$

and a quadratic equation for γ is derived and roots are obtained as:

$$\gamma = \pm\sqrt{\kappa^2 + \Delta^2} \tag{2.30}$$

The solutions of the two unidirectional modes are then re-written as follows:

$$\begin{cases} A(z) = [A_e e^{-j\sqrt{\kappa^2+\Delta^2}z} + A_o e^{+j\sqrt{\kappa^2+\Delta^2}z}]e^{-j\Delta z} \\ B(z) = [\dfrac{\kappa A_e}{\sqrt{\kappa^2+\Delta^2}-\Delta} e^{-j\sqrt{\kappa^2+\Delta^2}z} + \dfrac{-\kappa A_o}{\sqrt{\kappa^2+\Delta^2}+\Delta} e^{+j\sqrt{\kappa^2+\Delta^2}z}]e^{+j\Delta z} \end{cases} \tag{2.31}$$

The optical waves of the two unidirectional modes are derived:

$$\begin{aligned} \psi_a(x,y,z,t) &= [A_e e^{-j\beta_e z} + A_o e^{-j\beta_o z}] f_a(x,y) e^{j\omega t} \\ \psi_b(x,y,z,t) &= [B_e e^{-j\beta_e z} + B_o e^{-j\beta_o z}] f_b(x,y) e^{j\omega t} \end{aligned} \tag{2.32}$$

where the ratio of A_e and B_e is a positive constant and the ratio of A_o and B_o is a negative constant. The following relations are also used:

$$\left.\begin{matrix} \beta_e \\ \beta_o \end{matrix}\right\} = \beta_m \pm \beta_c \tag{2.33}$$

$$\beta_m \equiv (\beta_a + \beta_b)/2, \beta_c \equiv \sqrt{\kappa^2 + \Delta^2} \tag{2.34}$$

Equation (2.33) and (2.34) indicate that optical waves ψ_a and ψ_b propagating along waveguides I and II are expressed by a linear combination of two waves with the

propagation constants β_e and β_o. Therefore, β_e and β_o are the propagation constants of the coupled mode system, and ψ_e and ψ_o correspond to $A_e f_a + B_e f_b$ and $A_o f_a + B_o f_b$.

When the boundary conditions are $A(0) = 1$ and $B(0) = 0$ at $z = 0$ (which means the wave is excited only at waveguide I), $A(z)$ and $B(z)$ are written as

$$\begin{cases} A(z) = e^{-j\Delta z}\{\cos\beta_c z + j\dfrac{\Delta}{\beta_c}\sin\beta_c z\} \\ B(z) = e^{+j\Delta z}\dfrac{-j\kappa}{\beta_c}\sin\beta_c z \end{cases} \tag{2.35}$$

Since f_a and f_b are expressed by means of a normalized power flow, the power flow along waveguides I and II are given by $|A(z)|^2$ and $|B(z)|^2$ respectively. And thus the proceeding equations can be re-written in the power form as follows:

$$\begin{cases} \dfrac{|A(z)|^2}{|A(0)|^2} = 1 - F\sin^2\beta_c z \\ \dfrac{|B(z)|^2}{|A(0)|^2} = F\sin^2\beta_c z \end{cases} \tag{2.36}$$

where

$$F = \left(\frac{\kappa}{\beta_c}\right)^2 = \frac{1}{1 + (\Delta/\kappa)^2} \tag{2.37}$$

The power of waves propagating along the two waveguides varies or beats periodically. F means the maximum transfer of optical power from waveguide I to II. The maximum power transfer occurs at distance L, which is given as

$$L = \frac{\pi}{2\beta_c} \tag{2.38}$$

This L is called the coupling length.

2.5 Nonlinearity in the optical waveguides

Nonlinear optics is a branch of optics that describes the behavior of light inside the nonlinear media. Inside the nonlinear media, the optical light would response nonlinearly according to the electrical field intensity. The amorphous As_2S_3 glass is a very good material as the nonlinear medium for its relatively large nonlinearity coefficient at a wide range of bandwidth from near IR to mid IR. Therefore, the As_2S_3 material waveguide is an ideal platform for various nonlinear optical applications. The two most common nonlinear optical processes inside the As_2S_3 waveguide are self-phase modulation (SPM), and cross-phase modulation (XPM).

Self-phase modulation (SPM) is a phenomenon occurring in nonlinear material media (such as As_2S_3 waveguide) when the refractive index of the media is dependent on the intensity of the optical pulse propagating inside the material. Therefore self-phase modulation would lead to spectral broadening of the optical pulse as its phase is modulated when propagating along the varying refractive index [13].

The self-phase modulation inside the optical waveguide was firstly demonstrated with the optical fiber. With the normalized amplitude $U(z,T)$, the propagation equation inside the waveguide can be written as:

$$\frac{\partial U}{\partial z} = \frac{i}{L_{NL}} \exp(-\alpha z) \left|U\right|^2 U \tag{2.39}$$

where α is the fiber loss. The nonlinear length is defined as:

$$L_{NL} = (\gamma P_0)^{-1} \tag{2.40}$$

where P_0 is the peak power. The term γ is related to the material nonlinear-index coefficient n_2 by equation:

$$\gamma = \frac{n_2 \omega_0}{c A_{eff}} \tag{2.41}$$

where ω_0 is the frequency, c is the light speed and A_{eff} is the effective area of the optical mode. The propagation equation is solved to obtain

$$U(z,T) = U(0,T)\exp[i\phi_{NL}(z,T)] \tag{2.42}$$

where $U(0,T)$ is the field amplitude at $z = 0$ and the nonlinear phase is written as:

$$\phi_{NL}(z,T) = \left|U(0,T)\right|^2 (z_{eff} / L_{NL}) \tag{2.43}$$

with the effective propagation length:

$$z_{eff} = [1 - \exp(-\alpha z)] / \alpha \tag{2.44}$$

The equation (2.42) shows that the pulse shape governed by $\left|U(z,T)\right|^2$ remains unchanged while the SPM gives the rise to the intensity-dependent phase shift. The nonlinear phase shift $\phi_{NL}(z,T)$ increases with the propagated distance z. The term z_{eff} plays the role of an effective distance which is smaller than z due to the loss. If α is zero, the waveguide is lossless and $z_{eff} = z$. The maximum phase shift occurs at the pulse center located at $T = 0$ and is given by

$$\phi_{\max} = z_{eff} / L_{NL} = \gamma P_0 z_{eff} \tag{2.45}$$

The spectral broadening which is induced by SPM is a consequence of the time dependence of the nonlinear phase shift $\phi_{NL}(z,T)$. A temporally varying phase implies that the instantaneous optical frequency differs across the pulse from its center value ω_0. This difference is given by:

$$\delta\omega(T) = -\frac{\partial\phi_{NL}}{\partial T} = -\frac{\partial}{\partial T}(|U(0,T)|^2)\frac{z_{eff}}{L_{NL}} \tag{2.46}$$

The new frequency components are continuously generated as the pulse propagates along the waveguide. These SPM generated frequency components broaden the spectrum over its initial width at $z = 0$. The extent of the spectral broadening depends on the pulse shape. The SPM induced chirp for a super-Gaussian pulse with the incident field $U(0,T) = \exp[-\frac{1+iC}{2}(\frac{T}{T_0})^{2m}]$ is:

$$\delta\omega(T) = \frac{2m}{T_0}\frac{z_{eff}}{L_{NL}}(\frac{T}{T_0})^{2m-1}\exp[-(\frac{T}{T_0})^{2m}] \tag{2.47}$$

where parameter m is 1 for a Gaussian pulse.

The SPM induced magnitude spectral broadening can be investigated by obtaining the shape of the pulse spectrum $S(\omega)$ which is calculated by taking the Fourier transform $S(\omega) = \left|\tilde{U}(z,\omega)\right|^2$,

$$S(\omega) = \left|\int_{-\infty}^{\infty} U(0,T)\exp[i\phi_{NL}(z,T) + i(\omega-\omega_0)T]dT\right|^2 \tag{2.48}$$

The maximum nonlinear phase shift $\phi_{\max}$ increases linearly with the incident power P_0 under the fixed length of the waveguide. And the pulse spectrum shape also revolves with the maximum phase shift.

When two optical waves co-propagate inside the waveguide, they can interact with each other through Kerr nonlinearity. Under appropriate conditions (such as phase matching), new waves could be generated through nonlinear phenomenon, for which four wave mixing is a typical example. However, there's always a nonlinear process occurring when there are two incident optical waves co-propagating inside the nonlinear media which is known as cross-phase modulation (XPM). Cross-phase modulation is always accompanied by self-phase modulation. The difference between XPM and SPM is that in cross-phase modulation, the effective refractive index of a wave depends not only on its own intensity but also on the intensity of the other co-propagating wave.

The rapidly varying part of the electric field of the co-propagating two waves can be separated by writing it in the form:

$$E(r,t) = \frac{1}{2}\hat{x}[E_1 \exp(-i\omega_1 t) + E_2 \exp(-i\omega_2 t)] + c.c \tag{2.49}$$

where $\hat{x}$ is the polarization unit vector, ω_1 and ω_2 are the center frequencies of the two pulses, and the corresponding amplitudes E_1 and E_2 are assumed to be slowly varying functions of time. The origin of the XPM can be derived from the equation:

$$\begin{aligned} P_{NL}(r,t) = \frac{1}{2}\hat{x}\{&P_{NL}(\omega_1)\exp(-i\omega_1 t) + P_{NL}(\omega_2)\exp(-i\omega_2 t) \\ &+ P_{NL}(2\omega_1 - \omega_2)\exp[(-i(2\omega_1 - \omega_2)t] \\ &+ P_{NL}(2\omega_2 - \omega_1)\exp[(-i(2\omega_2 - \omega_1)t]\} + c.c \end{aligned} \tag{2.50}$$

where

$$P_{NL}(\omega_1) = \chi_{eff}(|E_1|^2 + 2|E_2|^2)E_1, \tag{2.51}$$
$$P_{NL}(\omega_2) = \chi_{eff}(|E_2|^2 + 2|E_1|^2)E_2,$$
$$P_{NL}(2\omega_1 - \omega_2) = \chi_{eff}E_1^2E_2^*,$$
$$P_{NL}(2\omega_2 - \omega_1) = \chi_{eff}E_2^2E_1^*,$$

and

$$\chi_{eff} = \frac{3\varepsilon_0}{4}\chi^{(3)}_{xxxx} \tag{2.52}$$

The new frequency terms $2\omega_1 - \omega_2$ and $2\omega_2 - \omega_1$ result from the phenomenon of four-wave mixing which would not be discussed here. It is necessary to satisfy the phase-matching condition if the new frequency components are to be significantly buildup. If the phase-matching condition does not occur, only the remaining two terms provide a nonlinear contribution to the refractive index.

This can be seen by writing $P_{NL}(\omega_j)$ in the form ($j = 1,2$)

$$P_{NL}(\omega_j) = \varepsilon_0\varepsilon_j^{NL}E_j, \tag{2.53}$$

and combining it with the linear part so that the total induced polarization is given by

$$P(\omega_j) = \varepsilon_0\varepsilon_j E_j \tag{2.54}$$

where

$$\varepsilon_j = \varepsilon_j^L + \varepsilon_j^{NL} = (n_j^L + \Delta n_j)^2 \tag{2.55}$$

n_j^L is the linear part of the refractive index and Δn_j is the change induced by the third-order nonlinear effects. Using the approximation $\Delta n_j \ll n_j^L$, the nonlinear part of the refractive index is given by

$$\Delta n_j = \varepsilon_j^{NL} / 2n_j = n_2(\left|E_j\right|^2 + 2\left|E_{3-j}\right|^2), \tag{2.56}$$

where the nonlinear-index coefficient

$$n_2 = \frac{3}{8n}\mathrm{Re}(\chi_{xxxx}^{(3)}). \tag{2.57}$$

Equation (2.56) shows that the refractive index of an optical wave depends not only on the intensity of that wave but also on the intensity of other co-propagating waves. As the optical wave propagates inside the waveguide, it acquires an intensity-dependent nonlinear phase given by

$$\phi_j^{NL} = \frac{\omega_j z}{c}\Delta n_j = \frac{\omega_j z n_2}{c}[\left|E_j\right|^2 + 2\left|E_{3-j}\right|^2], \tag{2.58}$$

where $j = 1, 2$. The first term is responsible for the self-phase modulation (SPM) discussed in previous section. The second term results from phase modulation of one wave by the co-propagating wave and is responsible for XPM. The factor of 2 on the second term shows that XPM is twice as effective as SPM for the same incident intensity.

CHAPTER III

DEVICE DESIGN AND SIMULATION[*]

3.1 General device design process

The design process of the integrated electro-optical waveguide devices starts from the high-level schematic simulations which defined the purpose or functionality of the designed device. After determining the materials and substrates used for building the waveguides, physical-layer simulations with commercial software packages would be made to calculate the detailed waveguide parameters, i.e. waveguide width, thickness and cladding layers, which are optimized for the specific requirements, such as single mode guiding waveguide or the premium mode confinement factors.

---

[*] Part of this chapter is reprinted by the permission from "Two-stage taper enhanced ultra-high Q As_2S_3 ring resonator on $LiNbO_3$" by Yifeng Zhou, Xin Xia, William T. Snider, Jaehyun Kim, Qi Chen, Wee C. Tan and Christi Madsen, IEEE Photonics Technology Letters, Vol. 23, No. 17, copyright 2011 by IEEE.

[*] Part of this chapter is reprinted by the permission from "Fabrication and measurement of sidewall gratings integrated in hybrid As_2S_3-Ti:$LiNbO_3$ optical waveguides" by Xin Wang, Yifeng Zhou and Christi Madsen, Journal of Lightwave Technology, Vol. 21, Issue 17, copyright 2014 by IEEE.

The next step is to define the higher-level waveguide structure based on the simulated 2-D waveguide profile. In our research projects, the waveguide structure includes straight waveguides, race-track ring resonator waveguides and side-wall grating coupler waveguides. For each waveguide structure, corresponded simulations are made to optimize the waveguide device performance. For example, the ring resonator waveguide simulations include the coupling region design and bend loss simulation. The details about different waveguide device design and simulation would be given in the following sections.

After the simulation process, the fabrication process would be considered to realize the design structure. The fabrication process involves with the substrate sample preparation, thin film material deposition, lithography patterning and etching. For different material combinations and waveguide structure design, different fabrication procedures are employed and optimized. For instance, the ring resonator waveguide only uses photo-lithography to define the pattern because the minimum feature size of the waveguide is about 1~1.5 μm. However, the side-wall grating coupler waveguide requires the E-beam writing lithography as its minimum device size is smaller than 400 nm.

Optical measurement is the last step to test the optical performance of the designed and fabricated waveguides. Normally, the fabricated waveguides would be inspected by optical microscope and scanning electron microscopy (SEM) to make sure the waveguides look good after the fabrication process and all the physical parameters of the design are realized. If the optical measurement gives a differed or non-satisfactory

result compared to the simulation result, we would re-start from the initial design and simulation process to correct the potential un-intended factors that we do not take into considerations before.

3.2 As_2S_3-on-$LiNbO_3$ 2-D waveguide design and simulation

As mentioned in Chapter I, the material platform combination of As_2S_3 ridge waveguide on $LiNbO_3$ substrate has the unique benefits including: the higher refractive index of As_2S_3 on much lower index $LiNbO_3$ enabling the compact bend waveguide structure; the relatively high material nonlinear coefficient of As_2S_3 over other materials; the electro-optical tuning capability inside the $LiNbO_3$ substrate; and the easy low-loss fiber-chip butt coupling.

In Chapter II, the numerical methods to calculate the optical mode field distribution inside the waveguide were discussed. However, such methods are normally not accurate enough to meet the current device design requirements. Furthermore, our integrated waveguide is based on the combined material platforms which are also too complicated to be solved by the relatively simple theoretic mathematical models. Here, a commercially available optical waveguide software package, Fimmwave (from Photon Design) is used to numerically calculate the optical field distribution, mode confinement factor and the mode effective index, based on the waveguide geometry and materials.

The simplest waveguide structure of As_2S_3-on-$LiNbO_3$ substrate is illustrated in Fig. 3.1.

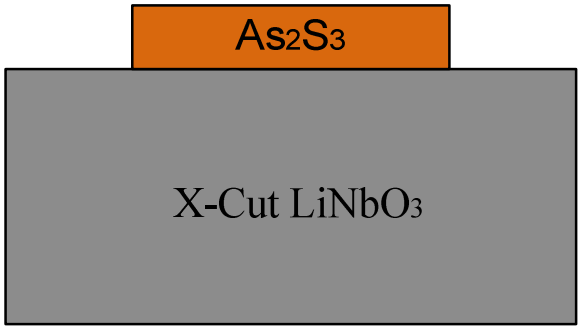

Fig. 3.1 Ridge As_2S_3 waveguide on X-cut $LiNbO_3$ substrate

To minimize the mode propagation loss, only single mode waveguides are interested to us. During the design process, the As_2S_3 waveguide structure was designed to only support fundamental TE_{00} or TM_{00} mode, depending on the polarization needs. At the same time, a higher mode confinement factor inside the As_2S_3 waveguide is desired for the nonlinear application of the As_2S_3 material. Single mode TE and TM As_2S_3-on-$LiNbO_3$ waveguides are designed, shown in Fig. 3.2.

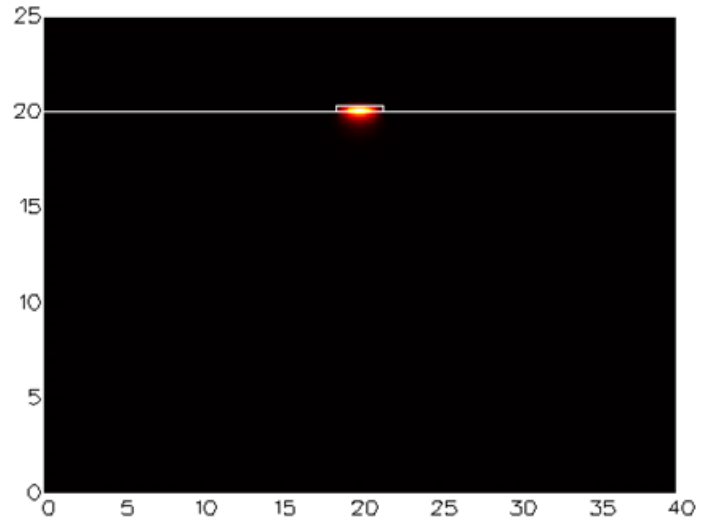

(a)

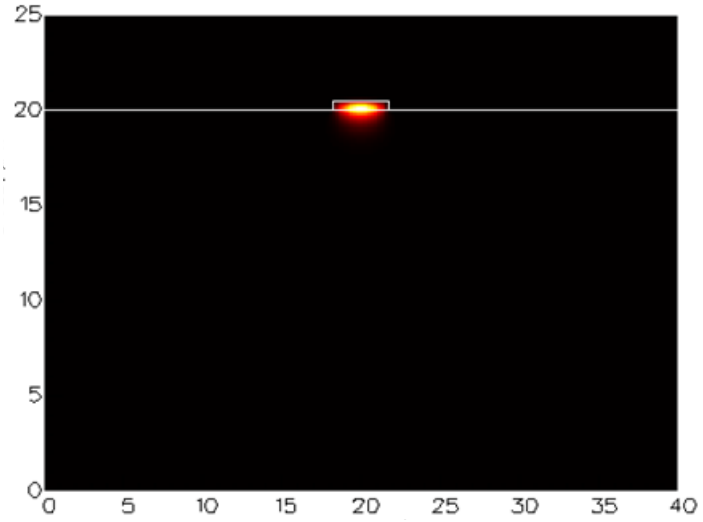

(b)

Fig. 3.2 (a) Fundamental TE_{00} mode intensity distribution of As_2S_3-on-$LiNbO_3$ waveguide (b) Fundamental TM_{00} mode intensity distribution of As_2S_3-on-$LiNbO_3$ waveguide

The designed fundamental TE As_2S_3-on-$LiNbO_3$ waveguide has the width of 3 μm and the thickness of 0.3 μm. The mode confinement factor inside the As_2S_3 material is 41.6% with an effective mode area of 2.57 μm^2. The mode effective index is 2.15648.

At the same time, the designed fundamental TM As_2S_3-on-$LiNbO_3$ waveguide has the width of 3.5 μm and the thickness of 0.47 μm. The mode confinement factor inside the As_2S_3 material is 38.2% with an effective mode area of 4.05 μm^2. The mode effective index is 2.22545.

This initial design of the 2-D As_2S_3-on-$LiNbO_3$ waveguide profile is simple but critical for the later designed and fabricated optical waveguide devices because all of these waveguides are based on the fundamental TE and TM optical waveguide modes.

3.3 As_2S_3-Ti:$LiNbO_3$ taper coupler waveguide design

3.3.1 Super mode theory and simulation model

One of the advantage of using $LiNbO_3$ as substrate is the easy low loss coupling between the single mode fiber (SMF) and Ti diffused $LiNbO_3$ channel waveguide. However, our As_2S_3-on-$LiNbO_3$ hybrid waveguides require the optical energy finally propagating inside the As_2S_3 material. Therefore, a taper waveguide structure must be designed to efficiently couple the light from Ti:$LiNbO_3$ channel waveguide into the As_2S_3-on-$LiNbO_3$ waveguide. A schematic overview of the As_2S_3-Ti:$LiNbO_3$ taper waveguide is shown in Fig. 3.3 [14].

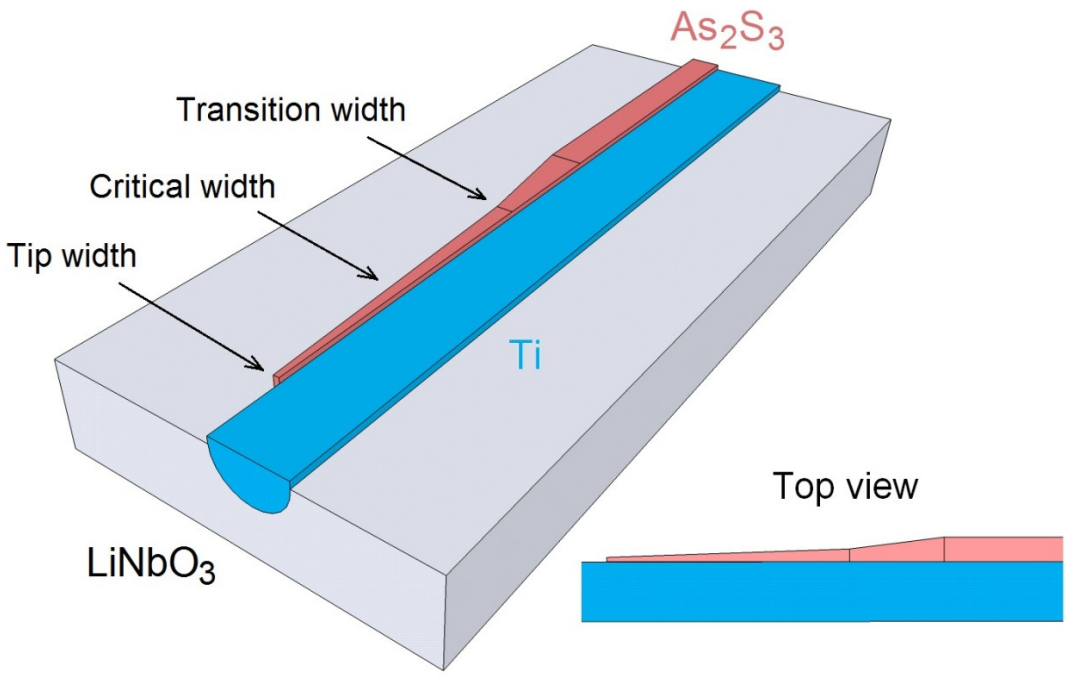

Fig. 3.3 Configuration of the As_2S_3-Ti:$LiNbO_3$ taper coupler and its top view

Compared to our taper coupler structure, generally the directional coupler is the simplest optical coupling structure by transferring energy between two waveguides. However, in the real world, its coupling efficiency is fairly low because of phase mismatch and the low tolerance to the fabrication errors. The taper coupler waveguide is much simpler in design and fabrication.

The working principle of the taper coupler is fairly clear and straightforward. The taper coupler is composed of two parallel waveguides placed in a very close proximity. One is uniform at one end whereas at the other end, the waveguide width is gradually varied. Two ends of the taper match the wave guiding properties of two waveguides.

And so the optical mode is transformed gradually from one into another during propagation in the taper.

Sometime the taper coupler is also called adiabatic coupler, if the taper waveguide can be assumed as infinitely long. For the adiabatic taper, 100% of optical mode can be transferred from one waveguide to the other waveguide.

However, in practice, we cannot make a waveguide infinitely long. A balance must be achieved between the taper waveguide length and the coupling efficiency. Also, in a lot of cases, 100% coupling is not desired. Here, a super mode theory is used to numerically evaluate the taper coupler waveguide performance and provide the guidelines in design such waveguide structure in our devices.

As discussed in Chapter II, the coupled mode equations analyze the coupled waveguides by taking one waveguide as the subject and studying the influence of the perturbation imposed by the presence of the other one. A taper waveguide, which consists of two adjacent waveguide, can also be regarded as a modified directional coupler.

Compared to the coupled mode theory, super mode theory views the coupled waveguides as a whole system and studies the normalized local modes of the system, which are called super modes. The taper coupler is a varying structure where the width of one of the waveguides is constantly changing along the propagation direction. In our simulation methods, the coupler can be divided into a succession of infinitely short sections. The length of each section is so small that the width can be regarded as invariant.

The simulation of a taper coupler can be divided into two steps: modeling of the individual divisions and a cascade of individual models. For each division, as the width is assumed constant, it actually can be regarded as a simple directional coupler. In each division, there are fundamental super mode and first order super mode, which are named as even mode (E_e) and odd mode (E_o) respectively according to the symmetry of their field distributions. The total field of the super mode system is a linear combination of the even and odd mode.

The even and odd modes are called phase matched if the propagation constants of these two modes in individual waveguides are the same. Otherwise, they are phase mismatched. When the phase mismatch is large, two waveguides are decoupled in which case a wave propagating in either one is not affected by the existence of the other and the super modes of the composite structure just become those of the individual waveguides. δ is defined as the difference of the propagation constants of two individual waveguide modes while β_c is for two super modes in a similar way:

$$\delta = \frac{\beta_2 - \beta_1}{2} \text{ and } \beta_c = \frac{\beta_e - \beta_o}{2} \tag{3.1}$$

If δ is much smaller than 0, most energy of the even mode is located in waveguide 1 while if it is much larger than 0, most energy is located in waveguide 2, as shown in Fig. 3.4. The case is opposite for the odd mode. So the taper coupler is to spatially transfer the energy of a super mode from one waveguide to the other by designing the tapered waveguide so that δ sweeps from a negative value to a positive

value. We can obtain the expressions of super modes and the relationship between the phase mismatch of super modes (β_c) and that of the individual modes (δ):

$$\beta_c^{\,2} = \delta^2 + \kappa^2 \tag{3.2}$$

As δ and β_c are known, the coupling strength κ can be thus calculated. The mode field distribution of even and odd super modes, as well as those of the individual modes is shown in Fig. 3.5.

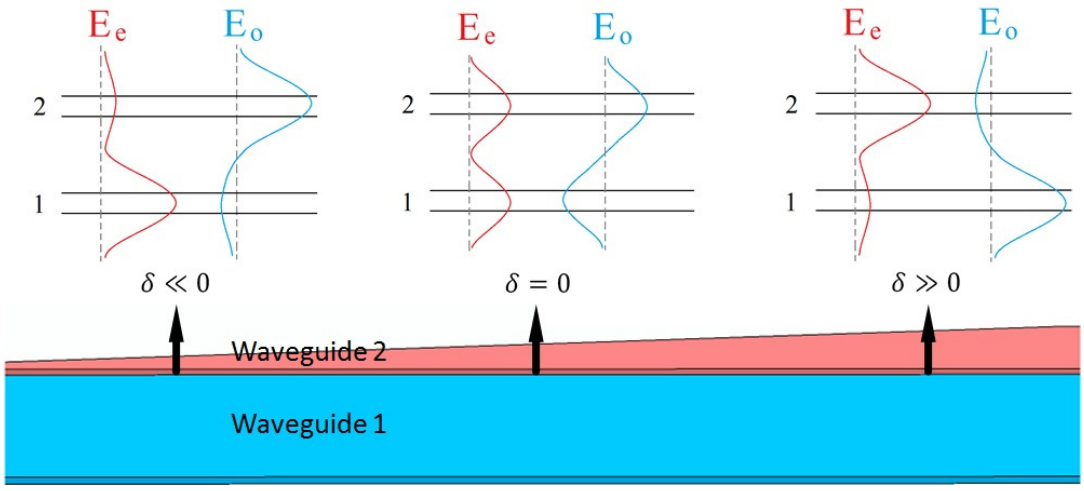

Fig. 3.4 The super modes of a taper coupler waveguide

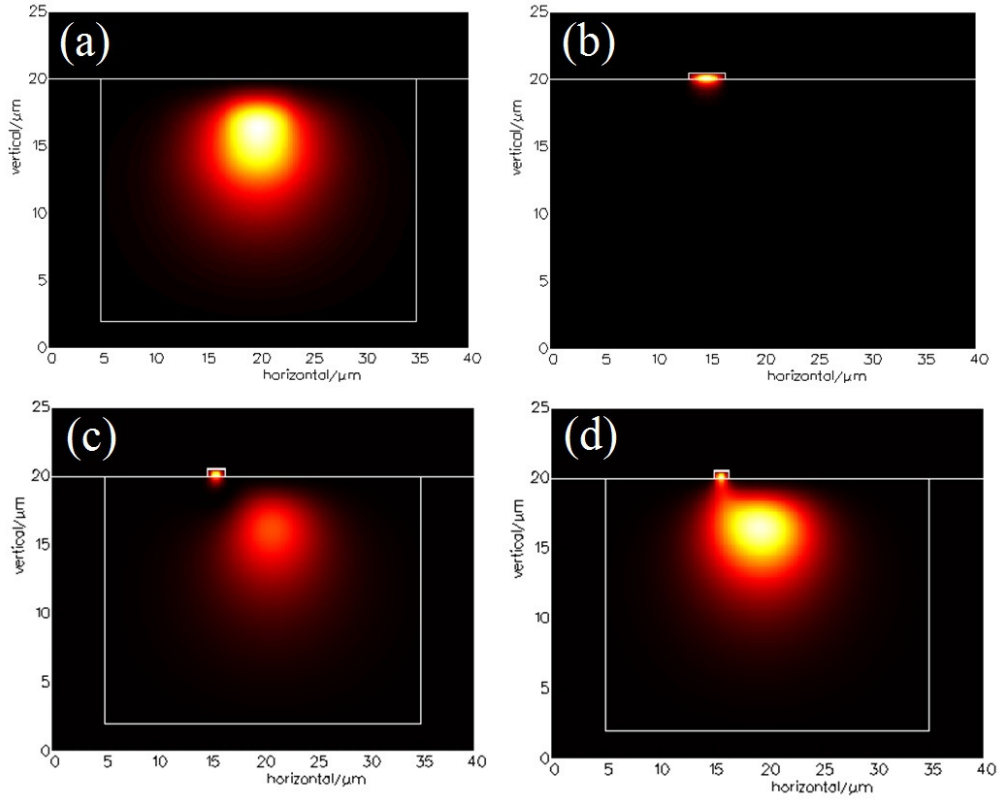

Fig. 3.5 The fundamental mode of the Ti:$LiNbO_3$ waveguide (a) the As_2S_3 waveguide (b) and the odd (c) the even mode (d) of the coupled waveguides

Transfer matrix formalism is derived to cascade all the models based on coupled mode equations. In the matrix form, the solution to coupled mode equation is:

$$\begin{bmatrix} E_1(z) \\ E_2(z) \end{bmatrix} = \begin{bmatrix} \left[\cos(\beta_c z) + \frac{j\delta}{\beta_c}\sin(\beta_c z)\right]e^{-i\delta z} & -\frac{j\kappa}{\beta_c}\sin(\beta_c z)e^{-i\delta z} \\ -\frac{j\kappa}{\beta_c}\sin(\beta_c z)e^{i\delta z} & \left[\cos(\beta_c z) - \frac{j\delta}{\beta_c}\sin(\beta_c z)\right]e^{i\delta z} \end{bmatrix} \begin{bmatrix} E_1(0) \\ E_2(0) \end{bmatrix} \tag{3.3}$$

where $E_1(0)$ and $E_2(0)$ are the input electric fields in waveguide 1 and 2. Let $z = z_0$ and re-form the equation to obtain the expression of vector, let $z = z_0 + \Delta z$ and substitute the vector expression into it. We could arrive at the transfer matrix formalism relating the model at $z_0 + \Delta z$ to the model at z_0 :

$$\begin{bmatrix} E_1(z_0+\Delta z) \\ E_2(z_0+\Delta z) \end{bmatrix} = M(z_0+\Delta z; z_0) \begin{bmatrix} E_1(z_0) \\ E_2(z_0) \end{bmatrix}$$

$$M(z_0+\Delta z; z_0) = \begin{bmatrix} \left[\cos(\beta_c \Delta z) + \frac{j\delta}{\beta_c}\sin(\beta_c \Delta z)\right] e^{-i(\delta \Delta z)} & -\frac{j\kappa}{\beta_c}\sin(\beta_c \Delta z) e^{-i[\delta(z_0+\Delta z)+\delta z_0]} \\ -\frac{j\kappa}{\beta_c}\sin(\beta_c \Delta z) e^{i[\delta(z_0+\Delta z)+\delta z_0]} & \left[\cos(\beta_c \Delta z) - \frac{j\delta}{\beta_c}\sin(\beta_c \Delta z)\right] e^{i(\delta \Delta z)} \end{bmatrix} \quad (3.4)$$

Then by multiplying the matrices in order, the models are cascaded. Consequently, the electric field at a certain point z can be obtained from the known input $E_1(0)$ and $E_2(0)$.

In our simulations, the software Fimmwave is used to model each section and calculate all the numerical parameters of the propagation constants: β_1 , β_2 , β_e and β_o . The matrices cascaded simulations were done with Matlab computing software.

3.3.2 Simulation results

The structure of the As_2S_3-Ti:$LiNbO_3$ taper coupler waveguide is illustrated in Fig. 3.3. A titanium diffused channel waveguide is formed in the lithium niobate substrate. On the substrate surface is the As_2S_3 ridge waveguide with the varying waveguide width, which is separated from the Ti:$LiNbO_3$ channel waveguide by 0.5~1 μm. As the width of the As_2S_3 taper varies, the mode propagation constants in each section are plotted against the average width of that section in Fig. 3.6.

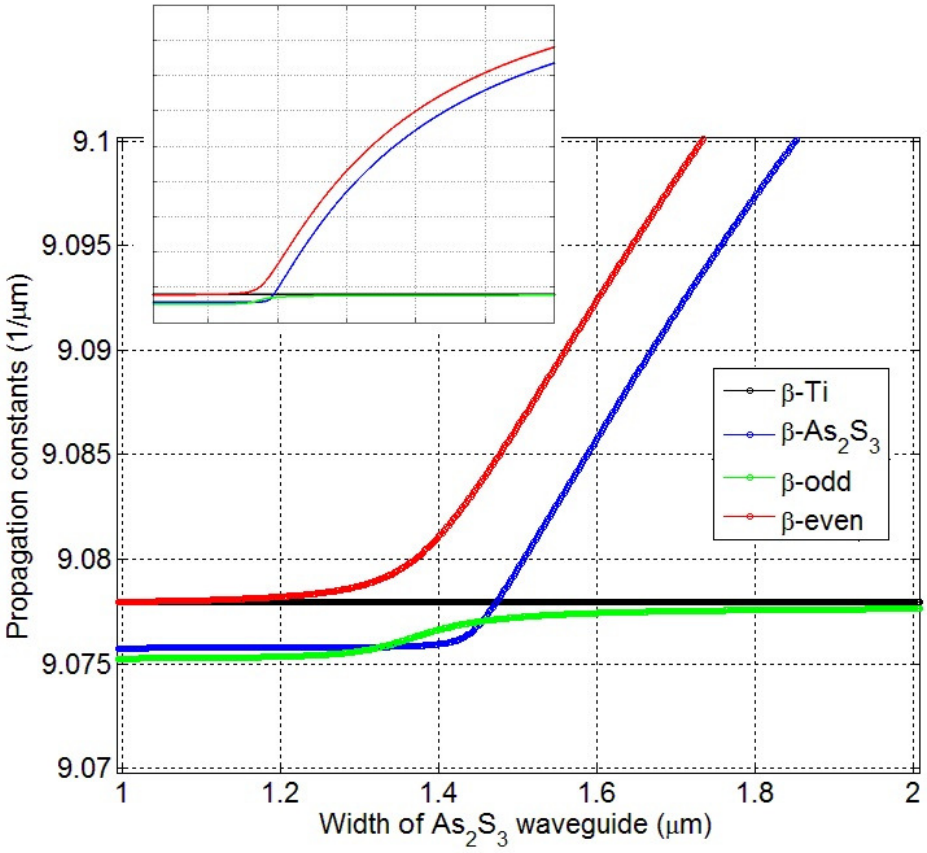

Fig. 3.6 The propagation constants of four modes with a inset picture showing them in a large scale

As we can see from the calculated propagation constants, the individual Ti:$LiNbO_3$ channel waveguide mode constant remains unchanged as its width is uniform, while the other three modes experience the increasing propagation constants with the varied wider As_2S_3 taper width. During this process, there is a point that the propagation constants of the As_2S_3 mode and the Ti mode are equal, corresponding to the point that the phase mismatch δ equals to 0. From the Fig. 3.6, it is the point where the β-As_2S_3 and β-Ti curves cross, corresponding to the width of 1.47 μm (for the TM

mode waveguide), which is called critical width. At the critical width point, two waveguides are phase matched and the energy is equally distributed in two waveguides for both even and odd modes.

At the initial design, a linear taper coupler was used. The As_2S_3 taper waveguide width is linearly increased from 1~3.5 μm. The squares stand for the coupling efficiency and the bars represent the magnitude of oscillation, as shown in Fig. 3.7. From the figure, we can see that there is an optimum point that the maximum coupling reaches about 95% when the taper length is 5 mm. The inset picture shows the coupling efficiency of a linearly 5 mm long taper waveguide. It is clear that if the taper length is longer than this optimum length, the coupled energy oscillates and couples back from the even mode to the odd mode.

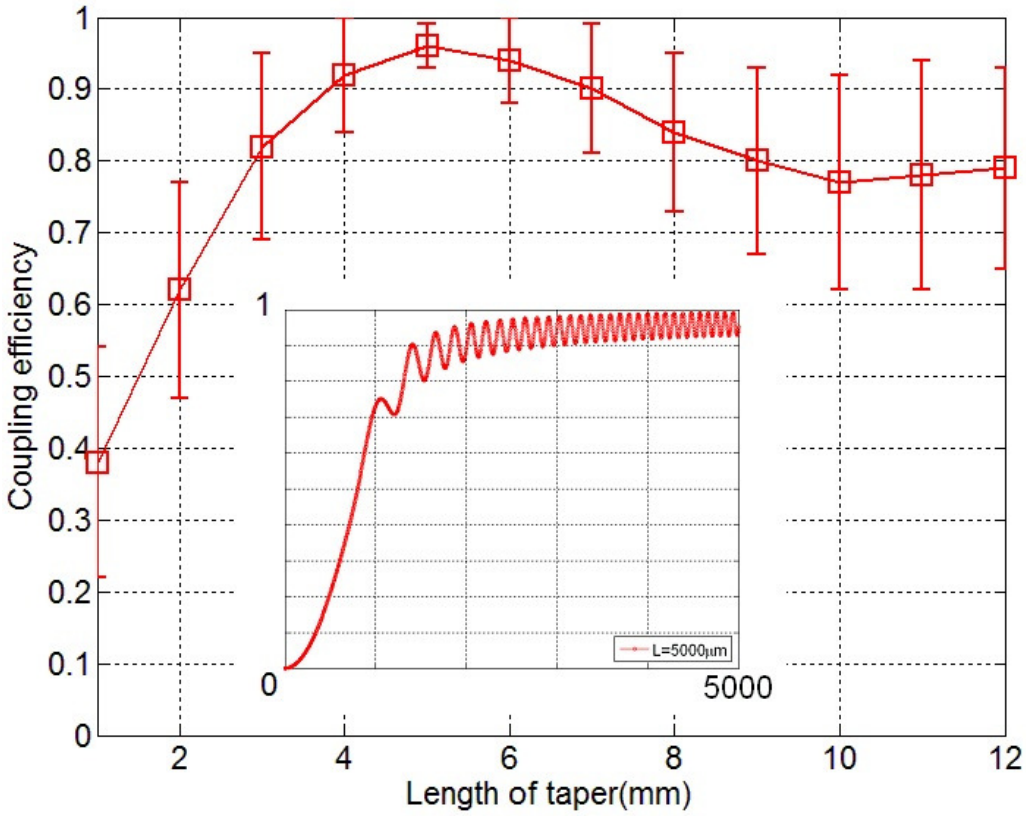

Fig. 3.7 Coupling efficiency for tapers of different length, with the inset figure showing the coupling process of a 5 mm long taper

At the end of the taper width, there is still a weak coupling between two waveguides, which negatively affects the coupling efficiency and causes it to oscillate. This behavior of coupler is like that of the resonant couplers. As a result, a certain amount of energy flows back and forth between the two waveguides. Under the super mode theory view, the energy couples between the even and odd modes. Therefore, in the presence of mode beating, it is not necessarily that the longer taper, the better coupling at the taper end. It is assumed that there exists an optimum taper length at a

certain taper width that most coupling occurs while beyond that taper width, the taper length should be shortened to avoid the mode beating between two waveguides.

Therefore, we arrived at the two stage taper coupler design, as shown in Fig. 3.3. Since the end width of the first stage which is called transition width can now be a much smaller value, the rate of width change is reduced largely. The simulation shows that for the first part of a two stage taper, if the width varies from 1.0 μm to 1.6 μm in the length of 2 mm, along with the second stage width varying from 1.6 μm to 3.5 μm in the length of 1 mm, the coupling efficiency can reach above 90% and almost suffers no mode beating.

3.4 As_2S_3-on-$LiNbO_3$ race track ring resonator waveguide design

As introduced in Chapter I, resonator based reconfigurable optical devices with feedback paths are attracting interest in recent years as compact on-chip active optic device components with various functions, such as modulators, tunable optical filters and multiplexers. The resonant cavity optical waveguide can be realized by various structures, such as ring resonator [11], micro disk [10], micro sphere [15] and grating Fabry-Perot cavity resonator. A resonant cavity optical waveguide consists of a feedback path and a coupler structure that only a partial of the incident light would be coupled into the cavity and the remained part would be transmitted to the output port. At a certain wavelength, if the phase of the light propagating inside the cavity is the integral times of 2π, the light would be totally trapped inside the cavity. And this wavelength would be the resonant wavelength of an optical cavity waveguide. For the integrated planar

resonant cavity optical waveguide, ring resonator waveguide is one of the most commonly used structures.

A ring resonator waveguide is consisted of a straight bus waveguide, a ring bend waveguide and a directional coupler that connecting the bus and feedback path ring waveguide. The incident light is input through the bus waveguide and partially coupled into the feedback ring waveguide. The coupled light inside the cavity propagates along a round-trip path and partially coupled back to the bus waveguide.

In this section, the design details of the As_2S_3-on-$LiNbO_3$ ring resonator waveguide would be discussed. And they can be divided into the coupling region design and the bend waveguide loss simulations.

An overview schematic design of the As_2S_3 ring resonator waveguide side-coupled to a Ti:$LiNbO_3$ channel waveguide is shown in Fig. 3.8.

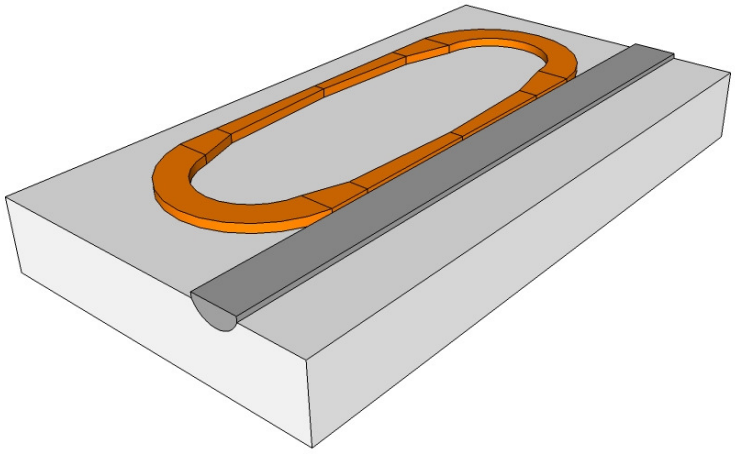

Fig. 3.8 Schematic design of As_2S_3-on-$LiNbO_3$ ring resonator waveguide

The straight bus waveguide is formed by the titanium diffused $LiNbO_3$ channel waveguide. The laser source would couple the light from the single mode fiber into the channel waveguide first. The output signal after the ring resonator would also be collected at the other end of the channel waveguide through the single mode fiber to the optical vector analyzer.

On the $LiNbO_3$ substrate surface, a race track ring shape As_2S_3 ridge waveguide is side coupled to the bus channel waveguide. In the coupling region, the As_2S_3-on-$LiNbO_3$ back to back taper waveguide is designed to efficiently couple the light from the bus waveguide into the ring waveguide, as well as couple the light back to the bus waveguide after the round-trip propagation inside the ring waveguide.

3.4.1 Coupling region design

In 2009, the first vertically integrated As_2S_3-on-$LiNbO_3$ ring resonator waveguide was demonstrated with the TM mode [11]. However, the performance of the ring resonator response is not premium and needs to be improved in the following aspects: a). propagation loss; b). coupling strength between bus waveguide and ring resonator; c). ring resonator response at telecommunication wavelength (1550 nm). d). extinction ratio of the ring response. A low-propagation-loss ring resonator waveguide is necessary for both linear electro-optical and nonlinear tuning proposes. In [4], the round-trip loss of the ring resonator with a circumference of 4.827 mm was 2.08 dB, which corresponds for a relatively high propagation loss of 4.3 dB/cm. Meanwhile, the

coupling strength between Ti:$LiNbO_3$ bus and As_2S_3 ring waveguides was only 10%, as well as a small extinction ratio of only 5 dB, which is not favorable for a resonance-notch filter device. Finally, the ring response was only able to be measured at 1522 nm, which is far away to the ideal telecom-band wavelength centered at 1555 nm. The first designed As_2S_3-on-$LiNbO_3$ ring resonator is shown in Fig. 3.9.

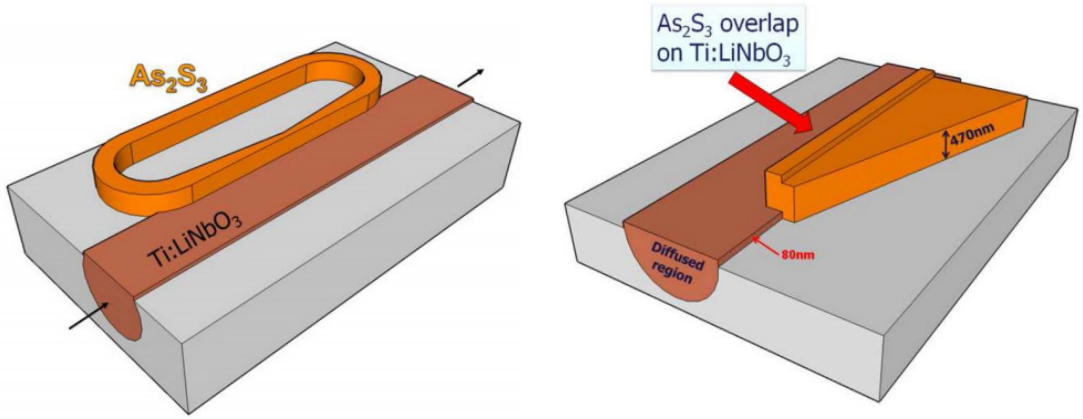

(a) (b)

Fig. 3.9 Vertically integrated As_2S_3-on-$LiNbO_3$ ring resonator (As_2S_3 waveguide overlapped on the Ti:$LiNbO_3$ channel waveguide)

Comparing the ring device in Fig. 3.9 to the re-designed ring waveguide shown in Fig. 3.8, we can see that the most significant change is inside the coupling region. In Fig. 3.9, the As_2S_3 taper coupler waveguide is a linear taper design which in previous section, it is noticed that the linear stage taper would suffer a resonant coupling beating and cannot reach the maximum coupling strength. As the same time, the other big change is in the old design, the As_2S_3 taper waveguide overlaps the Ti:$LiNbO_3$ channel

waveguide while in the new design in Fig. 3.8, the As_2S_3 taper coupler waveguide is about 0.5 μm away from the Ti:$LiNbO_3$ channel waveguide.

If observed under the surface profiler or SEM inspector, we could find that the Ti:$LiNbO_3$ channel waveguide has a 100 nm thick bump after diffusion process. Generally, the bump surface is also rough. It is believed that there would be a huge scattering loss if the optical light propagates through the bump surface.

Instead, a new designed two-stage back to back taper side-coupled to the Ti:$LiNbO_3$ channel waveguide was proposed to solve these problems. The comparison between the overlapped taper structure and the side-coupled taper waveguide is shown in Fig. 3.10.

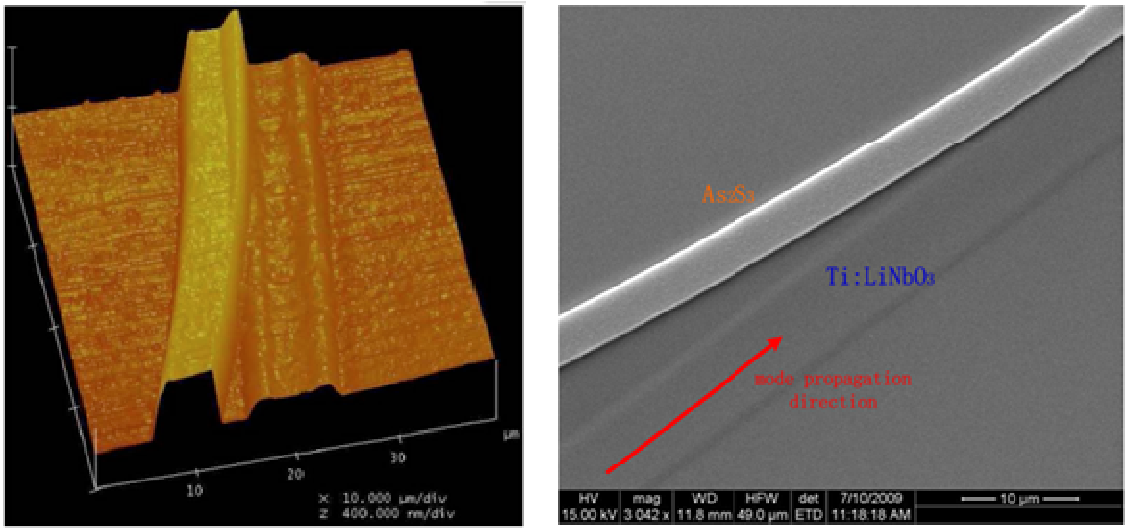

(a) (b)

Fig. 3.10 (a) AFM picture of the ring starting to overlap on Ti:$LiNbO_3$ waveguide (b) SEM image of the fabricated ring device: side-coupling region

The schematic design of the two-stage back to back taper structure is shown in Fig. 3.11.

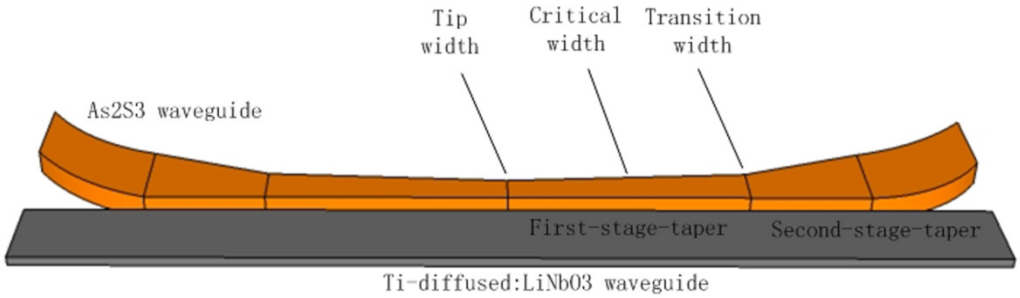

Fig. 3.11 Back to back two-stage taper side coupling of the As_2S_3 ring resonator

For the first stage of the two-stage taper, the width is designed to vary from 1.0 µm to 1.6 µm across 2 mm of length. It is followed with a much shorter 1 mm long second stage, with width varying from 1.6 µm to 3.5 µm, as shown in Fig. 3.11. Since the coupling region works as a two-by-two mode coupler, the Ti-diffused waveguide is increased to a 12 µm width in the coupling region to support two modes and minimize the mode radiation loss.

3.4.2 Back-to-back taper coupler simulation

The schematic structure of a back-to-back taper coupler waveguide of the ring resonator is shown in Fig. 3.12. It is composed of three parts: the down side taper waveguide, the uniform middle part waveguide and the up side taper waveguide. The one-side taper coupler design and simulation are discussed in the previous section. Here,

the method of super mode theory is also used to simulate the back-to-back taper coupler performance.

Fig. 3.12 As_2S_3-on-$LiNbO_3$ back-to-back taper coupler of the ring resonator waveguide

The purple color input mode indicates the fundamental super mode field E_e and the green color input mode means the first order super mode field E_o. In the coupled waveguide system, E_e also stands for the As_2S_3 waveguide mode while E_o stands for the Ti:$LiNbO_3$ channel waveguide mode. A transfer coupling matrix method is used to study the whole back-to-back taper coupling efficiency.

The three parts of the back-to-back taper were simulated separately and each part was described by a transfer coupling matrix. It starts from the down taper, as shown in Fig. 3.13.

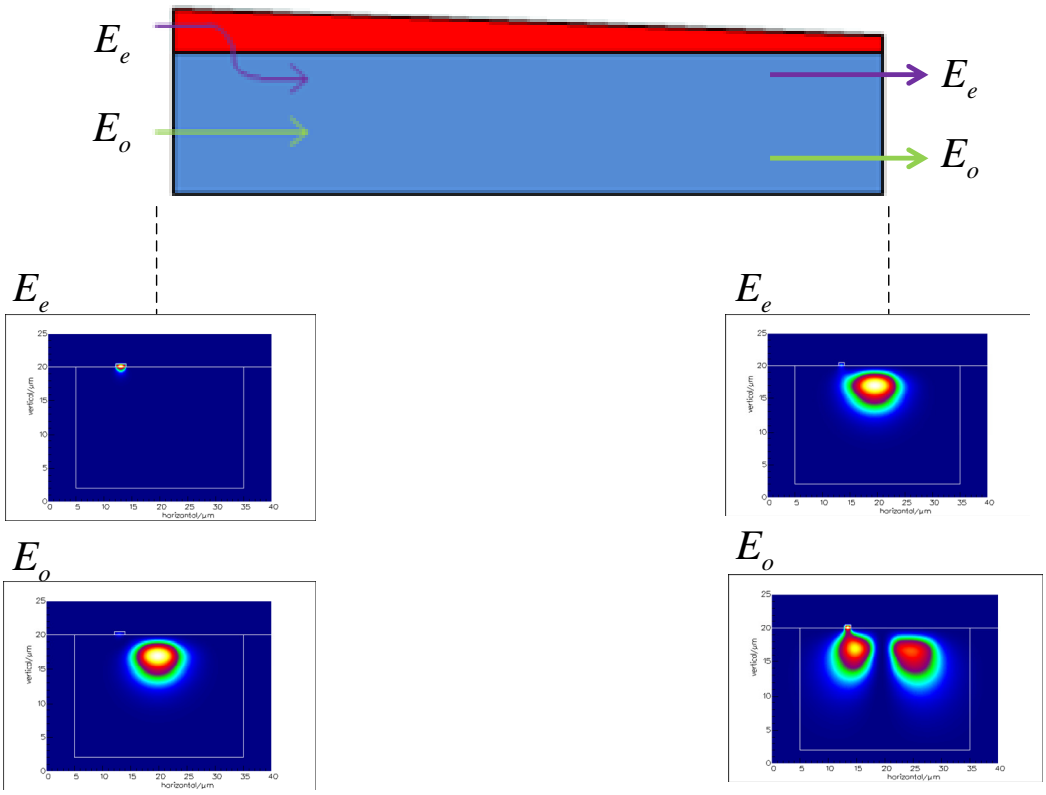

Fig. 3.13 Down-side taper simulation of the back-to-back taper coupler

Because the coupling region of the ring resonator is working as a two by two mode coupler, to avoid the mode energy loss, the central part of the Ti:$LiNbO_3$ waveguide is widened from 7 μm to 12 μm. A transfer matrix is written to model the coupling and transmittance of the down side taper coupler:

$$\begin{bmatrix} H_{11} & H_{12} \\ H_{21} & H_{22} \end{bmatrix} \tag{3.5}$$

where H_{11} stands for the fundamental As_2S_3 mode coupling to the fundamental Ti:$LiNbO_3$ mode at the middle section, H_{12} stands for the fundamental As_2S_3 mode

coupling to the first order Ti:$LiNbO_3$ mode at the middle section, H_{21} stands for the fundamental Ti:$LiNbO_3$ mode coupling to the fundamental Ti:$LiNbO_3$ mode at the middle section and H_{22} stands for the fundamental Ti:$LiNbO_3$ mode coupling to the first order Ti:$LiNbO_3$ mode at the middle section.

The middle part of the back-to-back taper is a simple uniform coupled waveguide, as shown in Fig. 3.14.

Fig. 3.14 Middle section part of the back-to-back taper coupler

Because the middle part coupled waveguide is uniform, there would be no mode energy coupling during the propagation of this part and only the phase varies. The transfer matrix of this middle part section is as follows:

$$\begin{bmatrix} e^{-j\beta_1 L} & 0 \\ 0 & e^{-j\beta_2 L} \end{bmatrix} \tag{3.6}$$

where β_1 is the propagation constant of fundamental Ti:$LiNbO_3$ mode and β_2 is the propagation constant of the first order Ti:$LiNbO_3$ mode. L is the length of this middle part uniform section waveguide.

The third part is the up side taper coupler which is symmetric to the down side taper coupler, as shown in Fig. 3.15.

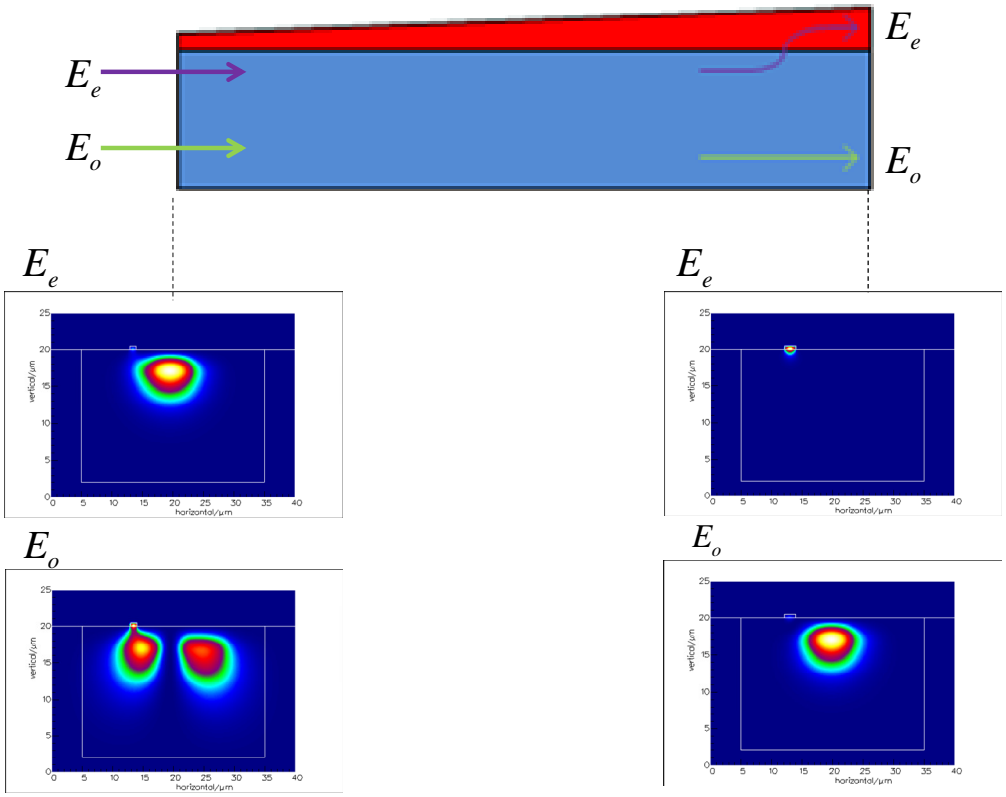

Fig. 3.15 Up-side taper simulation of the back-to-back taper coupler

Similarly, a transfer matrix is used to model the coupling for the up side taper as followed:

$$\begin{bmatrix} H'_{11} & H'_{12} \\ H'_{21} & H'_{22} \end{bmatrix} \tag{3.7}$$

where $H_{11}^{,}$ stands for the fundamental Ti:$LiNbO_3$ mode at the middle section coupling to the fundamental As_2S_3 mode, $H_{12}^{,}$ stands for the fundamental Ti:$LiNbO_3$ mode at the middle section coupling to the fundamental Ti:$LiNbO_3$ mode, $H_{21}^{,}$ stands for the first order Ti:$LiNbO_3$ mode at the middle section coupling to the fundamental As_2S_3 mode and $H_{22}^{,}$ stands for the first order Ti:$LiNbO_3$ mode at the middle section coupling to the fundamental Ti:$LiNbO_3$ mode.

The multiplication of the three transfer matrix would yield a two by two transfer matrix which evaluates the coupling performance of the back-to-back taper coupler for the ring resonator. The final transfer matrix is written as:

$$M = \begin{bmatrix} H_{11} & H_{12} \\ H_{21} & H_{22} \end{bmatrix} \cdot \begin{bmatrix} e^{-j\beta_1 L} & 0 \\ 0 & e^{-j\beta_2 L} \end{bmatrix} \cdot \begin{bmatrix} H_{11}^{,} & H_{12}^{,} \\ H_{21}^{,} & H_{22}^{,} \end{bmatrix} \tag{3.8}$$

where M_{11} stands for the fundamental As_2S_3 mode at the input transmitted to the fundamental As_2S_3 mode at the output, M_{12} stands for the fundamental As_2S_3 mode at the input coupled to the fundamental Ti:$LiNbO_3$ waveguide mode at the output, M_{21} stands for the fundamental Ti:$LiNbO_3$ waveguide mode at the input coupled to the fundamental As_2S_3 mode at the output and M_{22} stands for the fundamental Ti:$LiNbO_3$ waveguide mode at the input transmitted to the fundamental Ti:$LiNbO_3$ waveguide mode at the output.

For the TM mode ring resonator waveguide, the As_2S_3 single taper length is assumed as 3 mm. The thickness of the As_2S_3 waveguide is 0.47 µm and at the center part of the coupling region, the Ti:$LiNbO_3$ waveguide is widened to 12 µm.

The impact of the length of the middle uniform coupled waveguide on coupling efficiency was studied and simulated, as shown in Fig. 3.16.

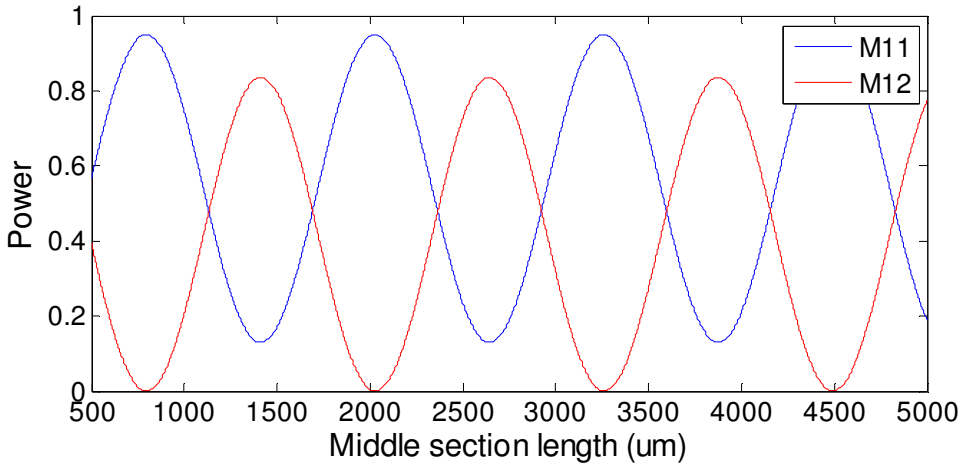

Fig. 3.16 The power of transmittance and coupling of the back to back taper with the varied middle uniform waveguide length

From Fig. 3.16, we can see that with the varied intermediate uniform waveguide length from 500~5000 µm, the coupling strength shows a big oscillation. And this indicates that the middle section part just works like a directional mode coupler.

The wavelength dependency of the coupling strength for the back-to-back taper is also simulated. Using the model of the As_2S_3 taper width from 1.1~1.9 µm with 3 mm length side coupled to the 12-µm wide Ti:$LiNbO_3$ waveguide, as well as a intermediate

uniform waveguide length at 1.5 mm, the coupling strength was plotted over a scanned wavelength from 1520~1580 nm, as shown in Fig. 3.17.

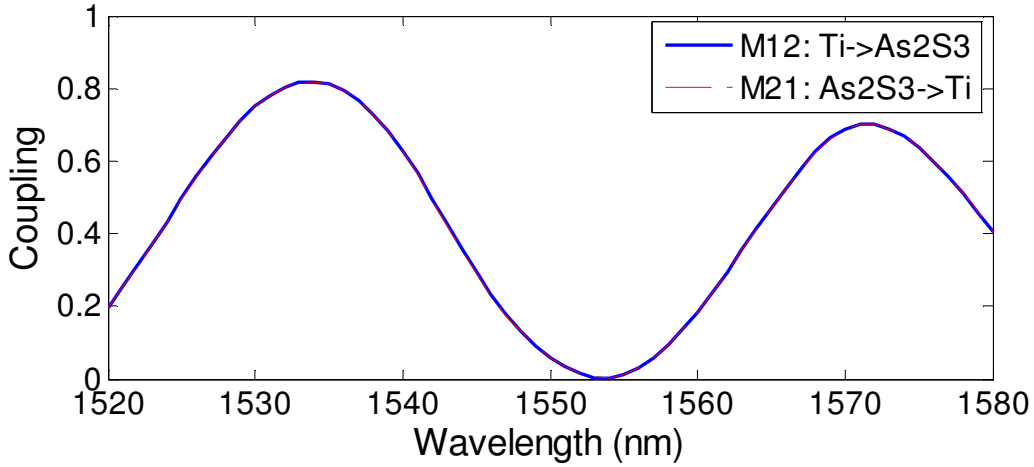

Fig. 3.17 Wavelength dependent coupling strength of the back-to-back taper coupler

Finally, a ring resonator response was generated by using the wavelength dependent coupling from the back-to-back taper coupler model. If the ring resonator has a propagation loss of 2 dB/cm and a round-trip length of 1.85 cm, using the coupling strength from the transfer matrix component M_{21}, the resonant response is simulated in Fig. 3.18.

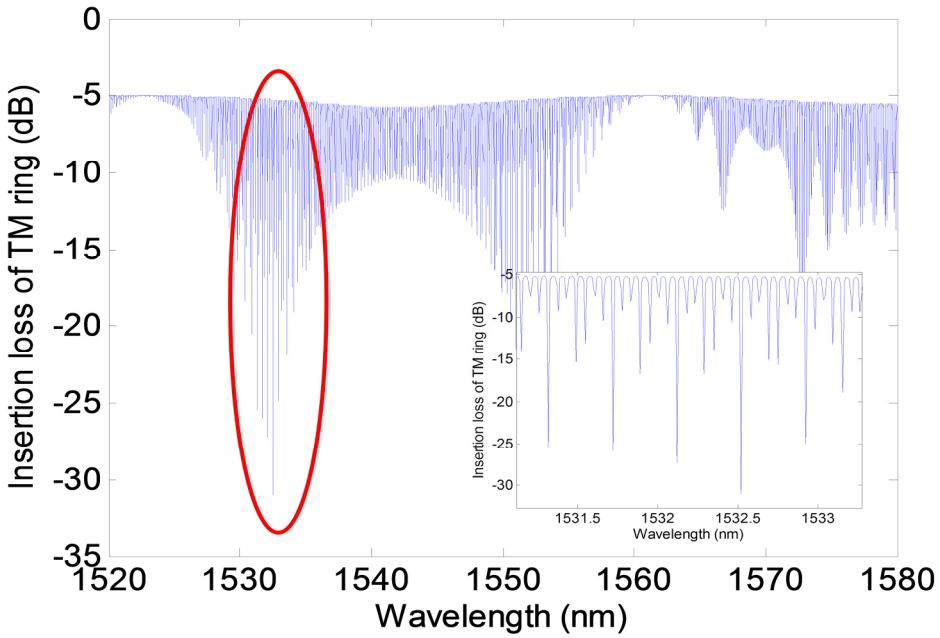

Fig. 3.18 Simulated ring resonator response with the coupling strength from the back-to-back taper coupler transfer matrix model

3.4.3 Bend waveguide simulations

The other critical design parameter for the ring resonator waveguide device is the bend radius of the ring waveguide part. In any bent waveguide, the bending loss increases as the radius decreases. There are two types of bent mode waveguides based on the As_2S_3-on-$LiNbO_3$ substrate which are TE and TM bent waveguide. The design of TM bent waveguide mode is much simpler than that of TE one due to the birefringence property of the $LiNbO_3$ material substrate.

The $LiNbO_3$ substrate used in our As_2S_3-on-$LiNbO_3$ material platform is X-cut Y-propagation. The $LiNbO_3$ crystal shows different refractive index at three different

propagation directions: X-direction and Y-direction are n_o with the refractive index of 2.2112383 and Z-direction is n_e with the refractive index of 2.138092, which is shown in Fig. 3.19.

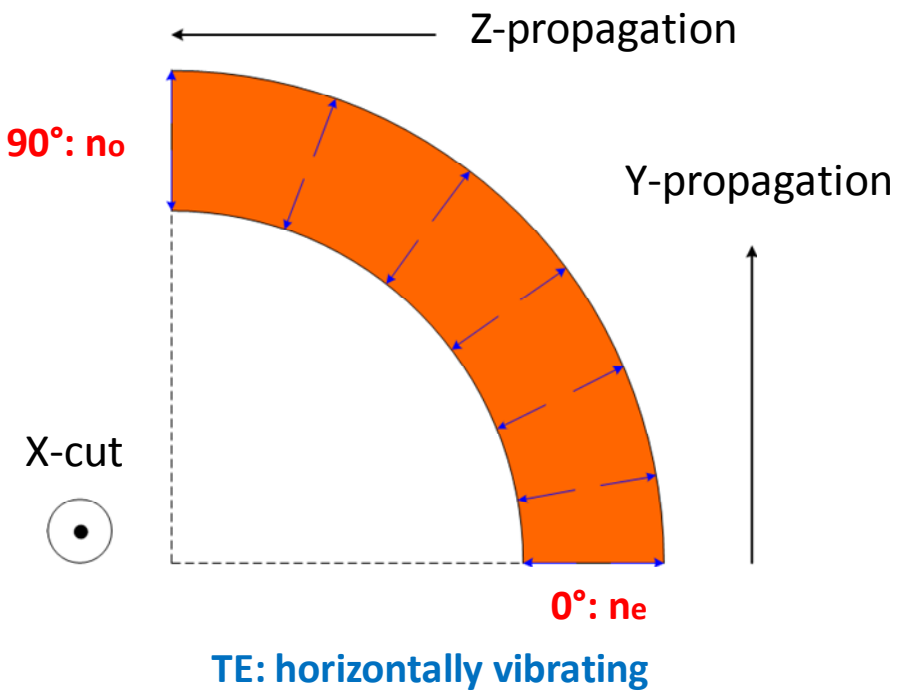

Fig. 3.19 Bent waveguide on X-cut Y-propagation $LiNbO_3$ substrate

For the TM bent mode, as its electrical field vibrates vertically to the substrate on X-direction, the $LiNbO_3$ substrate shows a constant n_o refractive index anywhere at the bent waveguide.

The bending loss for the fundamental TM mode of the As_2S_3-on-$LiNbO_3$ waveguide with varied bent radius was simulated, as shown in the Table 3.1. The

simulated TM waveguide was designed with the parameters: width 3.5 µm, As_2S_3 thickness 0.47 µm and air upper cladding.

Bent radius (µm)	Bending loss (1/cm)	Bending loss (dB/cm)
400	0.000978	0.00424
350	0.00636	0.0276
300	0.0409	0.1775
250	0.258	1.12
200	1.562	6.78

Table 3.1 Bending loss versus bent radius of the fundamental TM mode

From the Table 3.1, we can see that with the decreased bent radius from 400 µm to 200 µm, the waveguide bending loss increases dramatically about 1600 times. The bent waveguide mode fields of 400 µm radius and 200 µm radius were shown in Fig. 3.20.

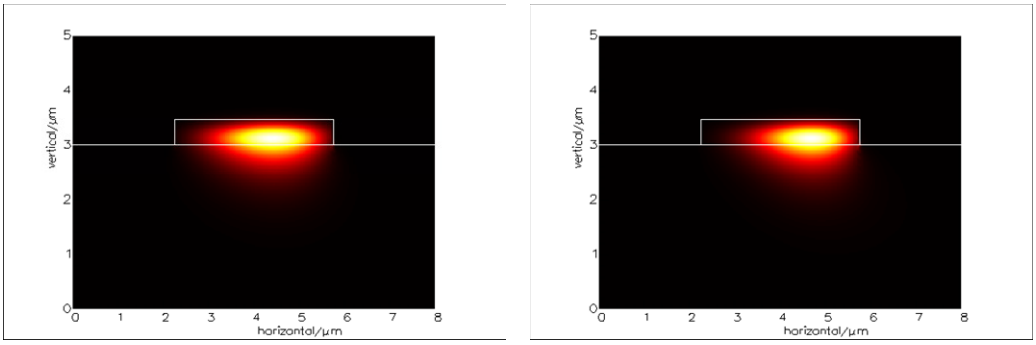

(a) (b)

Fig. 3.20 Comparison of the bent waveguide mode fields of (a) 400 μm radius and (b) 200 μm radius

To minimize the bending loss of the bent waveguide of the ring resonator, for the TM mode design, the bent radius is chosen as 400 μm. At this bent radius, the bending loss of the bent waveguide is as low as that could be neglected.

The bending loss of the TE bent waveguide on X-cut Y-propagation was also simulated. As mentioned above, the TE mode electric field vibrates horizontally to the $LiNbO_3$ substrate. As the $LiNbO_3$ substrate shows a birefringence property of its refractive index, the TE bent mode would see a changing substrate index during its propagation along the bent waveguide from 0° to 90°, as shown in Fig. 3.19.

The changing $LiNbO_3$ substrate index of the TE bent mode from 0° to 90° is shown in Fig. 3.21.

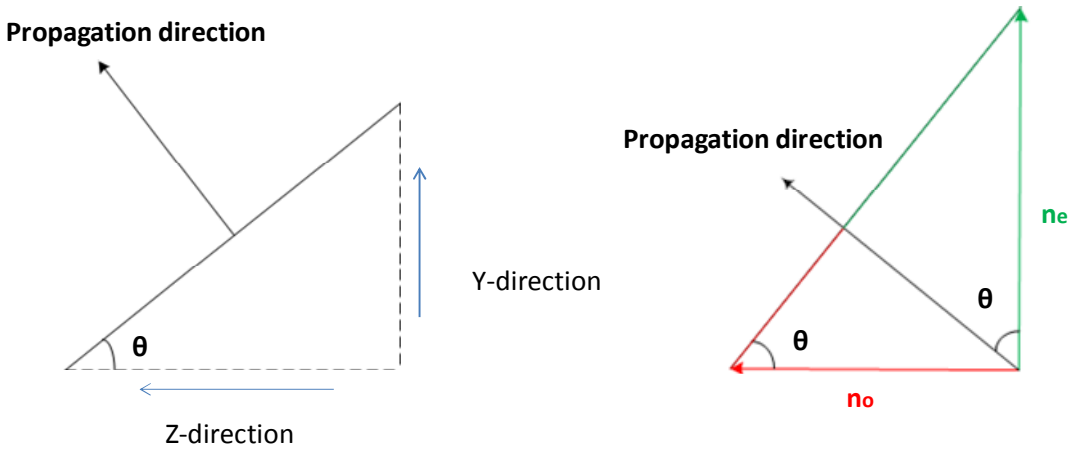

Fig. 3.21 The substrate refractive index of a TE mode on X-cut Y-propagation from 0° to 90° on its propagation direction

The substrate refractive index of a TE mode on the bent waveguide propagation direction from 0° to 90° can be calculated by the equations:

$$n_{xx} = \sqrt{(n_e \cos\theta)^2 + (n_o \sin\theta)^2} \quad \text{and} \quad n_{zz} = \sqrt{(n_e \sin\theta)^2 + (n_o \cos\theta)^2} \tag{3.9}$$

where $n_e = 2.138092$ and $n_o = 2.2112383$.

The simulated TE mode As_2S_3-on-$LiNbO_3$ waveguide has the As_2S_3 thickness of 0.31 µm, the width of 5 µm and with the SiO_2 upper cladding layer of 100 nm. The bending loss and the mode confinement factor of the bent waveguide at the varied propagation bent angle are shown in Table 3.2.

Bend degree	Mode confinement	Bend loss (dB/cm)
0	51.39%	0.0022
10	51.22%	0.0025
20	49.93%	0.01
30	47.73%	0.0955
40	44.78%	1.1057
50	41.13%	9.4924
60	37.25%	45.4059
70	33.63%	120.9076
80	31.10%	202.6852
90	30.32%	233.8676

Table 3.2 TE mode bent waveguide: bending loss and mode confinement factor at the different bent degree

At the 90° propagation direction of the bent waveguide, it shows the largest bending loss. The comparison of a straight waveguide TE mode and a 400 μm bent radius waveguide TE mode at the 90° is shown in Fig. 3.22. From Fig. 3.22, we can see that the bent mode electric field is seriously distorted and squeezed to the edge of the waveguide, indicating a relatively large bending loss.

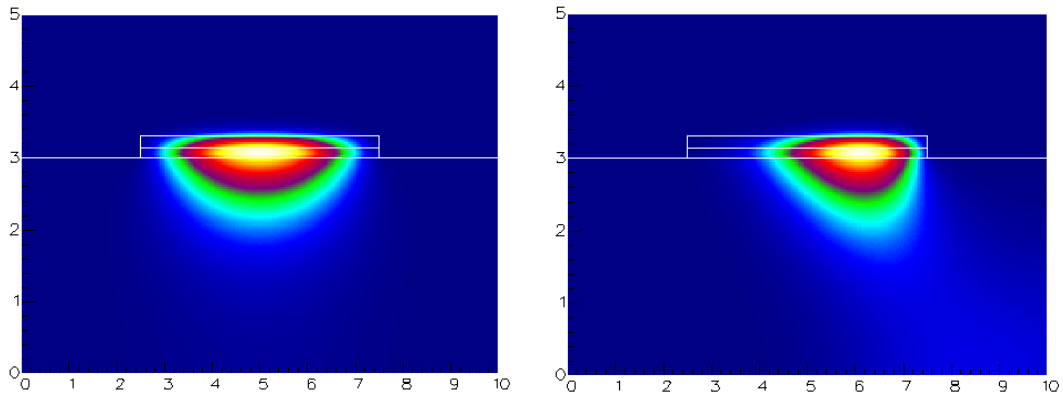

Fig. 3.22 The TE waveguide mode electric field distribution at 90° (a) straight waveguide mode (b) 400 µm bent radius waveguide mode

For a 400 µm bent radius, the TE As_2S_3-on-$LiNbO_3$ ring waveguide shows a total round-trip bending loss as high as 13.6 dB, after calculation. This large bending loss is unacceptable for a low-loss integrated waveguide device. Compared to the low negligible bending loss of the TM mode, for the ring resonator waveguide device, TE mode bent waveguide is not preferred.

3.5 Side-wall grating coupler cavity waveguide

The As_2S_3-on-$LiNbO_3$ ring resonator waveguide is designed for TM mode because the TE bent waveguide mode suffers a huge bending loss at 400 µm radius due to the changing substrate index of the $LiNbO_3$.

However, compared to the TM mode, TE mode has a much bigger mode confinement factor and a much smaller effective mode area, which is a desirable feature for nonlinear applications. Therefore, to realize a low loss TE mode As_2S_3-on-$LiNbO_3$ resonator cavity waveguide, the side-wall grating coupler cavity waveguide was designed.

Sidewall grating waveguides have the advantages of strong coupling strength, compact device size and simple lithography process. Compared to a ring resonator structure which consists of a straight bus waveguide connected to a ring waveguide by a coupling region, the sidewall grating cavity waveguide is simply made by two identical sidewall grating couplers connected by a straight uniform waveguide, which need no concerns about the bending loss from the ring structure.

The integrated optical cavity waveguide is consisted of two identical sidewall grating couplers with a straight long uniform waveguide in the middle, as seen in Fig 3.23. A two stage taper design is employed to efficiently couple the optical mode from the Ti diffused channel waveguide into the As_2S_3 waveguide.

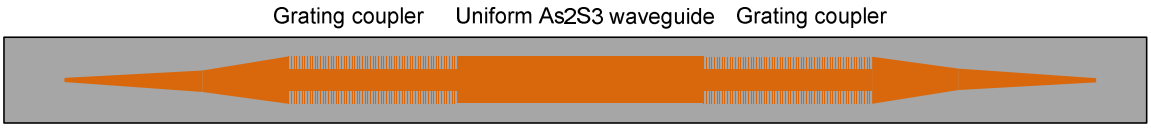

Fig. 3.23 Schematic structure of an optical cavity waveguide based on sidewall grating couplers

The cross-section view of the sidewall grating coupler is illustrated in Fig. 3.24 (a). The fundamental TE optical mode intensity distribution of the hybrid As_2S_3-on-$LiNbO_3$ waveguide for the grating coupler is shown in Fig. 3.24 (b). To evaluate the coupling and reflection performance of the sidewall grating inside the cavity structure, a testing structure of a single sidewall grating coupler is designed, as shown is Fig. 3.24 (c).

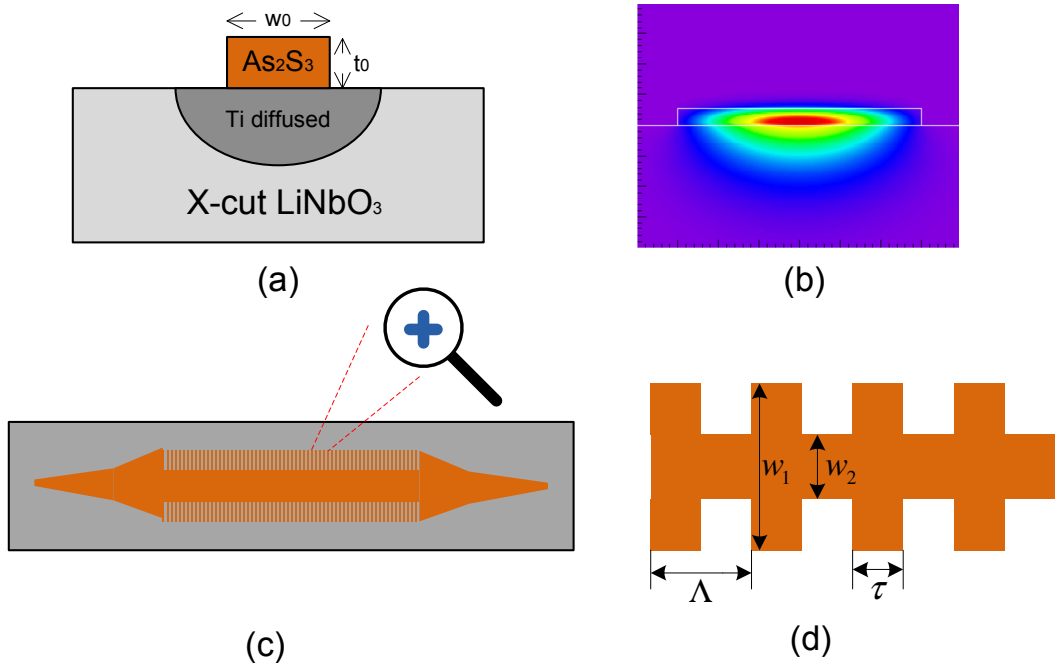

Fig. 3.24 (a) Cross section view of the hybrid As_2S_3-on-$LiNbO_3$ waveguide; (b) Mode intensity distribution of the hybrid waveguide; (c) Test structure of a single sidewall grating coupler; (d) Zoom-in view of the sidewall grating structure

The sidewall gratings are patterned on both side of the As_2S_3 strip waveguide. The widest width of the waveguide is defined as w_1 while the narrowest part is defined as w_2. The grating depth is calculated by $\Delta w = (w_2 - w_1)/2$. The grating period Λ is given by $\Lambda = \lambda_B / (2n_{eff})$ in which λ_B is the center wavelength of the grating reflection wavelength and n_{eff} is the effective mode index of the hybrid waveguide. The duty cycle is defined as τ / Λ. The largest grating coupling strength is achieved when the duty cycle is 0.5. The total grating length L_g is defined as the number of period N multiplying the period Λ. For an average grating width $w_0 = (w_1 + w_2)/2$ as 3.2 μm, the effective index is estimated around 2.153523 and the period Λ is calculated about 0.36 μm. For a grating depth of 800 nm and number of periods of 500, the grating coupling strength is 8.75 mm^{-1}. The As_2S_3 waveguide thickness is selected as 0.3 μm to meet the designed effective grating waveguide mode index.

The center uniform waveguide length is set as 1 mm, returning a cavity round-trip length as 2 mm.

The reflection R and transmission T of the sidewall grating coupler are given by equation (3.10) and (3.11):

$$R = \frac{|k|^2 \sinh^2 sL_g}{s^2 \cosh^2 sL_g + (\Delta\beta/2)^2 \sinh^2 sL_g} \tag{3.10}$$

$$T^2 + R^2 = 1 \tag{3.11}$$

where $s = \sqrt{k^2 - (\Delta\beta/2)^2}$ and $\Delta\beta = 2\pi(2n_{eff}/\lambda - 1/\Lambda)$. The largest reflection occurs at the wavelength that make the $\Delta\beta$ equals to zero and $R_{\max} = \tanh^2 sL_g$. The simulated

reflection and transmission response of the designed grating coupler is shown in Fig. 3.25 (a).

At the same time, the sidewall grating cavity response is calculated based on a transfer matrix method. The transfer matrix method divides the grating cavity waveguide into three parts which are two identical grating couplers and the center uniform cavity length. Each part is represented by a transfer matrix function and the resonator response is the multiplication of the three matrixes by equation (3.12).

$$\begin{bmatrix} a_1' \\ a_2' \end{bmatrix} = \begin{bmatrix} t+\frac{r^2}{t} & j\frac{r}{t} \\ -j\frac{r}{t} & \frac{1}{t} \end{bmatrix} \begin{bmatrix} \alpha e^{-j\beta L_c} & 0 \\ 0 & \frac{1}{\alpha} e^{j\beta L_c} \end{bmatrix} \begin{bmatrix} t+\frac{r^2}{t} & j\frac{r}{t} \\ -j\frac{r}{t} & \frac{1}{t} \end{bmatrix} \begin{bmatrix} a_1 \\ a_2 \end{bmatrix} \tag{3.12}$$

$$\begin{bmatrix} a_1' \\ a_2' \end{bmatrix} = \begin{bmatrix} M_{11} & M_{12} \\ M_{21} & M_{22} \end{bmatrix} \begin{bmatrix} a_1 \\ a_2 \end{bmatrix} \quad \text{T=} \frac{a_1'}{a_1} = M_{11} - \frac{M_{12} \cdot M_{21}}{M_{22}} \quad \text{and} \quad \text{R=} \frac{a_2}{a_1} = -\frac{M_{21}}{M_{22}}$$

The grating cavity resonator response is plotted in Fig. 3.25 (b).

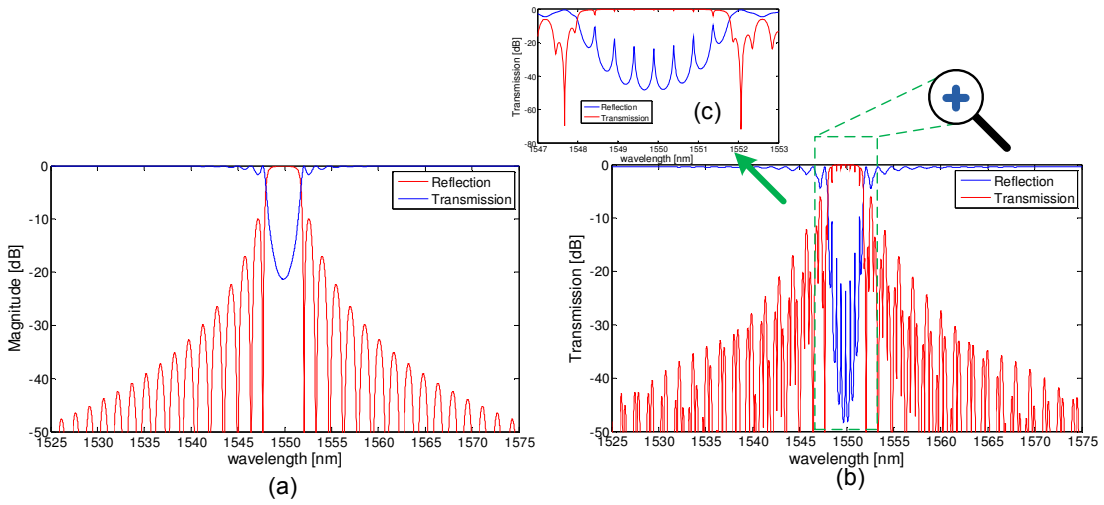

Fig. 3.25 (a) Reflection and transmission of the sidewall grating coupler; (b) Sidewall grating cavity resonator response; (c) A zoom-in plot of the resonant response at 1547~1553 nm wavelength range

3.6 Nonlinear calculations of the resonator cavity waveguide

As_2S_3 glass shows a good potential as a Kerr medium for ultra-fast all-optical tuning capability because of its high nonlinearity coefficient at infrared wavelength range. At the same time, resonance cavity devices are favored for their easily tunable ability as a small change of refractive index in the material would lead to a shift for their resonance. Therefore, the nonlinear Kerr process in As_2S_3 material can be applied to our As_2S_3-on-$LiNbO_3$ resonators and used as ultra-fast all-optical tunable on-chip devices. In the previous sections, the TM mode As_2S_3-on-$LiNbO_3$ ring resonator waveguides and the TE mode side-wall grating coupler cavity waveguides are designed and simulated. In

this section, the nonlinear applications based on these two devices are calculated and discussed.

3.6.1 Ring resonator waveguide

Waveguide nonlinearity efficiency γ was calculated for our TM-mode As_2S_3-on-$LiNbO_3$ ring waveguide with equation $\gamma = \frac{n_2 \omega_0}{cA_{eff}}$. Here, n_2 is material nonlinearity coefficient for which As_2S_3 is 3.8×10^{-18} m^2/W. And A_{eff} is the effective mode area of the waveguide. For our 0.47-μm thick and 3.5-μm wide As_2S_3 waveguide, the mode area of the fundamental TM-mode is 4 μm^2 at 1.55-μm wavelength. With the assumed parameters, the calculated γ is around 3.85 radian/m·W.

If the nonlinear process operated with a resonant cavity, the resonant response could save substantially power required to achieve same nonlinear phase shift compared to non-resonant devices (such as straight waveguide). The resonant cavity-enhanced nonlinearity tuning based on our As_2S_3-on-$LiNbO_3$ ring waveguide is shown in Fig. 3.26.

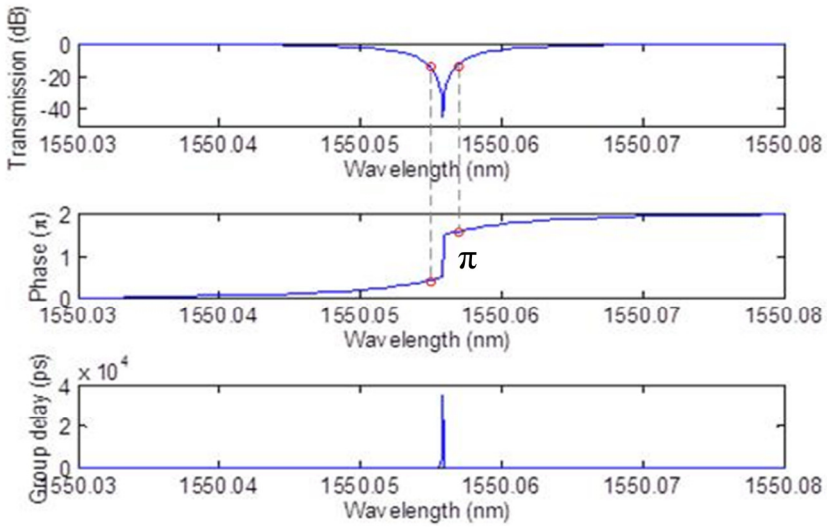

Fig. 3.26 A π nonlinear phase shift can be achieved with a resonant cavity-enhanced nonlinear process in TM-mode As_2S_3-on-$LiNbO_3$ ring waveguide

If the propagation loss of the ring waveguide is assumed as 2 dB/cm and the round-trip length of the resonator is 1.7 cm, using the calculated waveguide nonlinearity coefficient γ, not considering any extra loss and assuming an ultra-high Q resonator, the required power to make a π phase shift is only about 40 mW, under the help of steep abrupt phase change around the resonant wavelength.

3.6.2 Side-wall grating coupler cavity

As same as the ring resonator waveguide, the waveguide nonlinearity efficiency γ was calculated for our TE-mode As_2S_3-on-$LiNbO_3$ waveguide with relation $\gamma = n_2\omega_0 / cA_{eff}$. For our 0.3-μm thick and 3.2-μm wide As_2S_3 waveguide, the mode area of the fundamental TE-mode is 2.86 μm^2 at 1.55-μm wavelength. With the assumed

parameters, the calculated γ is around 5.38 radian/m·W. Compared to the TM-mode As_2S_3-on-$LiNbO_3$ waveguide, the nonlinearity efficiency γ of the TE-mode waveguide is about 40% larger due to the much smaller mode area.

The electrical field inside a grating cavity waveguide would be strongly enhanced at the resonant wavelength. The total electrical field is the sum of two standing waves which are the forward signal wave (E_f) and the backward signal wave (E_b) by equation:

$$E = E_f + E_b \tag{3.13}$$

$$E_f = \frac{t_1}{1 - r_1 r_2 e^{2\alpha L_c} e^{-j(2\beta L_c + \varphi_1 + \varphi_2)}} E_i \text{ and } E_b = \frac{t_1 r_2 e^{\alpha L_c} e^{-j(\beta L_c + \varphi_2)}}{1 - r_1 r_2 e^{2\alpha L_c} e^{-j(2\beta L_c + \varphi_1 + \varphi_2)}} E_i \tag{3.14}$$

where the terms r_1 and r_2 are defined as the reflectance of the grating couplers and if the grating couplers are identical, r_1 equals to r_2. L_c, φ_1 and φ_2 are defined as the cavity length and phase shifts at the grating couplers. The term α is the propagation loss inside the cavity in the unit of dB/cm. The electrical field enhancement inside the cavity is given by $Enhancement = |E|^2 / |E_{in}|^2$. In our case, the cavity length is 0.1 cm long and the propagation loss is 2.5 dB/cm. The reflectance of the sidewall grating coupler is assumed 0.8. The electrical field enhancement inside the resonant cavity is plotted in Fig. 3.27.

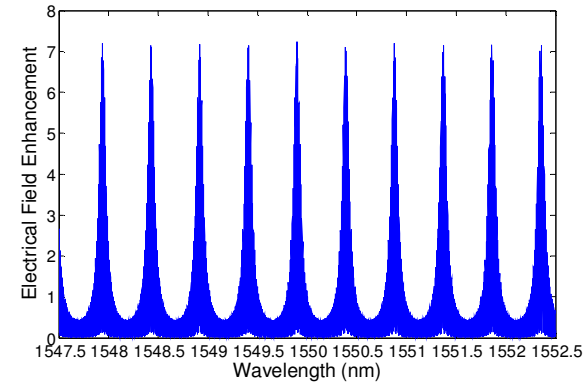

(a)

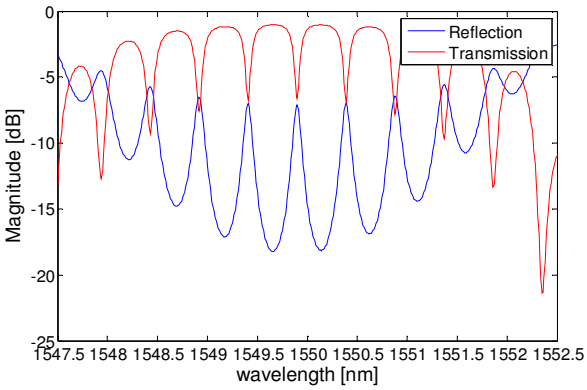

(b)

Fig. 3.27 (a) Electrical field enhancement inside the grating cavity waveguide (b) Sidewall grating cavity resonant response at the wavelength from 1547.5~1552.5 nm

From Fig. 3.27, we can see the largest enhancement occurs at the resonant wavelength of the grating cavity and the electrical field can be enhanced as large as 7 times of the input signal.

The nonlinear phase shift due to the pump power inside the cavity can be express as $\phi_{NL} = \gamma P_0 L_{eff}$. P_o is the peak power inside the cavity and L_{eff} is the effective propagation length as the waveguide has a propagation loss. L_{eff} can be written as

$L_{eff} = [1 - \exp(-\alpha L)] / \alpha$. If the propagation loss is chosen as 2.5 dB/cm and cavity round-trip length is 2 mm, the effective nonlinear length is 1.89 mm. Considering the nonlinear efficiency γ is 5.38 radian/m·W and the cavity resonant enhancement is 7, to achieve a π phase shift at the resonant wavelength would require a peak power of 44 W.

However, it is not required to tune such a big phase shift on a resonant cavity to change its resonant wavelength. A nonlinear phase shift of π/10, which only need 4.4 W peak power, is sufficient enough to tune the resonant response.

CHAPTER IV

WAVEGUIDE FABRICATION AND PROCESS OPTIMIZATION[*]

To effectively transfer the design of the integrated optical waveguides to the real working devices, the fabrication process is not only the most critical, but also the most challenging task. The fabrication process can be generally divided into three parts: thin film material deposition, lithography patterning and etching process.

Although there are many ways to deposit thin film, develop the pattern from the lithography process and define the waveguide through the etching process, according to the material platform chosen, the device structure feature size and the material tolerance property, only very specific and optimized fabrication methods can be suitable to realizing the designed the integrated As_2S_3-on-$LiNbO_3$ waveguide devices.

This chapter would discuss the fabrication and process optimization in detail for the general As_2S_3-on-$LiNbO_3$ waveguides, the ring resonator waveguides and the side-wall grating coupler cavity waveguides.

---

[*] Part of this chapter is reprinted by the permission from "Two-stage taper enhanced ultra-high Q As_2S_3 ring resonator on $LiNbO_3$" by Yifeng Zhou, Xin Xia, William T. Snider, Jaehyun Kim, Qi Chen, Wee C. Tan and Christi Madsen, IEEE Photonics Technology Letters, Vol. 23, No. 17, copyright 2011 by IEEE.

[*] Part of this chapter is reprinted by the permission from "Fabrication and measurement of sidewall gratings integrated in hybrid As_2S_3-Ti:$LiNbO_3$ optical waveguides" by Xin Wang, Yifeng Zhou and Christi Madsen, Journal of Lightwave Technology, Vol. 21, Issue 17, copyright 2014 by IEEE.

4.1 The As_2S_3-on-$LiNbO_3$ waveguides fabrication

The general procedures for fabricating the Ti:$LiNbO_3$ diffused channel waveguides and As_2S_3-on-$LiNbO_3$ waveguides are shown in Fig. 4.1. The general process of the fabrication starts by dicing the $LiNbO_3$ wafer into square pieces. After cleaning the wafer surface after dicing, a thin layer of Ti metal is deposited by DC sputtering. Followed lithography and ICP etching would define the straight waveguide pattern. After removing the photo-resist, the sample would be put in the diffusion furnace for forming the Ti:$LiNbO_3$ diffused channel waveguides.

The second stage is making the As_2S_3-on-$LiNbO_3$ waveguides. It starts by the As_2S_3 thin film deposition by RF sputtering. A protection layer of SiO_2 and Ti would also be deposited on top of the surface. After that, through the photo-lithography and ICP etching, the As_2S_3-on-$LiNbO_3$ waveguide patterns are made. The final stage is to remove the remained photo-resist and protection layer by HF dipping.

The details for this fabrication process are discussed in this chapter.

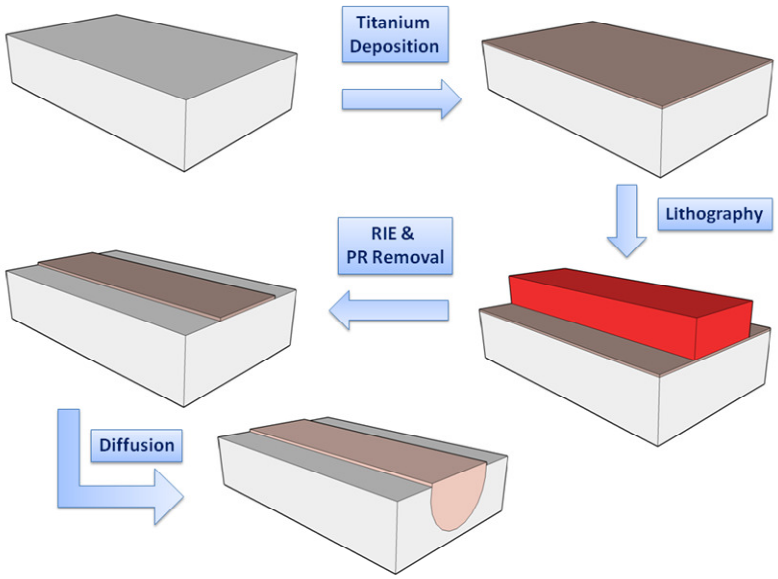

(a)

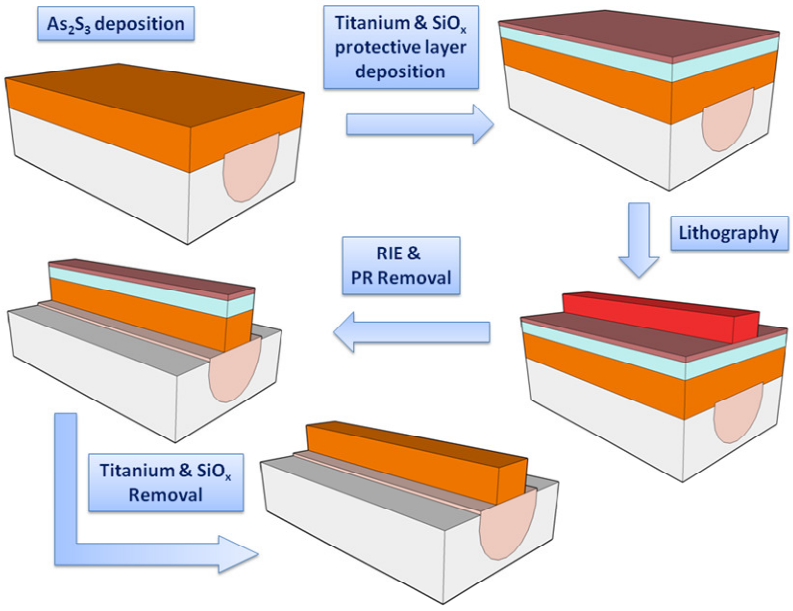

(b)

Fig. 4.1 Procedures for fabricating Ti:$LiNbO_3$ diffused channel waveguides and As_2S_3-on-$LiNbO_3$ waveguides

The fabrication of the titanium diffused $LiNbO_3$ channel waveguides starts from the substrate preparation by wafer dicing. The $LiNbO_3$ substrate is a 3-inch diameter X-cut Y-propagation wafer, bought from the company Crystal Technology Inc. For the $LiNbO_3$ wafer, one side of the wafer is polished and all the waveguide devices are built on top of the polished surface. The 3-inch wafer is diced into small square or rectangular shape pieces of samples by dicing saw machine.

During the dicing process, a lot of tiny $LiNbO_3$ dicing residuals could be attached to the sample surface. Therefore, a complete surface cleaning is necessary after dicing and before the next thin film deposition step. The cleaning starts from removing the small dicing residuals by using Q-tip gently rubbing over the surface of the sample with the soapy water. Then the sample is flushed under deionized (DI) water. Three common alcohol chemicals are then used to further clean the sample surface, which are acetone ((CH3)2CO), methanol (CH3OH) and Isopropyl (IPA) (C3H8O). Acetone is widely used in the laboratory for its good cleaning capability but easily leaving residuals after drying; methanol and IPA are also easy drying alcohols but they would not leave any residuals after cleaning. So the order of using these three alcohols is firstly using acetone, then methanol and finally IPA to clear everything.

A thin layer of titanium metal of 95 nm thickness is then deposited on top of the cleaned substrate by DC sputtering. Sputtering is the primary alternative to the evaporation method for metal deposition in microelectronics fabrication. Compared to the evaporation, sputtering has a better step coverage which induces far less radiation damage than electron beam evaporation. Also, it is much better at producing layers of

compound materials and alloys. These advantages have made sputtering the metal deposition technique of choice for most silicon-based technologies.

A multi-targets sputtering machine from AJA Company is used to deposit the thin film in our research group. The schematic figure of the sputtering machine is shown in Fig. 4.2.

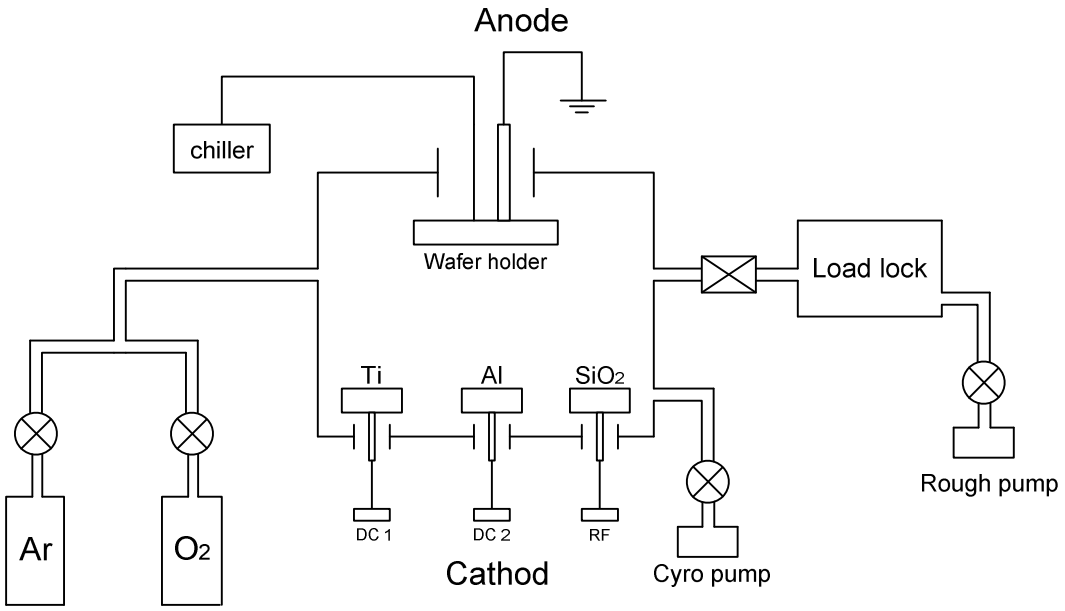

Fig. 4.2 Schematic figure of the AJA sputtering machine

The sputtering machine is mainly consisted of two chambers. The larger one is the main chamber which is always under the high vacuum maintained by the cryo pump. The smaller size one is called the load lock and is connected to the main chamber. The connection between the two chambers is switched on and off by a gate shutter. Every time the samples are load and unloaded, only the load lock is opened and after it is

pumped through the rough pump, the samples would be loaded into the main chamber. Because the load lock size is small, the time to pump it down to the high vacuum is short.

Inside the main chamber where the sputtering occurs, the samples are fixed on the wafer holder at the top which is connected to the anode. The material targets are sitting at the bottom of the chamber and are connected to the cathode. Depending on the material types, the targets are connected to DC and RF power supplies. For the Ti metal deposition, the DC power supply is used. The gases can be flowed into the chamber via a thin tube and controlled by a switch.

With the power turning on and Ar gas flowing into the chamber, the plasma would be ignited. High-energy ions would strikes the target containing the material to be deposited. To collect as many of the ejected atoms as possible, the cathode and anode in the sputtering system are closed spaced. The real sputtering machine system of our research lab is shown in Fig. 4.3.

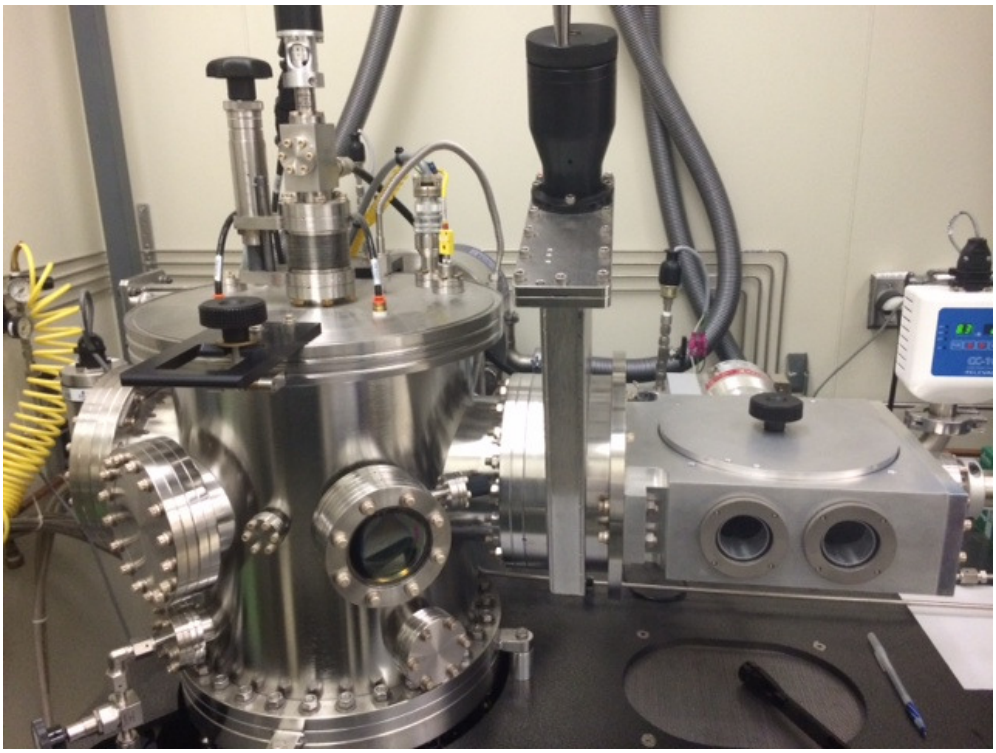

Fig. 4.3 The real AJA sputtering system: main chamber and load lock

The titanium thin film was deposited at the rate of 1.6 $\mathring{A}/s$ with 40 sccm Ar gas flow rate, 160 W DC power supply at 3 mtorr pressure.

Contact photo-lithography process is followed to pattern the straight photo resist waveguides on Ti metal. The waveguide pattern is designed and plotted by L-Edit software. A photo-mask is produced to contain the designed pattern by Benchmark Company. Each photo-mask contains the image of one layer of the lithography process. Depending on the contact lithography mask aligner, the photo-mask is the same size as the final image on the wafer.

Our Karl-Suss MA6 contact aligner is the simplest type of the aligners. Its structure can be shown in Fig. 4.4.

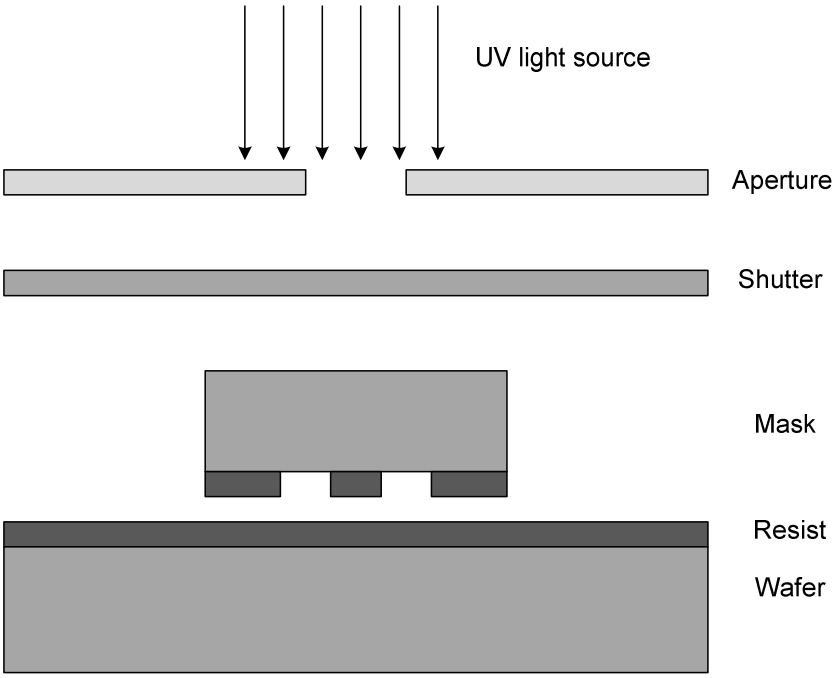

Fig. 4.4 Schematic of a contact lithography aligner

In contact printing, the mask is pressed against the resist-coated wafer during exposure. The mask is held chrome side down in a frame just below the microscope objectives. Vernier screws are then used to move the wafer with respect to the mask. Once the wafer is aligned to the mask the two are clamped together, the microscope objectives are retracted, and the wafer/mask assembly is wheeled into the exposure station. The UV light radiation from a high-intensity lamp is used to expose the wafer. After exposure, the carriage is returned to the inspection station for unloading.

Ideally, the entire wafer is in contact with the mask. Because of this contact the gap between the wafer and the optical disturbance goes to zero and diffraction effects are minimized. However, actually due to the finite resist thickness, the gap cannot be zero. Furthermore, in real contact printers, the mask contact varies across the wafer surface, as neither the wafer nor the mask is perfectly flat. One method to smoothen and flatten the wafer surface is to soft-back the photo-resist after spin coating. Also, pressures are used to push the mask into more intimate contact with the wafer, which is called the hard contact mode of exposure.

The major disadvantage of hard contact lithography is defect generation due to the contact between the resist-coated wafer and the photo-mask [16]. Defects are generated both on the wafer and on the mask on every contact cycle. That is why after a certain times of exposure process, the photo-mask needs to be replaced. Overall, the minimum feature size of the contact lithography in our research lab is about 1.5~2 μm.

The next step is to transfer the waveguide pattern from the developed photo-resist to the Ti metal. Etching step is necessary for that transfer process. There are mainly two types of etching methods: one is wet etching and the other is dry ion etching. The dry etching can be done by physical damage, chemical attack, or the combination of the two. The wet etching is a purely chemical process with low anisotropy but high selectivity.

The Ti metal film can be etched through wet etching process by using diluted HF solvent. However, it has serious drawbacks of the lack of anisotropy and very poor process control, which is shown in Fig. 4.5.

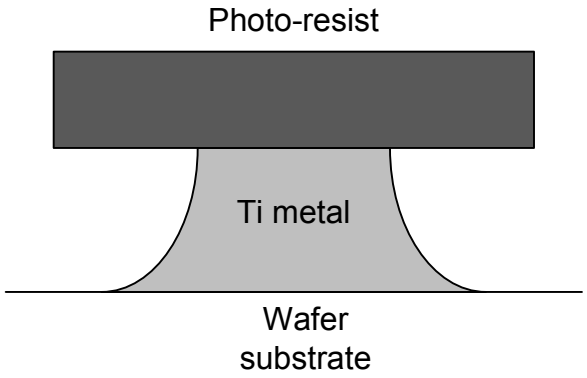

Fig. 4.5 Isotropic metal etching process

In our case, serious undercut phenomenon would occur in the wet etching process. The designed Ti waveguide width is 7 μm but in the wet etching, it can be reduced to less than 5 μm as the etching speed is hard to control.

Therefore, reactive ion etching (RIE) process is used to etch the thin film after the photo-lithography process. The RIE etching process is a low-pressure plasma etching. Etching in a plasma environment has several significant advantages when compared with wet etching. Plasmas are much easier to start and stop than simple immersion wet etching. Furthermore, the etching process can be highly anisotropic and even very small feature size patterns can be perfectly etched.

The etching gases include CHF_3 and Ar. CHF_3 appears as the chemical etchant while Ar gas is the inert gas for the purely physical ion milling. The combination of both chemical etching and physical ion milling can help to make a vertical anisotropic sidewall, as shown in Fig. 4.6.

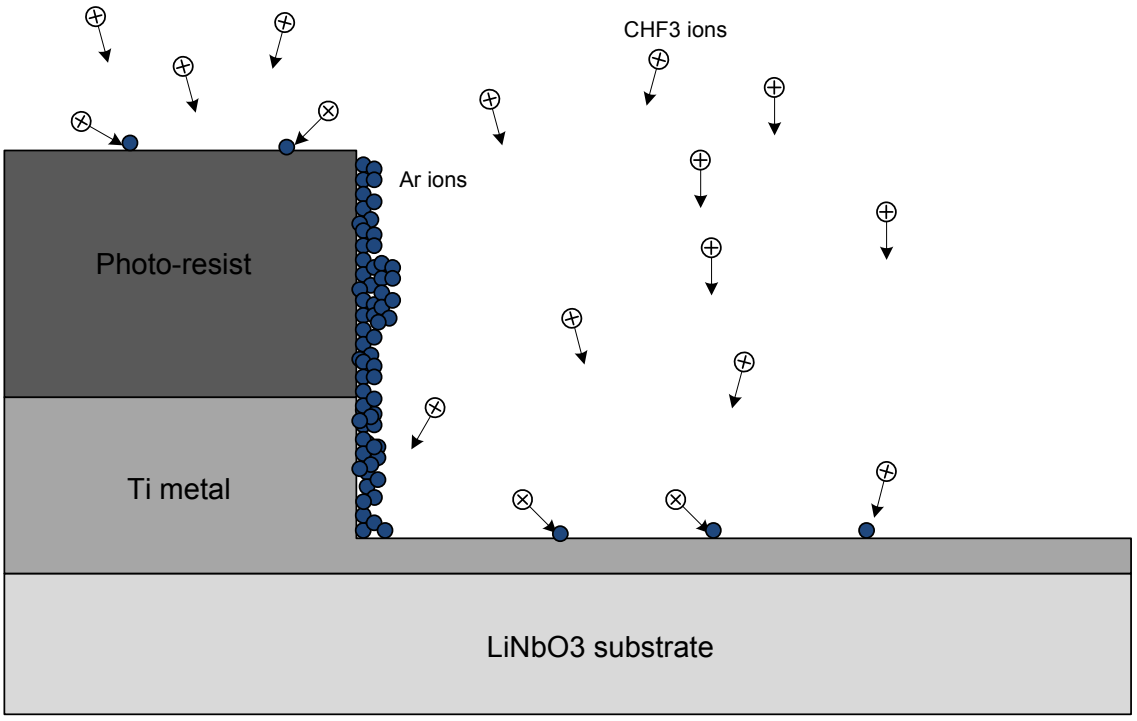

Fig. 4.6 Schematic diagram of an anisotropic plasma etching showing the formation of sidewall passivating films

After removing the photo-resist, the samples are going through the diffusion process to form the Ti:$LiNbO_3$ channel waveguides. The diffusion process occurs in wet breathing air ambient at 1025 ℃ for 9.5 hours. And the end facets of the $LiNbO_3$ samples are polished to minimize the butt coupling loss.

A 0.47-μm thick thin film of As_2S_3 is then deposited on top of the fabricated Ti-diffused:$LiNbO_3$ substrate by RF sputtering with the AJA sputtering system. A protective layer of SiO_2 and Ti is deposited over the As_2S_3 thin film to prevent it from reacting in $(CH_3)_4NOH$-based photo-resist developer. The As_2S_3 thin film deposition uniformity is also checked, as shown in Fig. 4.7.

The RF deposition recipe for As_2S_3 with AJA system is using a 25 sccm Ar gas and 35 W of RF power at vacuum pressure of 3 mtorr.

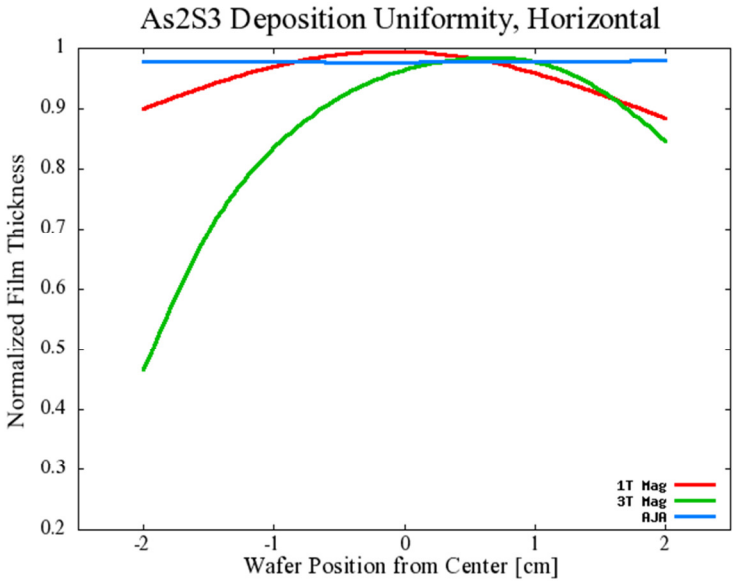

Fig. 4.7 As_2S_3 thin film deposition uniformity

After that, the second-layer photo-lithography is followed to pattern the As_2S_3 waveguide via the photo-resist. A 30-minutes hard bake is used to further harden the photo-resist, which would make them protect the As_2S_3 waveguide better during the RIE etching process. The smooth and vertical sidewall of the As_2S_3 waveguide after RIE etching can be seen in Fig. 4.8.

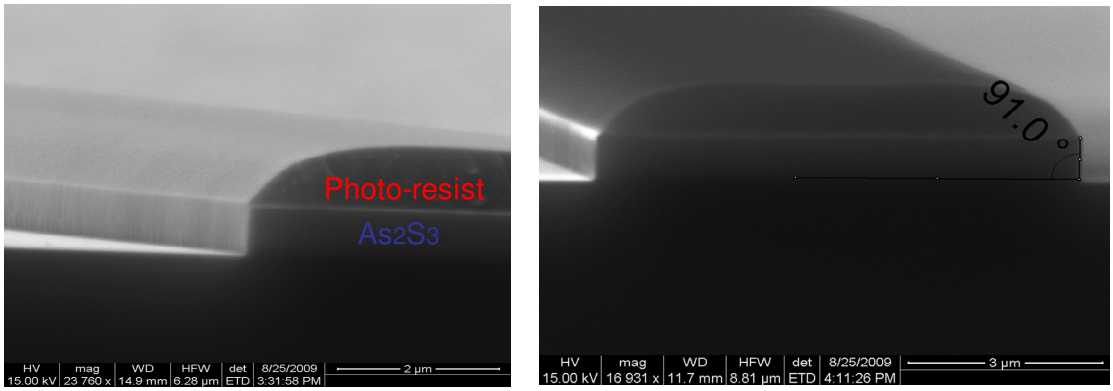

(a) (b)

Fig. 4.8 SEM picture of the As_2S_3 waveguide after RIE etching (a) smooth sidewall (b) vertical sidewall

The RIE etching recipe is optimized for etching the As_2S_3 waveguide. The ratio of the gas for CHF_3:Ar is fixed at 5:1. CHF_3 content is critical to prevent undercut due to polymer deposition on the sidewall. Previous experiments showed that a slower etch rate is favorable to make a smoother sidewall As_2S_3 etching. The etch rate can be controlled by adjusting the flow rate of the gases. At the same time, a relatively higher RF power is needed to make a larger DC bias on the plate, which induces a straighter path for ions and make an anisotropic etching profile.

Overall, the etching recipe for the As_2S_3 waveguide is the mixed gas of 25 sccm CHF_3 and 5 sccm Ar. The RF power is 100 W and the ICP power is 200W. The etching is under the pressure of 10 mtorr.

4.2 Fabrication of the ring resonator waveguide

As discussed in Chapter III, the biggest change of the As_2S_3 ring resonator waveguide design is that the ring waveguide would be side-coupled to the Ti:$LiNbO_3$ channel waveguide without any overlap. After the diffusion, the Ti:$LiNbO_3$ channel waveguide shows a 100-nm high bump on the substrate surface and the bump surface is also not smooth. Therefore, the overlap between the As_2S_3 ring waveguide and the Ti:$LiNbO_3$ channel waveguide would introduce the scattering loss which could not be negligible. The best solution is to put the As_2S_3 ring waveguide beside the Ti:$LiNbO_3$ bump at about 0~0.5 μm distance, as shown in Fig. 4.9.

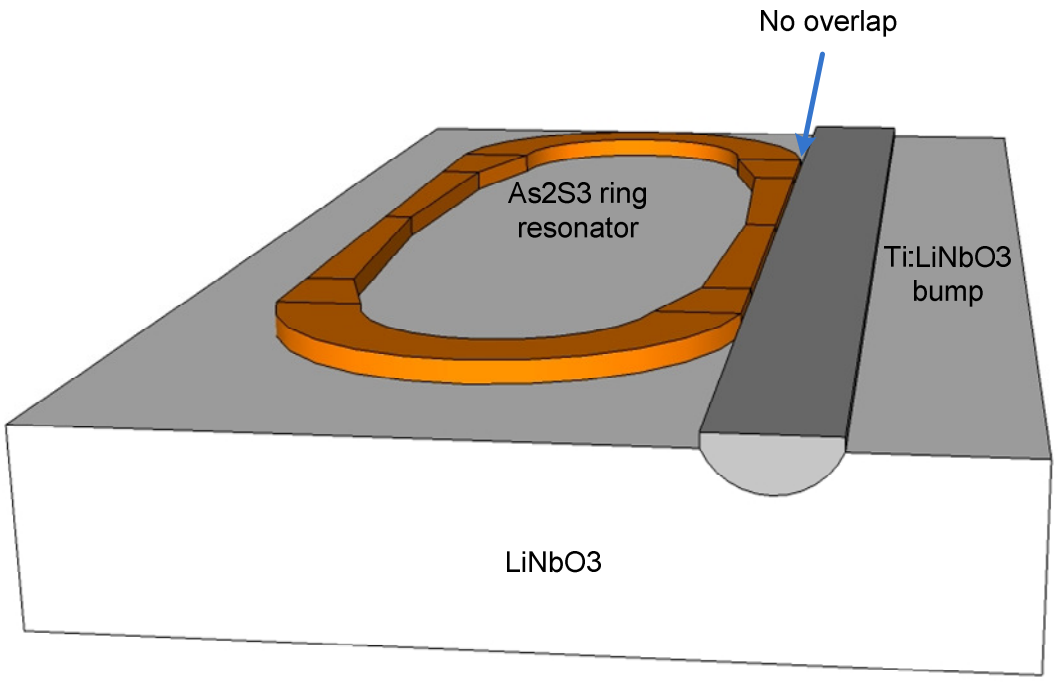

Fig. 4.9 As_2S_3 ring waveguide side-coupled to the Ti:$LiNbO_3$ channel waveguide without overlap

However, the contact photo-lithography method is not able to pattern the As_2S_3 ring waveguide precisely aligned to be side-coupled to the Ti:$LiNbO_3$ waveguide as its minimum feature size is around 1.5~2 μm, while the required controlled gap between the ring and the bus waveguide is about 0.5 μm. In this case, the projection lithography and the E-beam writing lithography are all able to pattern the waveguide with the minimum feature size below 1 μm.

E-beam writing can pattern the waveguide in nanometer scale but it takes very long time to expose the pattern through the E-beam writing. Compared to the E-beam writing, the projection lithography can expose the sub-micron size pattern but the throughput is much more efficient. As our ring waveguide size is relatively large, the projection lithography is used. A schematic figure of a projection lithography is shown in Fig. 4.10.

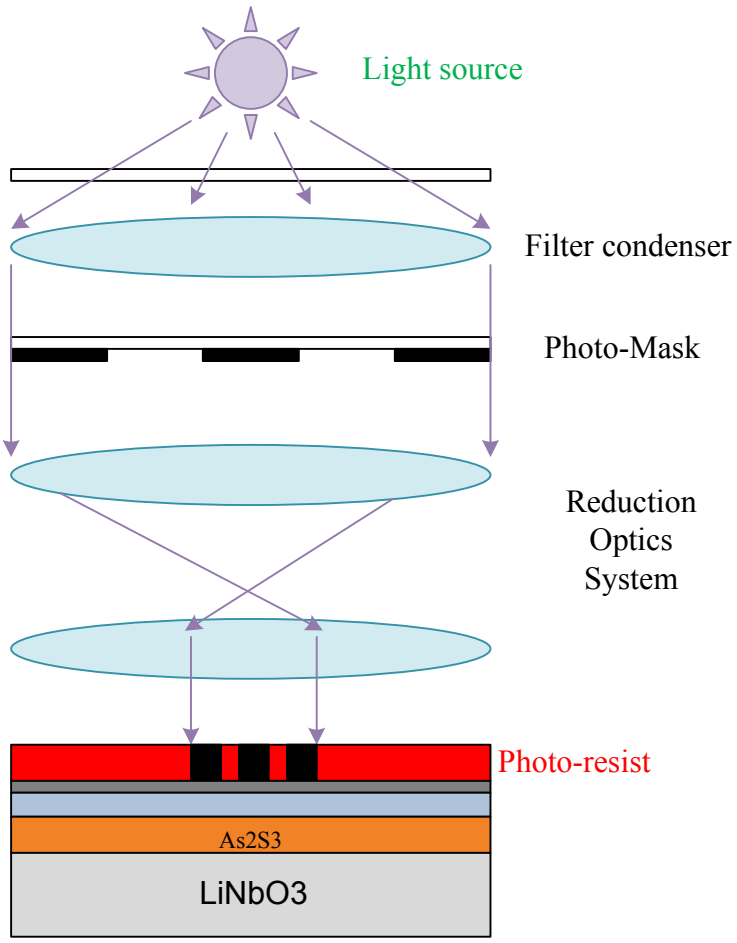

Fig. 4.10 Schematic figure of a projection lithography system

Projection printers were developed to obtain the high resolution of contact printing without the defects. From Fig. 4.10, we can see that the photo-mask is held between the condenser and a second set of lenses called the projector or objective. The purpose of the projector is to re-focus the light onto the wafer.

Part of the light from the mask has been diffracted to a large angle. To try to reimage the pattern onto the wafer, we must at minimum collect that diffracted light. The numerical aperture (NA) of the system is defined as $NA = n\sin(\alpha)$ where α is one-half

the angle of acceptance of the objective lens and n is the refractive index of the media between the objective and the wafer. In the case of optical aligners, the exposure is typically done in air where $n = 1.0$. Typical values for NA range from 0.16 to 0.18.

1:1 scanning systems are being replaced by step and repeat projection aligners. These systems are refractive, frequently with a reduction built in. The steppers used 10:1 reduction lens, 5:1 or 4:1 lenses. This means only a small region of the wafer, called a field, is exposed at a time. This allows systems to be built with very high NAs and therefore, high resolution.

Therefore, compared to the straight As_2S_3-on-$LiNbO_3$ waveguide fabrication, the only difference of making the As_2S_3-on-$LiNbO_3$ ring waveguide side-coupled to the Ti-diffused:$LiNbO_3$ channel waveguide is the lithography process. Projection lithography method was employed to pattern the ring resonator waveguide by stepper in Pennsylvania State University. The scanning system is 10:1 and the minimum feature size is around 0.5~1 μm. The SEM picture of the fabricated As_2S_3 ring back-to-back taper waveguide side-coupled to the Ti waveguide is shown in Fig. 4.11.

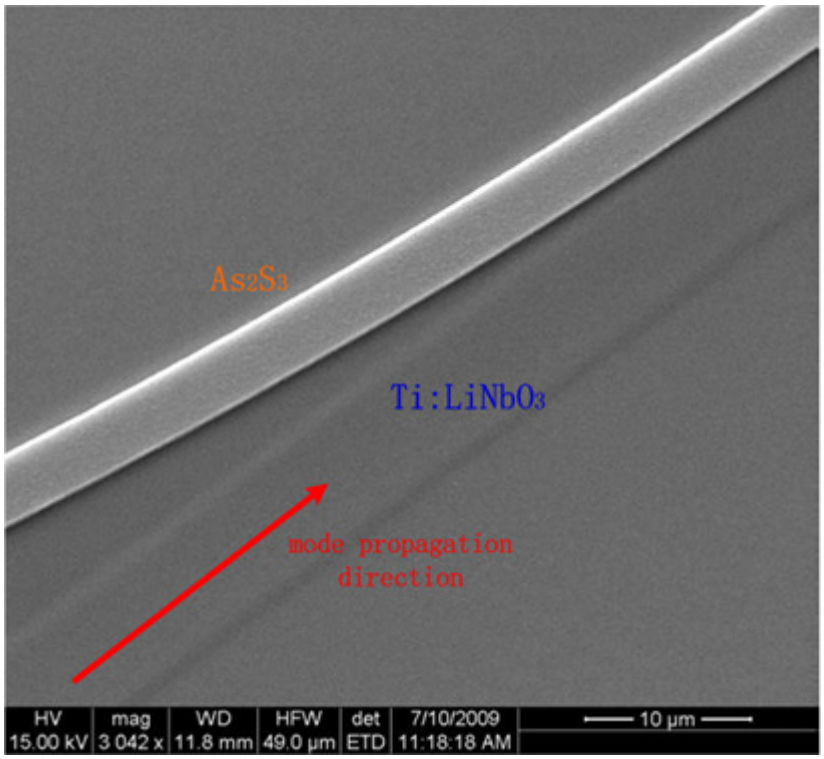

Fig. 4.11 SEM picture of the fabricated As_2S_3 ring back-to-back taper waveguide side-coupled to the Ti waveguide

4.3 Fabrication of the sidewall grating cavity waveguide

As discussed in Chapter III, due to the birefringence property of the $LiNbO_3$ substrate, the TE-mode As_2S_3-on-$LiNbO_3$ bent waveguide would suffer a large bending loss and only TM-mode could be supported in a ring-resonator structure waveguide. For the nonlinear application, compared to the TM mode, the TE mode of the As_2S_3-on-$LiNbO_3$ waveguide has a smaller effective mode area and higher confinement factor, leading to a larger nonlinear waveguide coefficient.

In this case, to realize the TE mode As_2S_3-on-$LiNbO_3$ waveguide cavity structure, the sidewall grating cavity waveguide is proposed, also as discussed in detail in Chapter III. The sidewall gratings are patterned on both side of the As_2S_3 strip waveguide. The widest width of the waveguide is defined as w_1 while the narrowest part is defined as w_2. The grating depth is calculated by $\Delta w = (w_2 - w_1)/2$. The grating period Λ is given by $\Lambda = \lambda_B / (2n_{eff})$ in which λ_B is the center wavelength of the grating reflection wavelength and n_{eff} is the effective mode index of the hybrid waveguide. The duty cycle is defined as τ / Λ. The largest grating coupling strength is achieved when the duty cycle is 0.5. A small portion of the sidewall grating waveguide is shown in Fig. 4.12.

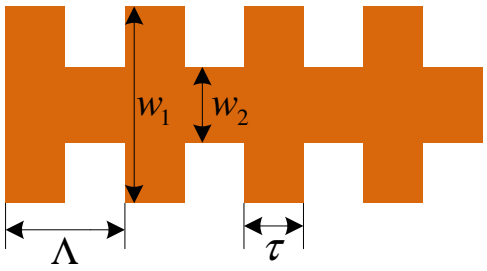

Fig. 4.12 A schematic figure of a small portion of the sidewall grating waveguide

In our design, the grating period Λ is about 800 nm and τ is 400 nm if the duty cycle is chosen as 0.5. To pattern the sub-micron feature size device, E-beam writing lithography is the best solution for its most accuracy and capability of writing nano-meter scale structures.

If the electron beam is regarded as a wave, its wavelength is much smaller than the optical light source, indicating that the electron beam lithography would break the diffraction limit of the UV light photo-lithography. The working principle is very similar to the traditional photo-lithography process. First, the selected E-beam resist which is sensitive to the electron beam exposure would be coated on the wafer surface by spin coating. After the soft-bake process, the sample would be loaded into the E-beam writer chamber. Different from the photo-lithography where a large window of the sample is exposed together, e-beam has a very small beam width which only allows local exposure at one time. Compared to the photo-lithography which uses UV light exposure to transfer the pattern from the photo-mask to the photo-resist, the E-beam writer reads the GDS file which contains the pattern structure and then scan the substrate surface and uses the electron beam to expose the pattern.

After exposure, the developing process would remove the exposed e-beam resist region (positive resist) or keep the exposed e-beam resist region (negative resist) and remove the unexposed part.

For our As_2S_3 grating waveguide E-beam lithography process, the most challenging part is the selection of the appropriate E-beam resist and the development of the fabrication process based on the selected resist.

4.3.1 E-beam lithography using HSQ resist

The first E-beam resist we used was hydrogen silsesquioxane (HSQ) resist for its ultra-high resolution and good contrast. Its resolution limit is around 10 nm which is

perfect for the nano-scale feature size device patterning. The chemical developer of the HSQ resist is MF-321 solution which contains 20% tetramethylammonium hydroxide (TMAH). To protect the As_2S_3 thin film from the developer, a protective layer of SiO_2 and Ti are deposited on top of the As_2S_3 material.

The HSQ is a negative resist which means the electron-beam exposed region would be kept while the unexposed part would be dissolved during the developing. One special feature of HSQ resist is that after the developing process, the un-dissolved E-beam resist would become SiO_2, which is shown in Fig. 4.13.

Fig. 4.13 HSQ E-beam resist becoming SiO_2 after exposure and developing

The biggest problem using HSQ as E-beam resist is from the followed RIE etching process. Normally, during the etching process, there should be a big etching selectivity between the patterned region and the un-patterned region. In optical photo-lithography, the photo-resist acts as a protective mask to keep the patterned region from the etching. However, in this case, the protective mask is SiO_2, which means the etching

selectivity between the patterned and un-patterned region is the same. Then, over-etching problem is unavoidable, as shown in Fig. 4.14. The SEM picture of the over-etched grating waveguide is shown in Fig. 4.15.

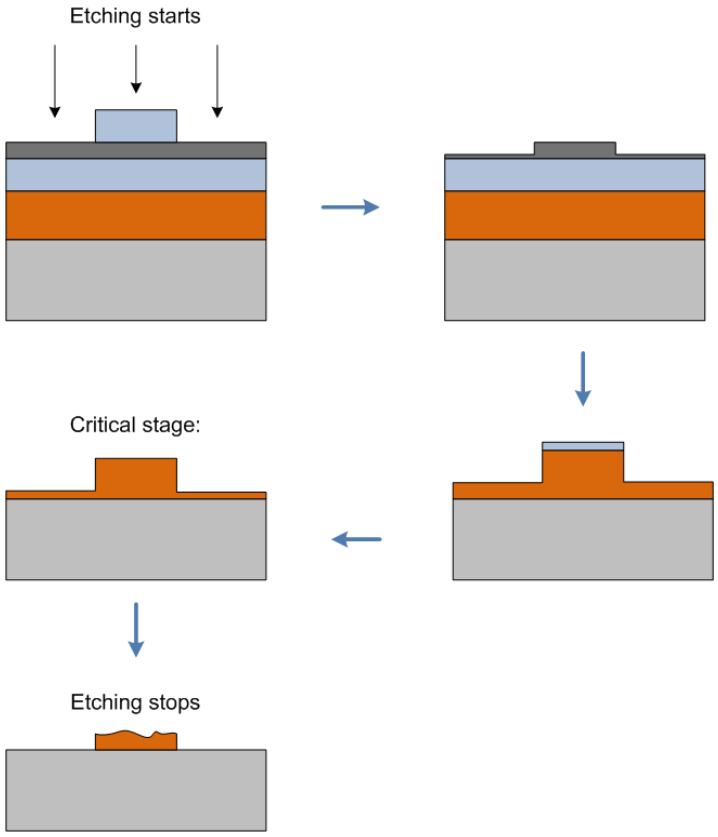

Fig. 4.14 Schematic figure of etching process by using HSQ as E-beam resist

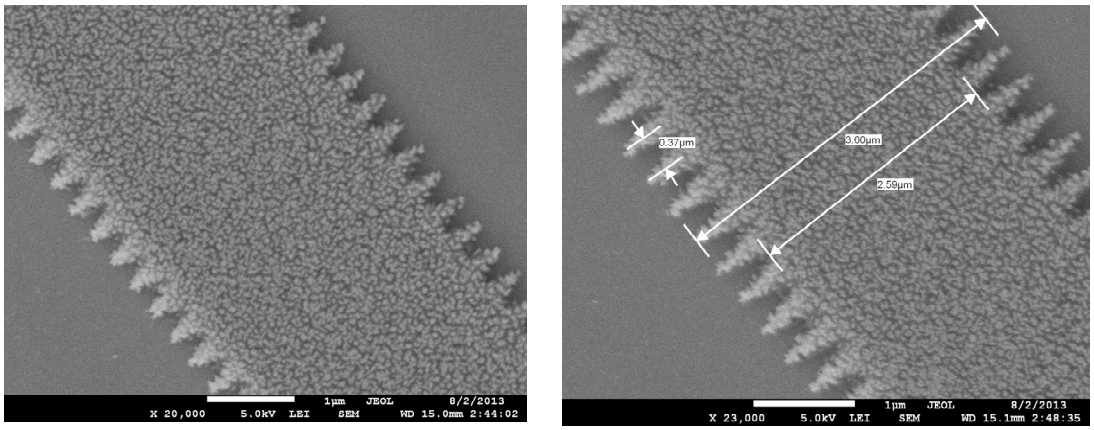

Fig. 4.15 SEM pictures of the over-etched As_2S_3 grating waveguide

4.3.2 E-beam lithography using PMMA resist

To effectively protect the waveguide region during the etching process, the etching mask should be resistant to the etching chemicals. From our research, all kinds of E-beam resist themselves could not be able to protect the As_2S_3 material. Instead, Cr metal is an ideal material as the etching mask.

Therefore, a positive E-beam resist should be selected and a liftoff process is followed to deposit the Cr metal on top of the waveguide region. A 9% 950PMMA C resist diluted to 3% with PMMA thinner is selected as the E-beam lithography resist. After spin coating and a 2-minute 180 ˚C soft bake, the sample is loaded into the E-beam writer and exposed. The developer is isopropyl alcohol mixed with DI water at 2:1 ratio. The exposed part would be dissolved in the developer.

A thin layer of Cr metal of 30 nm thickness would be deposited on the sample by E-beam evaporation. The reason by using E-beam evaporation instead of sputtering to deposit the Cr metal is that the liftoff process requiring the anisotropic thin film

deposition. The E-beam evaporation would not deposit the material on the sidewall of the resist. After the Cr deposition, the liftoff is followed by immersing the sample in the acetone. To help better remove the un-patterned region Cr metal, the liftoff baker is placed in the ultrasonic oven. The whole fabrication process is shown in Fig. 4.16.

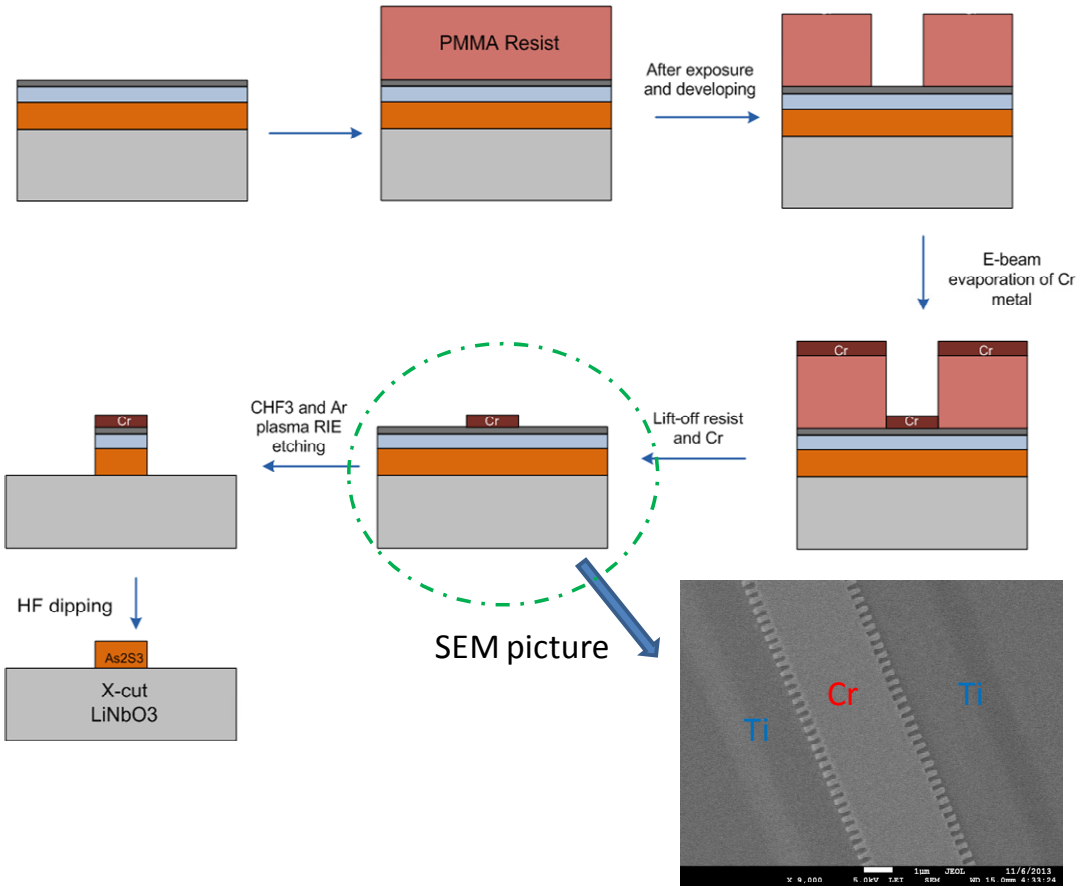

Fig. 4.16 The liftoff process by using PMMA as the E-beam resist, the insert small picture is the SEM picture of the grating waveguide after liftoff

CHAPTER V

MEASUREMENTS AND RESULTS*

5.1 S-bend waveguide using two-stage taper coupler

As discussed in Chapter III, the most fundamental and critical waveguide component is the taper coupler waveguide. To efficiently couple the light from the Ti-diffused:$LiNbO_3$ waveguide into the As_2S_3 waveguide, a two-stage taper coupler is designed and simulated. To test the coupling performance of the designed two-stage taper coupler, an S-bend waveguide was proposed, as shown in Fig. 5.1.

---

* Part of this chapter is reprinted by the permission from "Two-stage taper enhanced ultra-high Q As_2S_3 ring resonator on $LiNbO_3$" by Yifeng Zhou, Xin Xia, William T. Snider, Jaehyun Kim, Qi Chen, Wee C. Tan and Christi Madsen, IEEE Photonics Technology Letters, Vol. 23, No. 17, copyright 2011 by IEEE.

* Part of this chapter is reprinted by the permission from "Fabrication and measurement of sidewall gratings integrated in hybrid As_2S_3-Ti:$LiNbO_3$ optical waveguides" by Xin Wang, Yifeng Zhou and Christi Madsen, Journal of Lightwave Technology, Vol. 21, Issue 17, copyright 2014 by IEEE.

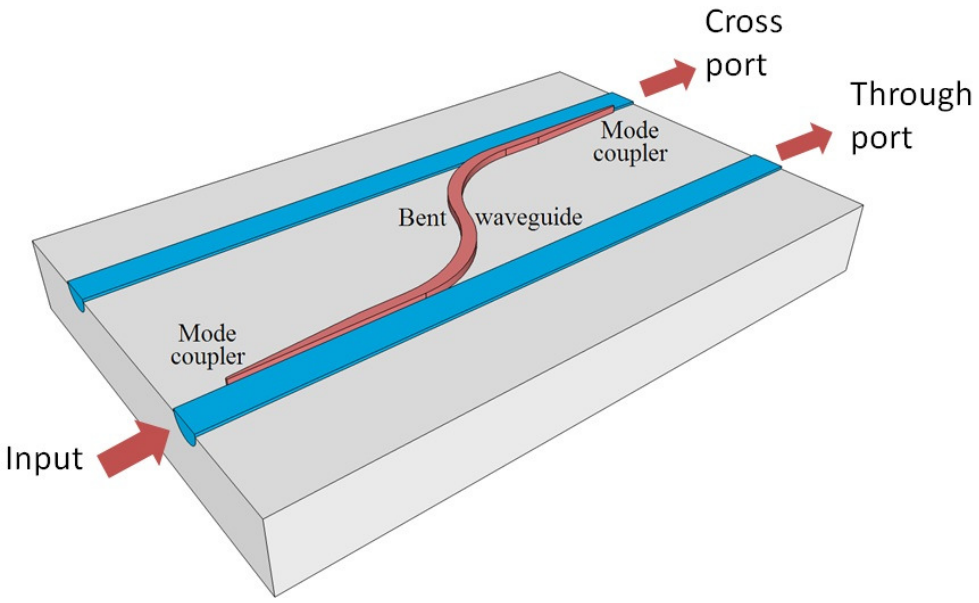

Fig. 5.1 S-bend waveguide for testing the two-stage taper coupler

As shown in Fig. 5.1, it is composed of two taper couplers and an S-shaped As_2S_3 waveguide to connect them. The taper couplers follow the two-stage taper coupler design.

The device is fabricated using photolithography and dry-etch technology. The substrate $LiNbO_3$ is a birefringence crystal with refractive index no=2.2119 and ne=2.1386 (λ=1531 nm), placed in x-cut, y-propagation manner. The titanium diffused waveguide is fabricated through sputtering of a 95 nm thick titanium layer, patterning into 7 μm wide strip with photolithography and reactive ion etching (RIE), diffusion for 9 hours at 1025 ℃ and optical polishing on end-facets.

For As_2S_3 waveguide fabrication, a layer of 0.47 μm thick As_2S_3 film is deposited on the titanium waveguide sample using an RF sputtering system, along with a

protective layer of SiO_2 and Ti, which protects the As_2S_3 from being dissolved by developers. Then the projection photolithography is carried out, and the 1.0 μm wide taper tip can be produced. After that, the T_i-SiO_2-As2S_3 stack is etched through to the substrate by RIE. And Ti-SiO_2 is removed in diluted hydrofluoric solution at last.

The hardbake time is prolonged in order to obtain smother sidewalls by the resist reflow process, which, however, causes an expansion of As_2S_3 waveguide to certain degree, up to 0.5 μm. The average tip width (i. e. the initial width) of tapered As_2S_3 waveguide after fabrication is 1.3 μm.

Instead of working at a single wavelength, these practical taper couplers are designed to work for a wavelength range. Accordingly, their coupling behaviors in frequency domain are studied. The measured spectrum at the cross port is presumably to have the same trends of the coupling spectrum, with an offset from the exact values. That offers the information of taper couplers in the frequency domain and can be used as another means to test our simulation method. The typical measured spectrum, along with simulation results is shown in Fig. 5.2. In simulation the wavelength is scanned correspondingly from 1520 nm to 1600 nm, at the interval of 2 nm. The results show that, though the taper coupler exhibits certain degree of wavelength dependency, it has high coupling efficiency over a broad bandwidth.

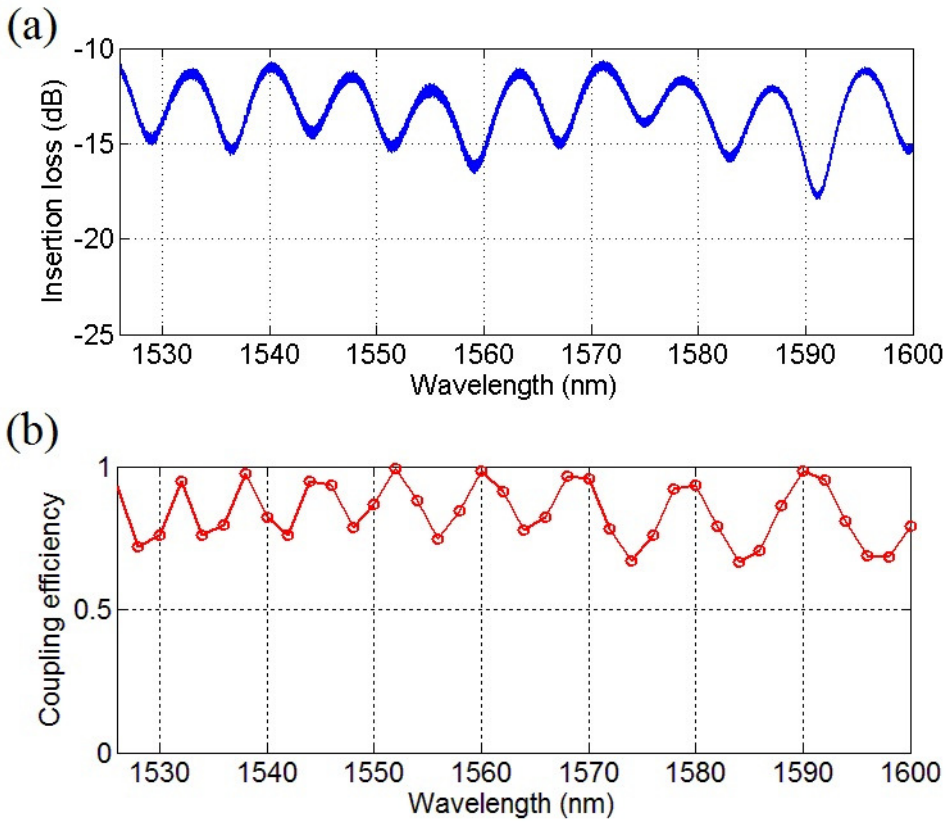

Fig. 5.2 Measured (a) and simulated (b) coupling spectra of taper coupler with tip width = 1.3 μm

From the curve, we can see that the period of oscillation is less than 10 nm, and longer wavelengths have a larger oscillation period than shorter wavelengths. The oscillation of the coupling curve is a strong indication of mode beating while the phenomenon that longer wavelengths have a slightly larger oscillation period possibly comes from waveguide dispersion: the wavelength-dependent propagation constant. Simulation shows that when the wavelength varies from 1530 nm to 1540 nm, the confinement of the mode in As_2S_3 waveguide changes from 0.4536 to 0.4459 and the

effective index changes from 2.2345 to 2.2331. Consequently, the propagation constant changes from 9.1763 to 9.1110, decreasing by 0.7%. We can learn that different wavelengths have different critical widths, which shifts to a larger value as the wavelength increases. Such change makes the mode at different wavelengths see the taper coupler slightly different, and the energy transfer does not take place at the same location: the mode of shorter wavelength couples before that of a longer wavelength does.

5.2 As_2S_3-on-$LiNbO_3$ ring resonator

Standard microelectronic device technology is used for fabrication. Our As_2S_3-on-$LiNbO_3$ ring waveguide fabrication starts by creating a 7-μm wide straight Ti-diffused waveguide on $LiNbO_3$ substrate. DC sputtering was used to deposit a 95 nm thick titanium (Ti) thin film on top of an x-cut y-propagation $LiNbO_3$ substrate. Photolithography and reactive ion etching (RIE) followed to form a straight 7-μm wide Ti waveguide pattern on the substrate. After diffusion for 9.5 h in wet breathing air ambient at 1025 °C, the end facets of the substrate were polished to minimizing coupling loss. Tested by butt-coupling single-mode fiber to the substrate with index matching gel, the insertion loss of a typical Ti-diffused waveguide is 2.5 ± 0.5 dB. A 0.47-μm thick thin film of As_2S_3 was then deposited on top of the fabricated Ti-diffused:$LiNbO_3$ substrate by RF magnetron sputtering [10]. A protective layer of SiO_2 and Ti was deposited over the As_2S_3 thin film to prevent it from reacting in (CH3)4NOH-based photo-resist developer. Projection lithography and subsequent RIE etching in an

Ar/CHF3 plasma were used to form the As_2S_3 ring pattern on the substrate. An annealing process at 130°C in vacuum atmosphere was employed to further decrease the propagation losses in the As_2S_3 waveguide.

The schematic figure of the measurement setup was shown in Fig. 5.3. The core equipment of the measurement system is an optical vector analyzer from LUNA Tech which combining the tunable continuous wavelength laser source and the spectrum analyzer in a whole system. Meanwhile, the optical vector analyzer is pre-installed with an analyzing software which could save spectrum magnitude, group delay and time-domain information. The measurement setup also includes the fiber-device under test-fiber alignment stages.

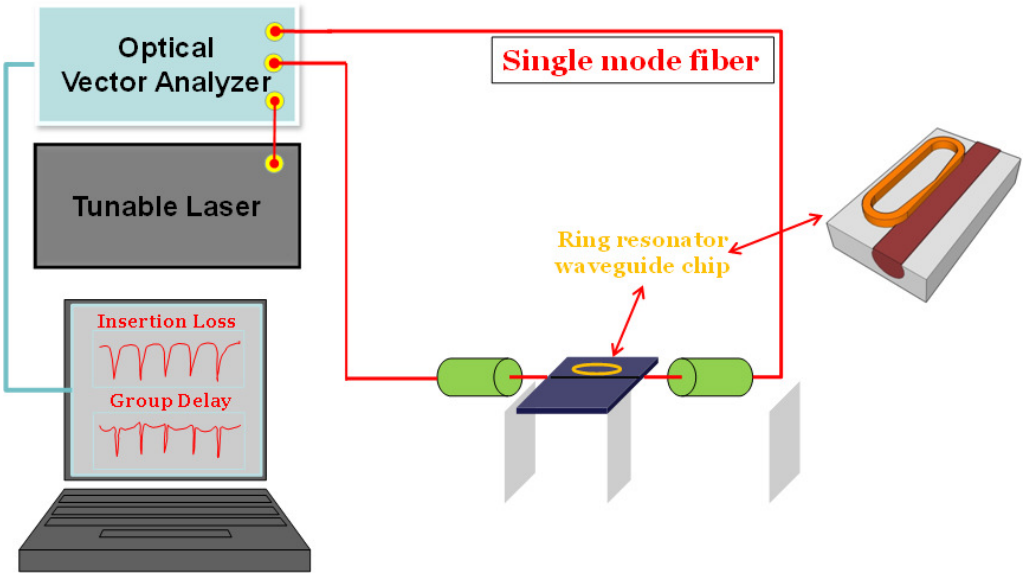

Fig. 5.3 Optical measurement setup of the ring-resonator chip

Mathematically, the ring resonator based all-pass filter can be described with the transfer equation at the z-domain by the digital signal processing method:

$$H(z) = \frac{(c - \gamma z^{-1})}{(1 - c\gamma z^{-1})} \tag{5.1}$$

If the feedback path is lossless, then the ring resonator yields an ideal optical all-pass filter. Optical all-pass filters can be used as building blocks to create higher-order optical bandpass filters which have optimal digital filter design characteristics, such as Butterworth and Chebyshev filters.

In equation (5.1), $c = \sqrt{1-k}$, $z = e^{i\beta L}$, $\gamma = e^{-\alpha L}$, k is the power coupling ratio, β is the propagation constant, αL is the ring round-trip loss, and L is the circumference of the ring resonator. In an optical all-pass filter, there is no ring round-trip loss and the loss term γ is one. To determine c and γ, both magnitude and phase responses of the ring resonator are needed. We measured the magnitude response and group delay of the As_2S_3 ring using a LUNA Technologies optical vector analyzer (OVA) with a tunable laser source. The full Jones Matrix of the device under test (DUT) was measured and fitted to extract the coupling strength and round-trip loss of the ring.

The fabricated TM-mode ring resonator waveguide to be measured has the followed key parameters: the coupling region was the back-to-back two-stage taper coupler side-coupled to the Ti channel waveguide in which the first stage taper was 1.3~1.6 μm width at 2 mm length and the second stage taper was 1.6~3.5 μm width at 1 mm length; the total round-trip length of the ring resonator was 1.7 cm long and the bent

radius was 400 µm; the ring resonator was designed with an ultra-narrow free spectral range (FSR) of 0.0579 nm.

The fitting was done across 4 FSRs at a center wavelength of 1546 nm. With the minimum insertion loss of 8.4 dB, the fitted power coupling ratio and round-trip loss from the measured magnitude and group delay response were 41% and 2.1 dB respectively, for TM polarization. For a round-trip path length of 1.7 cm, this corresponds to a 1.2 dB/cm propagation loss. The excess transmission loss is attributed to the propagation loss created by the Ti-diffused waveguide. The measurement and fitting results are shown in Fig. 5.4. The fit for both the magnitude and group delay can be excellent by using the simple model in equation (5.1). Even with the limited frequency resolution, the peak group delay for sharp responses can be well estimated.

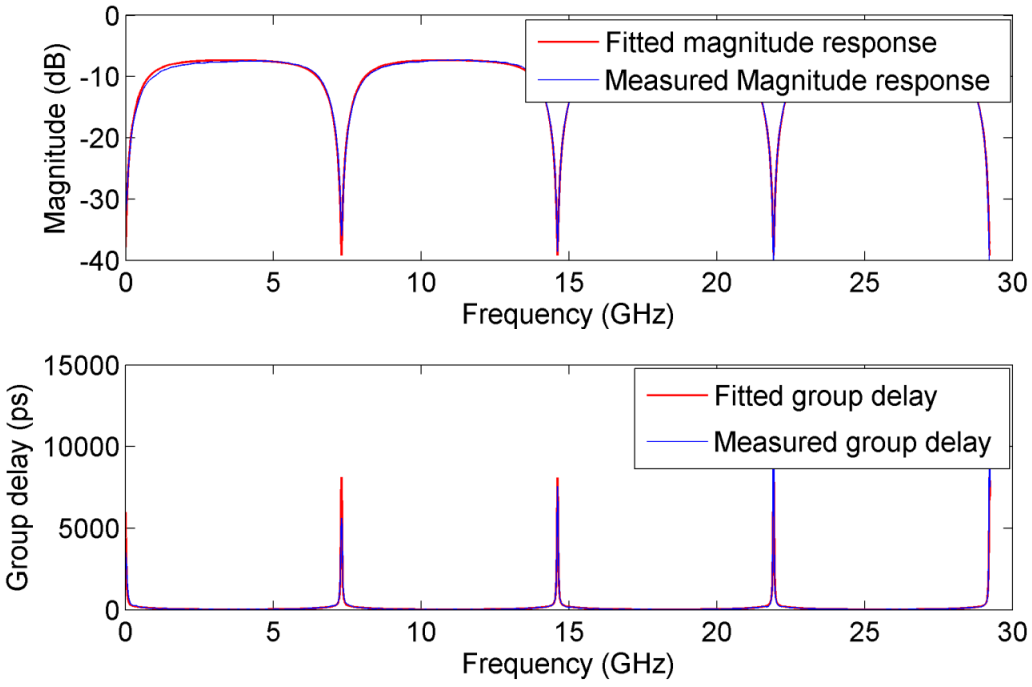

Fig. 5.4 Transmission and group delay response of As_2S_3-on-Ti:$LiNbO_3$ ring resonator

The periodic coupling beating phenomenon also shows up at the ring resonator waveguide which is discussed in the previous section of the S-bend waveguide, as shown in Fig. 5.5. When the wavelength varies, confinement of the mode in the As_2S_3 waveguide changes, and the effective index changes correspondingly. Such changes make the mode at different wavelengths see the taper coupler differently, and the energy transfer does not take place at the same location.

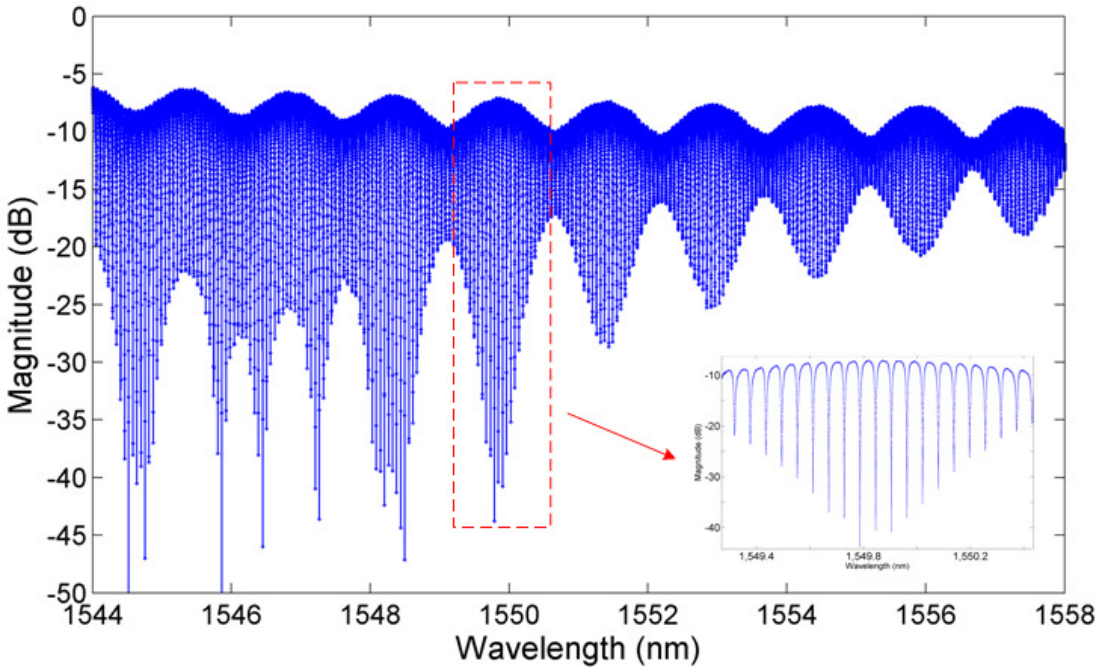

Fig. 5.5 Coupling oscillation phenomenon of ring resonator

5.3 As_2S_3-on-$LiNbO_3$ sidewall grating coupler and cavity waveguides

Sidewall grating waveguides have the advantages of strong coupling strength, compact device size and simple lithography process. Compared to a ring resonator

structure which consists of a straight bus waveguide connected to a ring waveguide by a coupling region, the sidewall grating cavity waveguide is simply made by two identical sidewall grating couplers connected by a straight uniform waveguide, which need no concerns about the bending loss from the ring structure. Meanwhile, the benefits by using the $LiNbO_3$ as the substrate mainly show in three aspects. Firstly, its much lower refractive index compared to As_2S_3 material enables a strong mode confinement for a high integration density. Secondly, it is very easy to make a high quality, low loss channel waveguide by diffuse titanium strip into the $LiNbO_3$ substrate. The mode size of the diffused channel waveguide is well close to the mode size of a single mode fiber, which helps to minimize the fiber-to-chip coupling loss, as low as 0.5 dB per facet. And thirdly, the excellent birefringence property of $LiNbO_3$ substrate enables its high efficiency in parametric frequency conversions, which explores the good potential in the nonlinear applications by the hybrid As_2S_3-on-$LiNbO_3$ material platform.

The integrated optical cavity waveguide is consisted of two identical sidewall grating couplers with a straight long uniform waveguide in the middle, as discussed in Chapter III. A two stage taper design is employed to efficiently couple the optical mode from the Ti diffused channel waveguide into the As_2S_3 waveguide.

To evaluate the coupling and reflection performance of the sidewall grating inside the cavity structure, a testing structure of a single sidewall grating coupler is designed, as shown in Fig. 5.6.

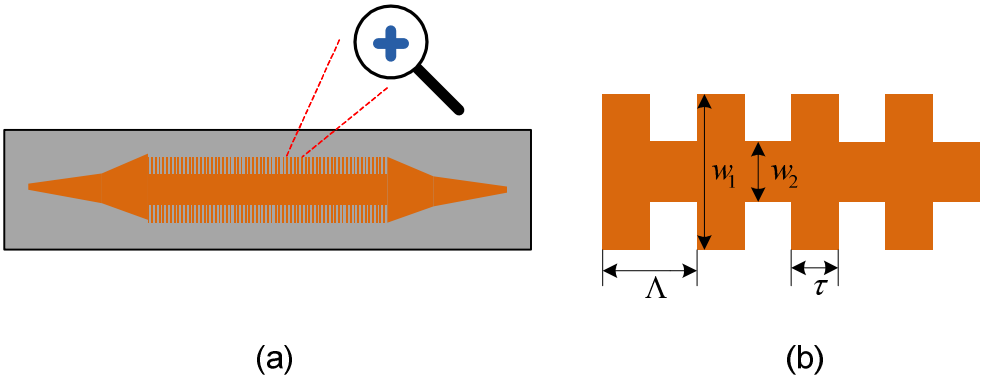

Fig. 5.6 (a) Test structure of a single sidewall grating coupler; (b) Zoom-in view of the sidewall grating structure

The sidewall gratings are patterned on both side of the As_2S_3 strip waveguide. The widest width of the waveguide is defined as w_1 while the narrowest part is defined as w_2. The grating depth is calculated by $\Delta w = (w_2 - w_1)/2$. The grating period Λ is given by $\Lambda = \lambda_B / (2n_{eff})$ in which λ_B is the center wavelength of the grating reflection wavelength and n_{eff} is the effective mode index of the hybrid waveguide. The duty cycle is defined as τ / Λ. The largest grating coupling strength is achieved when the duty cycle is 0.5. The total grating length L_g is defined as the number of period N multiplying the period Λ. For an average grating width $w_0 = (w_1 + w_2)/2$ as 3.2 μm, the effective index is estimated around 2.153523 and the period Λ is calculated about 0.36 μm. For a grating depth of 800 nm and number of periods of 500, the grating coupling strength is 8.75 mm^{-1}. The As_2S_3 waveguide thickness is selected as 0.3 μm to meet the designed effective grating waveguide mode index.

Standard microelectronic device technology is used for fabrication. Our As_2S_3-on-$LiNbO_3$ waveguide fabrication starts by creating a 7-µm wide straight Ti-diffused waveguide on $LiNbO_3$ substrate. DC sputtering was used to deposit a 95 nm thick titanium (Ti) thin film on top of an x-cut y-propagation $LiNbO_3$ substrate. Photolithography and reactive ion etching (RIE) followed to form a straight 7-µm wide Ti waveguide pattern on the substrate. After diffusion for 9.5 h in wet breathing air ambient at 1025 °C, the end facets of the substrate were polished to minimizing coupling loss. Tested by butt-coupling single-mode fiber to the substrate with index matching gel, the insertion loss of a typical Ti-diffused waveguide is 2.5 ± 0.5 dB. A 0.3-µm thick thin film of As_2S_3 was then deposited on top of the fabricated Ti-diffused:$LiNbO_3$ substrate by RF magnetron sputtering. A protective layer of SiO_2 and Ti was deposited over the As_2S_3 thin film. E-beam writing lithography and PMMA resist is used to pattern the sidewall grating cavity waveguides on top of the substrate. After the PMMA resist development, a thin layer of chromium is deposited on top of the resist layer as the etching mask. The detailed discussion of the fabrication process of the grating coupler waveguide can be seen in Chapter IV.

The measurement of the test structure of the sidewall grating couplers was also done by the optical measurement system in Fig. 5.3. The transmission and the reflection response of the sidewall grating coupler waveguide are shown in Fig. 5.7.

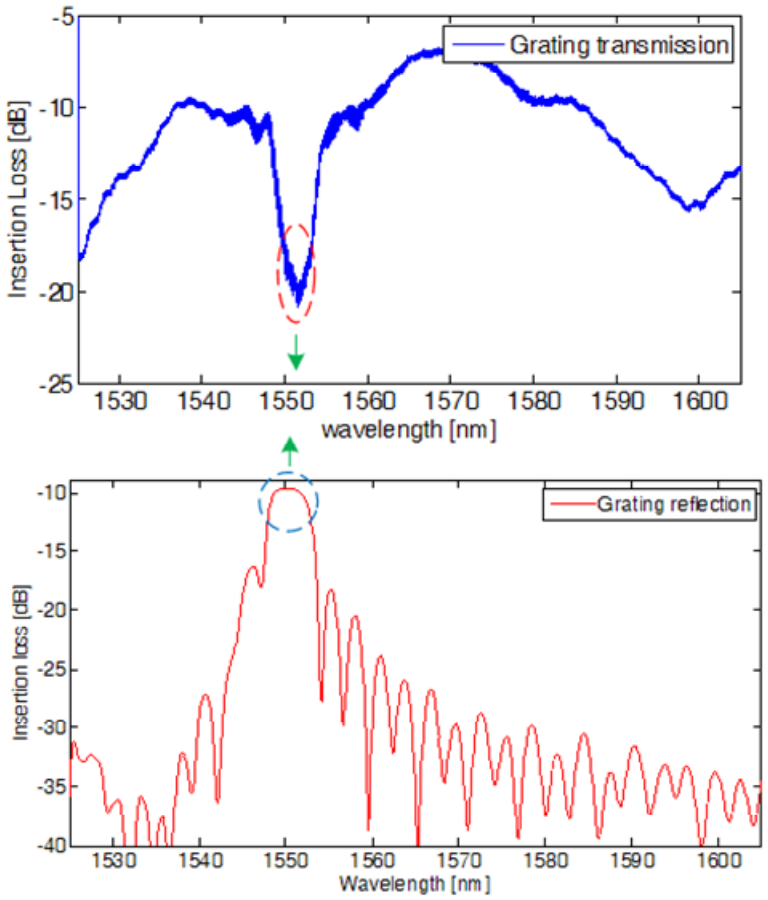

Fig. 5.7 Transmission and reflection response of a single sidewall grating coupler waveguide

The measurement and fitting of the grating coupler cavity waveguide was shown in Fig. 5.8.

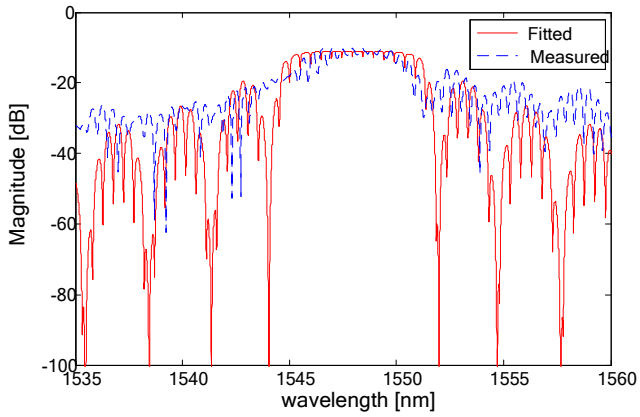

(a)

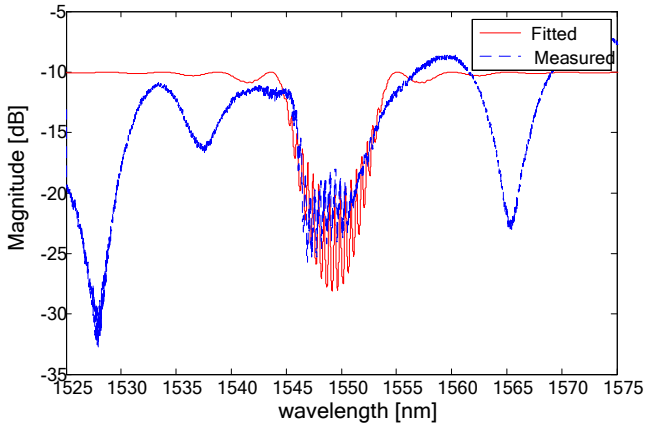

(b)

Fig. 5.8 Measurements and fittings of (a) reflection and (b) transmission of a sidewall grating cavity

From the fitting results, the coupling strength is estimated at around 14 mm^{-1}, which is much larger than the expected 9 mm^{-1}. The propagation loss inside the cavity is calculated and estimated 2.5 dB/cm from the reflection response at 1.55 μm. However, an insertion loss, i.e. chip waveguide loss, is estimated around 10~12 dB which would weaken the resonator response from the cavity waveguide. To minimize the waveguide loss, further steps should be considered. The Ti-diffused channel waveguide is not flat

and has a rough bump on the substrate surface. Chemical-mechanical planarization (CMP) method can be taken into the fabrication process to make the substrate surface flat and thus reduce the hybrid waveguide loss. The other solution is to directly make the As_2S_3 waveguide on top of the $LiNbO_3$ substrate instead of on top of the Ti diffused channel waveguide. Fiber-to-As_2S_3 waveguide direct coupling would be used to couple the light from the laser source to the hybrid waveguide and then couple into the detector.

5.4 Nonlinear measurement of ring resonator waveguides

As_2S_3 (or other chalcogenide materials, such as As_2Se_3) glass shows a good potential as a Kerr medium for ultra-fast all-optical tuning capability because of its high nonlinearity coefficient at infrared wavelength range. At the same time, resonance cavity devices are favored for their easily tunable ability as a small change of refractive index in the material would lead to a shift for their resonance. Therefore, the nonlinear Kerr process in As_2S_3 material can be applied to our As_2S_3-on-$LiNbO_3$ ring resonators and used as ultra-fast all-optical tunable on-chip devices.

A measurement system was setup for measuring nonlinearity in As_2S_3-on-$LiNbO_3$ ring resonators. The schematic figure of setup was shown in Fig. 5.9.

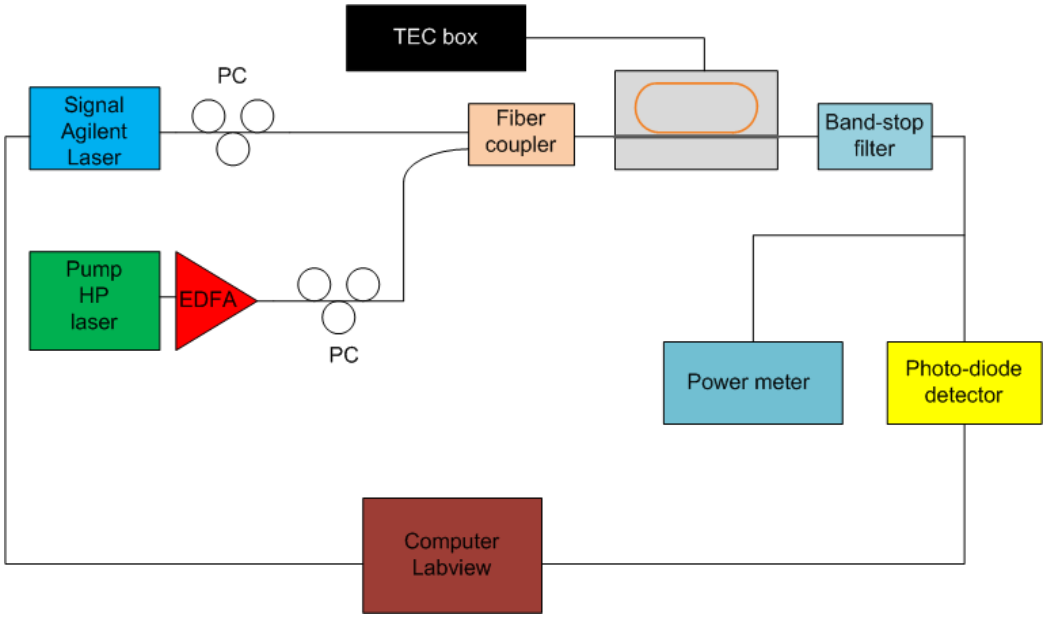

Fig. 5.9 Schematic figure of nonlinear measurement setup

An Agilent tunable laser was used as the sweeping signal source while the other HP tunable laser was employed as the single-tone pump source, which provided the high power inside the waveguide for nonlinearity. Due to the fact that the ring waveguide was designed for only TM-polarization, two polarization controllers were used to make the output from the laser TM-polarization light. A fiber combination coupler would mix the two paths signal by a certain percentage (98% for pump path and 2% for signal path) and then couple them into the ring resonator waveguide. A band-pass filter (1552~1557 nm) was put after the output of the ring waveguide to block the pump power and only pass through the signal power into the photo-diode detector. The sweeping of the signal and the reading of data from the photo-diode were operated by a Labview program.

At the same time, to avoid the thermal-induced material property change during the nonlinear process, the ring waveguide sample was put on a measurement stage made of aluminum with good thermal-conductivity. The measurement stage was also connected to a thermal-electrical controlling box which provided cooling if the temperature of the stage was higher than room temperature at 27 °C.

A picture of the real measurement setup in our lab was shown in Fig. 5.10.

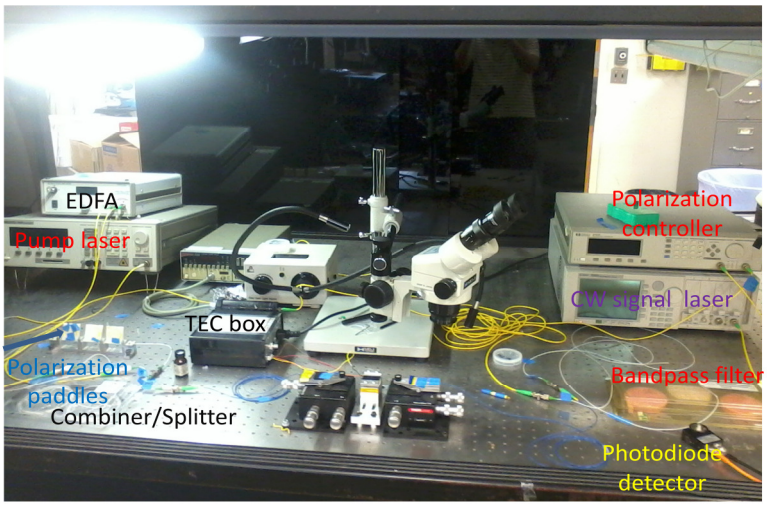

Fig. 5.10 Nonlinear measurement setup

A resonance tuning of the ring response was measured based on the fabricated TM-mode As_2S_3-on-$LiNbO_3$ ring resonator device, as shown in Fig. 5.11.

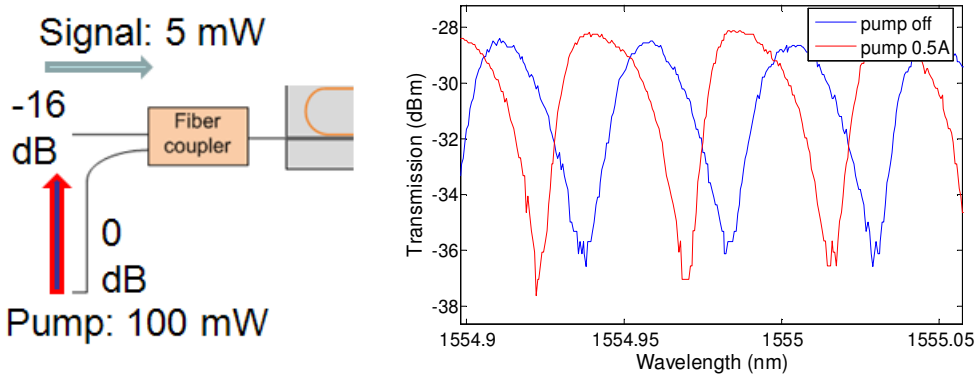

(a) (b)

Fig. 5.11 (a) Signal/Pump power coupling into ring sample (b) measured ring resonance shift

In the measurement, the signal is with 5 mW of power and the pump is with 100 mW of power at wavelength of 1564.902 nm.

The measured phase shift from the nonlinear tuning can be given by the equation $\Delta\varphi = \frac{2\pi n_g}{\lambda_1} L - \frac{2\pi n_g}{\lambda_2} L$. Here, λ is the resonance wavelength and n_g is the group index of the As_2S_3 waveguide mode which is assumed as 2.8. L is the ring resonator round-trip length and is calculated as 1.7 cm. From the measurement figure, the resonant wavelength was shifted from 1554.935 nm to 1554.925 nm. And the calculated phase shift thereby is 0.39 π.

We can also estimate the nonlinear index n_2 from the measurement results. By the equation $\phi_{NL} = \frac{2\pi n_2}{\lambda_0 A_{eff}} L_{eff} P_0$, ideally, for a peak power of 41 mW and 1.2 dB/cm propagation loss, a 1.7-cm long ring resonator at 1.55 μm can give a nonlinear phase

shift of π. Experimentally, assuming the propagation loss of 5 dB/cm and peak power 50 mW inside the waveguide, it gave a nonlinear phase shift of 0.39 π. Therefore, we can roughly estimate the nonlinear index as $n_2 = 2.6 \times 10^{-18} m^2 / W$.

CHAPTER VI

CONCLUSION

In this dissertation, the arsenic trisulfid (As_2S_3) on lithium niobate ($LiNbO_3$) substrate vertically integrated waveguide devices were studied. The As_2S_3-on-$LiNbO_3$ optical waveguides were designed, fabricated and characterized with various structures, including the taper couplers, race-track ring resonators and sidewall grating couplers. At the same time, the nonlinear effects were also measured with a pump-signal optical measurement setup on the fabricated As_2S_3-on-$LiNbO_3$ ring resonator waveguides.

To efficiently couple the optical light from the Ti-diffused $LiNbO_3$ channel waveguide to the As_2S_3 waveguide, a two-stage taper coupler structure was simulated and proposed. The taper coupler was designed with the super-mode theory and the guideline of the adiabatic taper. The performance of the two-stage taper coupler was evaluated through a single S-bend structure waveguide. The measurement results indicated that compared to the old single stage linear taper coupler, the two-stage taper coupler could achieve a 90% coupling strength with a significantly shorter total length by 60%.

The race-track As_2S_3-on-$LiNbO_3$ ring resonator waveguides were designed, fabricated and characterized. The coupling region designed employed a back-to-back taper coupler based on the two-stage taper structure. With the improved fabricated process by using projection photo-lithography instead of the contact photo-lithography, a propagation loss as low as 1.2 dB/cm was demonstrated on a 1.7-cm long path, 400-μm

bend radius As_2S_3-on-$LiNbO_3$ ring resonator waveguide with a FSR of 0.0579 nm, which corresponds to an ultra-high Q value of $3.5x10^5$. This is the highest Q-factor reported for chalcogenide ring resonator planar waveguide devices.

Due to the birefringence property of the $LiNbO_3$ material, on the X-cut Y-propagation $LiNbO_3$ substrate, the TE mode inside the As_2S_3 waveguide would see a changing refractive index along the bend waveguide. Thus only TM mode resonator waveguide could be realized by the ring structure. To realize the TE resonator waveguide with As_2S_3-on-$LiNbO_3$ platform, a sidewall grating resonator waveguide was designed, fabricated and optically tested. Using the sidewall grating couplers with a coupling strength as high as 14 mm^{-1}, the cavity resonant response with a FSR of 0.5 nm over a 5 nm bandwidth at 1.55 μm was demonstrated with a cavity propagation loss at 2.5 dB/cm.

To test the nonlinear performance of the fabricated As_2S_3-on-$LiNbO_3$ resonator waveguide devices, a pump-signal optical testing system was setup. A tunable continuous wavelength signal and a single-tone pump optical signal were coupled into the waveguide by an optical fiber combiner. And an optical fiber bandpass filter was put after the output side to remove the pump signal entering the photo diode detector. To avoid the thermal induced nonlinear effects inside the As_2S_3 materials, the As_2S_3 ring waveguide chip was measured placed on a good thermal-conductive aluminum sample stage connected to a thermal-electro controlling box. With the continuous wavelength signal power at 5 mW and the single tone pump power at 100 mW coupled into the waveguide via a 5%:95% ratio fiber multiplexer, the resonant spectrum was measured

blue-shifted and a 0.40-π phase shift was demonstrated at the resonant wavelength of 1554.935 nm.

With the realization of the nonlinear optical resonator waveguide devices based on the As_2S_3-on-$LiNbO_3$ material platform, more complicated and advanced optical devices could be built on multiple resonators which opened the window for the all-optical integrated circuits in the near future.

REFERENCES

[1] B. J. Ainslie and C. R. Day, "A review of single-mode fibers with modified dispersion characteristics", Vol. 4, No. 8, Journal of Lightwave Technology, 1986

[2] A. Liu, L. Liao, D. Rubin, H. Nguyen, B. Ciftcioglu, Y. Chetrit, N. Izhaky, and M. Paniccia, "High-speed optical modulation based on carrier depletion in a silicon waveguide", Vol. 15, Issue 2, Optics Express, 2007

[3] A. Beling, A. Cross, M. Piels, J. Peters, Q. Zhou, J. E. Bowers, and J. C. Campbell, "InP-based waveguide photodiodes heterogeneously integrated on silicon-on-insulator for photonic microwave generation", Vol. 21, Issue 22, Optics Express, 2014

[4] J. Hu, N. Carlie, N. Feng, L. Petit, A. Agarwal, K. Richardson and L. Kimerling, "Planar waveguide-coupled, high-index-contrast, high-Qresonators in chalcogenide glass for sensing", Vol. 33, No. 21, Optics Letters, 2008

[5] J. Bauters, J. R. Adleman, M. Heck, and J. Bowers, "Design and characterization of arrayed waveguide gratings using ultra-low loss Si3N4 waveguides", Applied Physics A, 2014

[6] M. Solmaz, D. Adams, S. Grover, W. Tan, X. Xia, O. Eknoyan, and C. K. Madsen, "Compact bends for achieving higher integration densities for LiNbO3 waveguides", Vol. 21, No. 9, IEEE Photonics Technology Letters, 2009

[7] Q. Xu, B. Schmidt, S. Pradhan and M. Lipson, "Micrometre-scale silicon electro-optic modulator", Vol. 435, Nature, 2005

[8] B. Little, S. Chu, H. Haus, J. Foresi, and J. Laine, "Microring resonator channel dropping filters", Vol. 15, No. 6, Journal of Lightwave Technology, 1997

[9] F. Morichetti, A. Canciamilla, C. Ferrari, A. Samarelli, M. sorel and A. Melloni, "Travelling-wave resonant four-wave mixing breaks the limits of cavity-enhanced all-optical wavelength conversion", No. 296, Nature Communications, 2011

[10] J. Hu, M. Torregiani, F. Morichetti, N. Carlie, A. Agarwal, K. Richardson, L. Kimerling and A. Melloni, "Resonant cavity-enhanced photosensitivity in As2S3 chalcogenide glass at 1550 nm telecommunication wavelength", Vol. 35, No. 6, Optics Letters, 2010

[11] M. Solmaz, D. Adams, W. Tan, W. Snider, and C. Madsen, "Vertically integrated As2S3 ring resonator on LiNbO3", Vol. 34, No. 11, Optics Letters, 2009

[12] H. Nishihara, M. Haruna and T. Suhara, “Optical integrated circuits”, McGraw-Hill Book Company, 1989

[13] G. Agrawal, “Nonlinear fiber optics: second edition”, Academic Press, 1995

[14] X. Xia, Y. Zhou and C. Madsen, “Analysis of As2S3-Ti: LiNbO3 taper couplers using supermode theory”, Vol. 2, No. 4, Optics and Photonics Journal, 2012

[15] D. Broaddus, M. Foster, I. Agha, J. Robinson, M. Lipson and A. Gaeta, “Silicon-waveguide-coupled high-Q chalcogenide microspheres”, Vol. 17, No. 8, Optics Express, 2009

[16] S. Campbell, “The science and engineering of microelectronic fabrication: second edition”, Oxford University Press, 2001